

Additive Manufacturing Methodology and System for Fabrication of Porous Structures with Functionally Graded Properties

by

Mihaela Vlasea

A thesis
presented to the University of Waterloo
in fulfilment of the
thesis requirement for the degree of
Doctor of Philosophy
in
Mechanical and Mechatronics Engineering

Waterloo, Ontario, Canada, 2014

© Mihaela Vlasea 2014

Declaration Page

I hereby declare that I am the sole author of this thesis. This is a true copy of the thesis, including any required final revisions, as accepted by my examiners.

I understand that my thesis may be made electronically available to the public.

Abstract

The focus of this dissertation is on the development of an additive manufacturing system and methodology for fabricating structures with functionally graded porous internal properties and complex three-dimensional external characteristics. For this purpose, a multi-scale three-dimensional printing system was developed, with capabilities and fabrication methodologies refined in the context of, but not limited to, manufacturing of porous bone substitutes. Porous bone implants are functionally graded structures, where internally, the design requires a gradient in porosity and mechanical properties matching the functional transition between cortical and cancellous bone regions. Geometrically, the three-dimensional shape of the design must adhere to the anatomical shape of the bone tissue being replaced.

In this work, control over functionally graded porous properties was achieved by integrating specialized modules in a custom-made additive manufacturing system and studying their effect on fabricated constructs. Heterogeneous porous properties were controlled by: (i) using a micro-syringe deposition module capable of embedding sacrificial elements with a controlled feature size within the structure, (ii) controlling the amount of binder dispersed onto the powder substrate using a piezoelectric printhead, (iii) controlling the powder type or size in real-time, and/or (iv) selecting the print layer stacking orientation within the part. Characterization methods included differential scanning calorimetry (DSC)-thermo gravimetric analysis (TGA) to establish the thermal decomposition of sacrificial elements, X-ray diffraction (XRD) and dispersive X-ray spectroscopy (EDAX) to investigate the chemical composition and crystallinity, scanning electron microscopy (SEM) and optical microscopy to investigate the physical and structural properties, uniaxial mechanical loading to establish compressive strength characteristics, and porosity measurements to determine the bulk properties of the material. These studies showed that the developed system was successful in manufacturing embedded interconnected features in the range of 100-500 μm , with a significant impact on structural properties resulting in bulk porosities in the range of 30-55% and compressive strength between 2-50 *MPa*.

In this work, control over the the three-dimensional shape of the construct was established iteratively, by using a silhouette extraction image processing technique to determine the appropriate anisotropic compensation factors necessary to offset the effects of shrinkage in complex-shaped parts during thermal annealing. Overall shape deviations in the range of $\pm 5-7\%$ were achieved in the second iteration for a femoral condyle implant in a sheep model.

The newly developed multi-scale 3DP system and associated fabrication methodology was concluded to have great potential in manufacturing structures with functionally graded properties and complex shape characteristics.

Acknowledgements

I would like to express my gratitude to the people in my life who made this academic journey a rich and fulfilling life experience.

I would like to thank my supervisor, Prof. Ehsan Toyserkani, for his guidance, support and trust throughout my academic career. Under his mentorship, I had the opportunity to truly advance my engineering design skills and scientific knowledge. I would also like to acknowledge my co-supervisor, Dr. Rita Kandel, for her kind support, enthusiastic vision for this project, and openness to a fruitful collaboration.

I hereby acknowledge my thesis examining committee members, Dr. Mark Filiaggi from Dalhousie University, Dr. John B. Medley, Dr. Jan Huissoon and Dr. Siv Sivaloganathan from the University of Waterloo for taking the time to review my thesis and to provide their valuable constructive insights. I would also like to acknowledge professors Dr. Maud Gorbet, Dr. Kaan Erkorkmaz, and Dr. Richard Wells, whose graduate courses have been extremely useful in developing some of the modelling and mathematical framework used in my dissertation.

This academic experience has shown me the value of interdisciplinary collaboration. I had the unique pleasure to be part of a wonderful and prestigious research group, working together toward achieving a unified purpose. My work would not have been made possible without Dr. Rita Kandel, Dr. Bob Pilliar, Dr. Mark Grynepas from Mount Sinai Hospital, Dr. Mark Hurtig from Guelph University, Dr. Paul Zalzal from McMaster University, Dr. Manuela Kunz from Queen's University, and my friend and collaborator David Lee, from University of Toronto. I would like to extend my thanks to Eugene Hu in the Institute of Biomaterial and Biomedical Engineering at the University of Toronto for his advice, his hard work in providing raw materials for my project, and for thermal annealing of parts.

I would like to extend a special thanks to the amazing technical staff team at University of Waterloo, electronic technologists Andy Barber and Jim Merli, CNC technicians Robert Wagner and Jason Benninger, for their amazing effort in assisting me with the electrical and mechanical troubleshooting of the newly developed three-dimensional printing system. I would also like to acknowledge Leanne Stodola and Anthony Khoraych from Advanced Test and Automation Inc. for their valuable input in software integration.

I would like to thank my colleagues at the Multi-scale Additive Manufacturing Laboratory research team at University of Waterloo, Dr. Yaser Shanjani, Dr. Hamidreza Alemohammad,

Ahmad Basalah, Elahe Jabari, Amir Azhari, Esmat Sheydaeian, Richard Liang, Farid Behzadian, Xixi Zhang, and Negar Rasti for their friendship and assistance.

I would also like to acknowledge the financial support from the National Resources and Engineering Research Council Canada Graduate Scholarship (NSERC CGS-M), the Government of Ontario for the Ontario Graduate Scholarship (OGS), University of Waterloo for President's Graduate Scholarship and Mechanical and Mechatronics Engineering Graduate Scholarship.

I owe my gratitude to my parents, Liana and Sorin, and to my sister Raluca, for instilling my passion for science and engineering and for their support and sacrifice in enabling me to pursue my professional and academic goals. I offer my special thanks to my beloved Andrej, for his cheerful encouragement throughout my academic years.

Dedication

To my beloved family

Table of Contents

List of Tables	xiii
List of Figures	xv
List of Abbreviations	xxi
1 Introduction and Literature Review	1
1.1 Structures with Functionally Graded Porous Properties	2
1.1.1 Industrial and Biomedical Applications	2
1.1.2 Manufacturing Methodologies for Structures with Controlled Porosity	4
1.1.2.1 Conventional Methodologies	4
1.1.2.2 Additive Manufacturing Methodologies	7
1.2 Additive Manufacturing Approach via 3DP	10
1.2.1 Description of 3DP Methodology	10
1.2.2 Current Research in 3DP Parameter Optimization	11
1.2.3 Advantages and Shortcomings of Conventional 3DP	12
1.3 Proposed Additive Manufacturing System and Methodology	13
1.3.1 System Components and Functionality	13
1.3.2 Manufacturing Design Cycle	15
1.3.3 Multi-scale 3DP System Applied to Bone Substitutes	16
1.3.3.1 Material Considerations	18
1.3.3.2 Structural Considerations	18
1.3.3.3 Mechanical Property Considerations	19
1.4 Motivations	20
1.5 Thesis Objectives	21
1.6 Thesis Outline	22

2	Control of Functionally Graded Properties via Micro-Dispensing of Sacrificial Photopolymer Materials	23
2.1	Material Considerations for Embedding Sacrificial Polymers	24
2.1.1	Materials and Methods	24
2.1.1.1	Brief Description of the Combined μ SD-3DP System	24
2.1.1.2	Sacrificial Photopolymer Deposition Process Description	26
2.1.1.3	Substrate Powder Material	26
2.1.1.4	Liquid Binder Material	27
2.1.1.5	Sacrificial Photopolymer Material	27
2.1.1.6	Sample Preparation	28
2.1.1.7	Post-processing Thermal Annealing of CPP	28
2.1.1.8	Geometry Characterization of Formed Channels	28
2.1.1.9	Polymer Thermal Decomposition Characterization	29
2.1.1.10	Surface Chemical Composition Characterization	29
2.1.1.11	Surface Material Composition Characterization	29
2.1.2	Results	30
2.1.2.1	Geometry Characterization of Formed Channels	30
2.1.2.2	Polymer Thermal Decomposition Properties	30
2.1.2.3	Surface Chemical Composition Properties	32
2.1.3	Discussion	34
2.2	Modelling and Experimental Validation of a Micro-syringe Deposition System for Dispensing Sacrificial Photopolymers on Particulate Ceramic Substrates	36
2.2.1	Analytical Model Development	36
2.2.1.1	Pressure-Flow Model	36
2.2.1.2	Deposition Geometry Model	39
2.2.2	Materials and Methods	40
2.2.2.1	Substrate Powder Material	40
2.2.2.2	Liquid Binder Material	41
2.2.2.3	Sacrificial Photopolymer Material	41
2.2.2.4	Sample Fabrication and Preparation	42
2.2.2.5	Sample Feature Geometrical Characterization	43
2.2.2.6	Sample Surface Roughness Characterization	44

2.2.3	Results	44
2.2.3.1	Experimental Measurements vs. Simulated Outputs	44
2.2.3.2	Effect of UV Exposure Latency on Experimental Measurements	46
2.2.3.3	Desired Feature Range vs. Experimental and Simulated Results	47
2.2.3.4	Surface Roughness Results	47
2.2.4	Discussion	47
2.3	Summary	50
3	Control of Functionally Graded Properties via Greyscale Binder Levels	52
3.1	Materials and Methods	53
3.1.1	Powder Substrate Material	53
3.1.2	Liquid Binder Material	53
3.1.3	Sample Fabrication	54
3.1.4	Dimensional Shrinkage Characterization	55
3.1.5	Porosity Characterization	55
3.1.6	Uniaxial Compression Characterization	56
3.1.7	Statistical Analysis	56
3.2	Results	57
3.2.1	Dimensional Shrinkage Results	57
3.2.2	Bulk Porosity and Density Results	58
3.2.3	Mechanical Strength - Uniaxial Compression Results	59
3.3	Discussion	61
3.4	Summary	63
4	Control of Functionally Graded Properties via Multi-powder Composition	64
4.1	Materials and Methods	66
4.1.1	Powder Substrate Material	66
4.1.2	Liquid Binder Material	66
4.1.3	Powder Size Characterization	66
4.1.4	Sample Fabrication	66
4.1.5	Dimensional Shrinkage Characterization	67
4.1.6	Porosity Characterization	67
4.1.7	Structural Characterization	67

4.1.8	Uniaxial Compression Characterization	68
4.1.9	Statistical Analysis	68
4.2	Results	68
4.2.1	Powder Size Characterization Results	68
4.2.2	Structural Characterization Images	70
4.2.3	Dimensional Shrinkage Results	70
4.2.4	Bulk Porosity and Density Results	72
4.2.5	Mechanical Strength - Uniaxial Compression Results	73
4.3	Discussion	74
4.4	Summary	76
5	Control of Functionally Graded Properties via Print Layer Orientation	78
5.1	Materials and Methods	79
5.1.1	Powder Substrate Material	79
5.1.2	Liquid Binder Material	79
5.1.3	Sample Fabrication	79
5.1.4	Porosity Characterization	80
5.1.5	Structural Characterization	80
5.1.6	Uniaxial Compression Characterization	80
5.1.7	Statistical Analysis	80
5.2	Results	81
5.2.1	Structural Characterization Results	81
5.2.2	Bulk Porosity and Density Results	82
5.2.3	Mechanical Strength - Uniaxial Compression Results	83
5.3	Discussion	84
5.4	Summary	87
6	Additive Manufacturing Design Cycle for Complex-Shaped Structures with Functionally Graded Properties	88
6.1	Case Study	90
6.1.1	Design Cycle Step 1 - Selection of Implantation Site	90
6.1.2	Design Cycle Step 2 - Identification of Load Kinetics and Kinematics	91
6.1.3	Design Cycle Step 3 - Optimization of 3DP Print Parameters	92

6.1.4	Design Cycle Step 4 - Evaluation of Anisotropic Shrinkage	93
6.1.5	Design Cycle Steps 5 and 6 - Additive Manufacturing of Part	93
6.2	Case Study Outcomes	95
6.3	Discussion	101
6.4	Summary	102
7	Conclusions and Future Work	103
7.1	Thesis Conclusions	104
7.2	Recommendations and Future Work	105
	APPENDICES	108
A	Appendix A Proposed Additive Manufacturing Process Description	109
B	Appendix B Proposed Additive Manufacturing System Capabilities	115
C	Appendix C Analytical Modelling of Micro-syringe System	120
D	Appendix D Surface Roughness Experimental Measurements	123
E	Appendix E Closed Loop Control Strategy for Micro-syringe System	125
F	Appendix F License Agreements	128
	References	131

List of Tables

Table 1.1	Porous properties of cancellous and cortical bone in humans	19
Table 1.2	Mechanical properties of cancellous and cortical bone in humans	19
Table 2.1	FESEM-EDAX analysis results	33
Table 2.2	Nomenclature and associated equations	37
Table 2.3	Geometrical characteristics of dispensing system	39
Table 2.4	Photopolymer fluid flow properties	42
Table 2.5	Selected variables in this study. An inconsistent deposition is one where the deposited tracks are intermittent and reliable measurements could not be obtained	43
Table 3.1	Dimensional shrinkage (%) in diameter d and height h of two categories of parts, with 150 and 190 μm layer thickness respectively, printed at 70, 80, 90, 100, and 90/70% greyscale levels, ($n = 10$)	57
Table 3.2	Bulk density of two categories of parts, with 150 and 190 μm layer thickness respectively, printed at 70, 80, 90, 100, and 90/70% greyscale respectively, ($n = 10$)	58
Table 3.3	Mechanical compression parameters for samples with layer thickness of 150 and 190 μm , printed at 70, 80, 90, 100, and 90/70% greyscale level respectively, ($n = 10$)	59
Table 4.1	Dimensional shrinkage of parts, with small CPP ($<75 \mu m$), with large CPP (75-150 μm), and dual CPP (measurements of bottom half large and top half small) powder size composition, ($n = 10$).	71
Table 4.2	Bulk density (g/cm^3) of parts, with small CPP ($<75 \mu m$), with large CPP (75-150 μm), and dual CPP (top half small, bottom half large) powder size composition, ($p < 0.05$), ($n = 10$)	72
Table 4.3	Uniaxial compression results for three classes of parts, small, large, and dual particle size composition, ($n = 10$)	73

Table 5.1	Bulk porosity and bulk density characteristics for cylindrical samples printed with layer stacking orientations of 0, 30, 45, 60, and 90° respectively, ($n = 10$) . . .	82
Table 5.2	Uniaxial compression results and Weibull moduli of cylindrical samples printed with layer stacking orientations of 0, 30, 45, 60, and 90° respectively, ($n = 8$)	83
Table 5.3	Normal and shear stress distribution along orientation planes for samples manufactured with stacked layers of orientation 0, 30, 45, 60, 90° respectively . . .	86
Table 6.1	The estimated compensation factor (CF) along the x- and y- axis respectively. * The direct shrinkage measurement is computed by comparing sintered vs. pre-sintered parts. **The indirect measurement is computed by cumulating the initial isotropic compensation factor to the shrinkage measured between the sintered part and the benchmark. The estimated compensation factor (CF) is calculated as the average of the direct and indirect shrinkage, with a complement sign	99
Table B.1	Multi-scale 3DP workstation, mechatronics components	117
Table D.1	Surface roughness values for CPP samples with particle size 75-150 μm . R_a is the arithmetic average of absolute values roughness parameter. R_q is the root mean squared roughness parameter.	124

List of Figures

Figure 1.1	Structures with functionally graded properties manufactured in response to different sets of required functionalities across two interfaces	4
Figure 1.2	Conventional methods for producing functionally graded porous structures	7
Figure 1.3	Classification of additive manufacturing methods for producing functionally graded porous structures	8
Figure 1.4	Conventional 3DP manufacturing system. In Step 1, the system is initialized. In Step 2, the feed bed is moved up by a piston, pushing excess powder above the feed bed rim. The build bed is actuated down, by an amount equivalent to the layer thickness. A counter rotating roller spreads the powder from the feed bed to the build bed. In Step 3, a printhead deposits a binder based on the corresponding slice image of the layer. The process is repeated until the part is completed	10
Figure 1.5	Novel multi-scale 3DP additive manufacturing system for fabrication of functionally graded porous structures. (100) Granite support, (101) Precision xy gantry assembly, (102) Counter rotating roller module, (103) Multiple supply bed selection and alignment module, (104) Binder dispensing printhead module, (105) Build bed module, (106) Sacrificial porogen particle insertion module, (107) Micro-syringe sacrificial polymer deposition module, (108) Micro-syringe deposition control, (109) Precision control z-axis, (110) UV curing module	14
Figure 1.6	Fabrication cycle for the novel multi-Scale 3DP mechatronic system for manufacturing of structures with functionally graded properties	15

Figure 1.7	Multi-scale 3DP manufacturing system. 1) The hardware is initialized. 2) One of multiple feed beds is selected, aligned, and actuated up by a piston, pushing excess powder above the feed bed rim. The build bed is actuated down, by an amount equivalent to the layer thickness. A counter rotating roller spreads the powder from the feed bed to the build bed. 3) A printhead deposits a binder based on the corresponding slice image of the layer. 4) If needed, a sacrificial polymer can be deposited at specific locations within the layer. 5) If needed, sacrificial porogen particles can be deposited at specific locations within the layer. The process is repeated until the part is completed	16
Figure 1.8	Design cycle for the novel multi-Scale 3DP mechatronic system for manufacturing structures with functionally graded properties	17
Figure 2.1	(a) Combined additive manufacturing via 3DP- μ SD for creating structures with interconnected features. (b) An example of a channel obtained after the heat treatment protocol, viewed under scanning electron microscopy (SEM), longitudinal aspect, 150x magnification	25
Figure 2.2	Relevant hardware components of the μ SD system	26
Figure 2.3	Multi-scale 3DP fabrication system showing the micro-syringe deposition system (μ SD) and a close-up view of a typical manufactured layer with the deposited photopolymer structure on the powder substrate	27
Figure 2.4	Cross-section of CPP part with integrated channels after heat treatment, viewed under an optical microscope. The part was encapsulated in epoxy, sliced in the vertical plane, and polished	30
Figure 2.5	Cross-section of CPP part with integrated micro-channels after heat treatment viewed under SEM a), b) top view x75 magnification, and c), d) view from a 30 ° inclination with x25 and x100 magnifications respectively. (*) Shows a defect in the channel	31
Figure 2.6	Polymer thermal decomposition TGA results of a) EBA* and b) PVA	32
Figure 2.7	FESEM-EDAX analysis of a typical CPP-PVA-EBA* sample after thermal annealing using a 250 μm^2 area	33
Figure 2.8	XRD analysis of CPP-PVA versus CPP-PVA-EBA* thermally annealed samples	34

Figure 2.9	Schematic of pressure-flow analytical model	38
Figure 2.10	Block diagram presentation of the combined analytical pressure-flow model and stochastic deposition geometry model	41
Figure 2.11	Photopolymer fluid power law approximation	42
Figure 2.12	Fabricated sample with deposited photopolymer tracks	44
Figure 2.13	Track width with respect to velocity of the nozzle at different volumetric flows. Experimental vs. modelled data with a sensitivity domain based on Monte Carlo simulations	45
Figure 2.14	Graphs illustrate the effect of UV exposure latency of 5 s, 18 s, and 30 s on the experimental measured line width. An increase in UV latency decreases the observed width	46
Figure 2.15	Cross-sectional area of experimental and simulated features versus the min- imum and maximum threshold of cross-sectional areas corresponding to features in the range 100-500 μm in diameter respectively	47
Figure 3.1	An illustration of samples manufactured with different greyscale levels of 70, 80, 90, 100, and 90/70% respectively, ($n = 10$)	54
Figure 3.2	Bulk porosity characteristics of cylindrical samples with layer thickness of 150 μm and 190 μm , at grayscale of 70, 80, 90, 100, 90/70% respectively. ($n = 10$). (*). Illustrates Tukey HSD statistical pairwise similarities	58
Figure 3.3	Ultimate compressive strength of samples with layer thickness of 150 μm and 190 μm , at grayscale levels of 70, 80, 90, 100, and 90/70% respectively, ($n =$ 10). (*) Illustrates Tukey HSD statistical pairwise similarities	59
Figure 3.4	Weibull failure probability functions and linear interpolations for compres- sive strength of samples printed with layer thickness of a) 150 μm and b) 190 μm , ($n = 10$)	60
Figure 4.1	An illustration of the newly developed multi-scale 3DP machine showing the powder beds integrated in the system. (100, 101, 102) Feed bed compartment modules, (103) Build bed module, (104) Printhead, (105) Micro-syringe deposition module, (106) UV curing module, (107) Roller module	65
Figure 4.2	An illustration of samples manufactured with large, small, and dual powder sizes, ($n = 10$) respectively	67

Figure 4.3	The particle size distribution for a) large particle size, sieved between 75-150 μm , ($n = 105$) and b) small particle size, sieved at $<75 \mu m$, ($n = 300$)	69
Figure 4.4	SEM view of powder with a),c) large particle size, sieved 75-150 μm at magnification x200, x25; b),d) small particle size, sieved $<75 \mu m$ at magnification x200, x1000	70
Figure 4.5	SEM view of sintered samples with a), c) large particle size at magnification x100, x30; b),d) small particle size, at magnification x100, x300	71
Figure 4.6	Bulk porosity characteristics and compressive strength measurements of cylindrical samples with small, large and dual particle size composition, with ($p < 0.05$). For each trial, ($n = 10$). (*) Illustrates Tukey HSD statistical pairwise similarity	72
Figure 4.7	Weibull failure probability functions and linear interpolations for compressive strength of cylindrical samples printed with small, large and dual sample particle size composition, ($p < 0.05$), ($n = 10$)	73
Figure 4.8	Thermally annealed samples with large, small, and dual particle size composition	75
Figure 5.1	Parts printed with 0, 30, 45, 60, 90° layer orientation, arranged in the build compartment. The axes shown correspond to the ZPrint TM software axes	80
Figure 5.2	Images of a CPP sample with 60° layer stacking orientation as viewed under SEM with a magnification of a) x22, b) x100 and c) x300	81
Figure 5.3	Bulk porosity characteristics of cylindrical samples layer stacking orientations 0, 30, 45, 60, and 90° respectively, ($n = 10$). (*) Illustrates Tukey HSD pairwise statistical similarities	82
Figure 5.4	Compression strength characteristics of cylindrical samples with layer stacking orientations 0, 30, 45, 60, and 90° respectively, ($p < 0.05$), ($n = 8$). (*) Illustrates Tukey HSD pairwise statistical similarity	83
Figure 5.5	Weibull failure probability functions and linear interpolations for compressive strength of cylindrical samples printed with layer stacking orientations 0, 30, 45, 60, and 90 ° respectively,, ($n = 8$)	84
Figure 6.1	Multi-scale 3DP design cycle for bone substitutes with complex internal and external architecture	89

Figure 6.2	Selection of implantation site - medial femoral trochlea in a sheep model	91
Figure 6.3	Layer stacking orientation for multi-scale 3DP process for the complex-shaped medial femoral trochlear bone substitute in a sheep model	92
Figure 6.4	The silhouette extraction methodology employs (a) images of the implants in specific orientations to produce (b) thresholded black and white images that can be used to compute the (c) silhouettes of the part. Silhouette contours are then sampled to quantify the shrinkage effects after thermal annealing	94
Figure 6.5	Schematic of additive manufacturing fabrication methodology	95
Figure 6.6	Silhouette extraction showing shrinkage after thermal annealing in xz and yz planes for complex shaped medial femoral implant at 5, 10 and 15% isotropic compensation compared to an ideal benchmark	96
Figure 6.7	Calculated shrinkage in the a) xz plane (x direction shrinkage shown) and b) yz plane (y direction shrinkage shown) for pre-sintered green complex shaped medial femoral trochlea implants at 5, 10, and 15% isotropic compensation compared to an ideal benchmark	97
Figure 6.8	Calculated shrinkage in the a) xz and b) yz planes for complex shaped medial femoral trochlea implant at 5, 10, and 15% isotropic compensation compared to an ideal benchmark	98
Figure 6.9	Silhouette extraction showing shrinkage in xz and yz planes for complex shaped medial femoral implant at 30, 20, and 10% anisotropic compensation in the x, y, z directions respectively compared to an ideal benchmark	100
Figure A.1	Pre-processing execution engine high level overview for the novel multi-scale 3DP mechatronic system.	110
Figure A.2	Processing execution engine high level overview for the novel multi-scale 3DP mechatronic system. Powder spread execution step.	111
Figure A.3	Processing execution engine high level overview for the novel multi-scale 3DP mechatronic system. Printing of binder execution step.	112
Figure A.4	Processing execution engine high level overview for the novel multi-scale 3DP mechatronic system. Depositing sacrificial polymer features execution step.	113
Figure A.5	Processing execution engine high level overview for the novel multi-scale 3DP mechatronic system. Depositing sacrificial porogen particles execution step.	114

Figure B.1	Novel multi-scale 3DP additive manufacturing system for fabrication of functionally graded porous structures. (100) Granite support, (101) Precision xy gantry assembly, (102) Counter rotating roller module, (103) Multiple supply bed selection and alignment module, (104) Binder dispensing printhead module, (105) Build bed module, (106) Sacrificial porogen particle insertion module, (107) Micro-syringe sacrificial polymer deposition module, (108) Micro-syringe deposition control, (109) Precision control z-axis, (110) UV curing module	116
Figure B.2	The relevant hardware componets for the feed bed powder systems	118
Figure B.3	The relevant hardware componets for the micro-syringe deposition module	118
Figure B.4	The relevant hardware componets for the porogen insertion module. This system is currently under development	119
Figure C.1	Analytical pressure-flow model as programmed in Simulink	121
Figure C.2	Formulae descriptions for pressure-flow model as programmed in Simulink	122
Figure D.1	Profile of CPP ceramic part with particles (75-150) μm in size	124
Figure E.1	Control strategy for the pressure flow component of the μSD system	126
Figure F.1	129
Figure F.2	130

List of Abbreviations

2D	Two dimension(al)
3D	Three dimension(al)
3DP	Three dimensional printing
AM	Additive manufacturing
AMF	Additive manufacturing file format
ANOVA	Analysis of variance
A-P	Anterior-posterior
BW	Body weight
CAB	Cellulose acetate butyrate
CAD	Computer aided design
CF	Compensation factor
CPP	Calcium polyphosphate
CT	Computed tomography
CT	Computed tomography
DMLS	Direct metal laser sintering
DSC	Differential scanning calorimetry
EBA	Ethoxylated (10 bisphenol A diacrylate)
EBM	Electron beam melting
EDAX	Dispersive X-ray diffraction spectroscopy
FDM	Fused deposition modelling
HSD	Honest significant differences
LDM	Low temperature deposition modelling
M-L	Medial-lateral
MLS	Modified least squares
PI	Photoinitiator, in context
PI	Proportional-integral control, in context
PVA	Polyvinyl alcohol
SEM	Scanning electron microscope or microscopy
SL	Stereolithography
SLS	Selective laser sintering
STL	Stereolithography file format
TGA	Thermo gravimetric analysis
μ SD	Microsyringe deposition system
UV	Ultraviolet
XRD	X-ray diffraction

Chapter 1

Introduction and Literature Review

The concept of functionally graded materials dates back to the mid 1980's, when Japanese researchers investigated metal-ceramic composites to be implemented as thermal barriers in rocket engines [1]. It was observed that using materials with a controlled gradient in heterogeneous properties yielded superior performance when compared to their homogeneous counterparts [2]. In general, functionally graded constructs exhibit a gradual change in structural, compositional and/or mechanical properties along one or more directions in response to a change in functionality at the interfaces between the construct and the environment [3]. They can be either chemically monolithic or composite in nature, and display a smooth transition between regions with different properties, without clear boundaries or interfaces [1].

Presently, there is an active interest in developing manufacturing processes for fabricating products with functionally graded porous properties, with areas of application ranging from electronics, aerospace, automotive, to biomedical applications [4, 5]. The focus of this chapter is to outline the importance of functionally graded structures in industrial and biomedical applications and to provide an overview of current state of the art conventional and additive manufacturing methodologies and their limitations in fabricating such constructs. A novel additive manufacturing system and methodology via three-dimensional printing is proposed to address some of the known limitations in controlling the functionally graded porous structure and composition of complex-shaped constructs, with a direct application in fabricating bone substitute implants.

1.1 Structures with Functionally Graded Porous Properties

1.1.1 Industrial and Biomedical Applications

There are many industrial and biomedical applications requiring structures with functionally graded porous properties. In the biomedical field, researchers have explored the fabrication of musculoskeletal, maxillofacial, and dental implants [3, 6, 7, 8] with controlled porous characteristics. In industry, applications such as ultrasonic piezoelectric transducers [2, 9, 10], filtration devices [11], thermal shields [12], fuel cells [13, 14] and electrodes [15] are some of the areas of interest in controlling porosity gradients within fabricated components. Porous properties are classified in terms of (i) pore size or scale such as macro, micro, meso and nano, (ii) geometry of pores such as irregular, oriented, fibrous, or networked, and (iii) degree of connectivity such as interconnected or open pores, isolated or closed pores [2] and blind pores accessible from a single direction [11].

In industry, an example of structures with functionally graded porous requirements are piezoelectric ultrasonic transducers intended for medical diagnostic devices. An optimal ultrasonic transducer would combine the capability of having a high piezoelectric response with having a good acoustic coupling with the media in contact with the transducer [9]. To produce a high piezoelectric response, a dense region of piezoceramic is required, called an active piezoelectric layer. Conversely, to allow for acoustic coupling with the media, a porous region is required, called a matching piezoelectric layer. A single phase homogeneous piezoelectric material would not meet these two design constraints at the same time [2]. Research has shown that the ideal device would display a continuous gradient in porosity from the active layer to the matching layer to improve acoustic energy transfer and piezoelectric response [2, 9, 10]. Other industrial areas of application where materials with functionally graded porous design are required are filtration devices [11], thermal shields [12], fuel cells [13, 14], and electrodes [15].

When considering biomedical applications, it is important to note that natural tissues are generally not homogeneous, with a structural complexity dictated by local functional requirements. A popular area of application, where materials with heterogeneous structural properties are required, is in manufacturing of musculoskeletal, maxillofacial and dental implants. The incentive for implementing functionally graded properties in such implants is to improve their biomechanical behaviour in order to avoid stress shielding and osteolysis, to improve osteoconductivity and implant fixation, and to induce the appropriate cellular cues dictated by gradients in porosity

and mechanical properties [3, 16].

Porous bone substitutes are an example of functionally graded constructs. They serve as an extracellular matrix to provide the mechanical and biological template for bone regeneration. This means that such porous implants are customized to have the desired bio-chemical signals that promote biocompatibility, osteogenesis, osteocompatibility, osteoinduction, osteoconduction, and an adequate *in vivo* degradation rate [5, 17]. From a structural standpoint, in designing a bone implant, it is necessary to consider a gradient in porosity and mechanical properties, from a dense external configuration matching the characteristics of cortical bone to the highly porous region with interconnected porosity matching the characteristics of cancellous bone [3]. Furthermore, natural bone architecture contains Volkmann- and Haversian-like conduits and trabeculae channels arranged in a three-dimensional network as a direct result of adaptations to mechanical loading, as postulated by Wolff's Law [18] and the mechanostat theory [19]. The ideal bone implant should closely adhere to the the internal configuration of the natural bone to be replaced. This means that the designed bone substitute must have a heterogeneous porous structure, with varying physical and mechanical characteristics. In addition, the implant must also be designed to have an anatomically accurate three dimensional shape in order to maintain a natural contact load distribution post implantation [20].

Dental implants are another example of structures where functionally graded properties are required. For such implants, a portion of the part is embedded in bone, while the other portion is exposed. The exposed segment has to be dense and strong enough to withstand occlusal forces, whereas the portion of the implant interfacing the bone has to be porous to allow osteoconductivity and an appropriate osteointegration with the surrounding bone tissue [3]. A structurally and compositionally homogeneous dental implant would not be able to simultaneously meet these requirements, as an implant with a dense structural composition throughout would cause stress shielding and poor osteointegration, while an entirely porous material would not satisfy strength requirements.

As seen, there is a broad range of applications in the industrial and biomedical field for constructs with a gradient in structural and mechanical properties across one or more orientations, in response to a change in functionality at the interface between the structure and the environment. An illustration of a general design requirements for constructs with functionally graded properties is shown in Figure 1.1. Specialized manufacturing methodologies have to be considered for such devices, depending on the material composition and the porosity requirements.

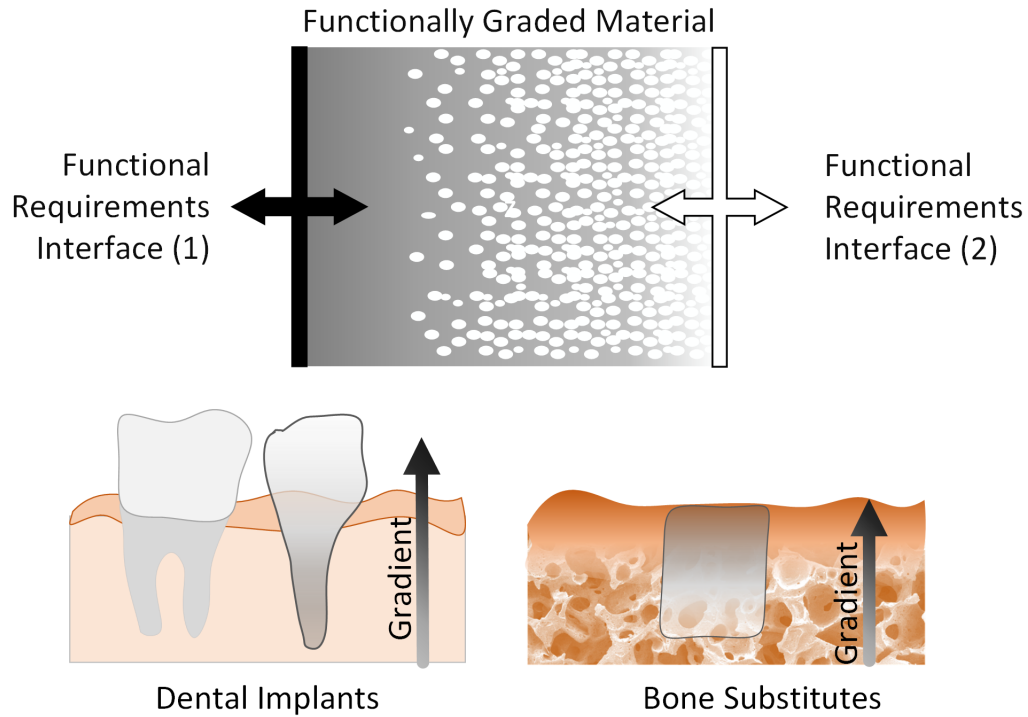


Figure 1.1: Structures with functionally graded properties manufactured in response to different sets of required functionalities across two interfaces

1.1.2 Manufacturing Methodologies for Structures with Controlled Porosity

A general classification of manufacturing methodologies for structures with embedded porosity distinguishes between conventional methods and additive manufacturing approaches [21]. Conventional methods typically focus on introducing the required range of porosity into the material using various mechanical, chemical or electrochemical approaches and are generally not adept in creating versatile complex-shaped structures. Additive manufacturing approaches are used to build-in the porosity as the part is being manufactured in a layer-by-layer fashion, with flexible control over three-dimensional shape complexity.

1.1.2.1 Conventional Methodologies

Casting methods are common conventional approaches in manufacturing porous metallic, ceramic or polymeric structures, where the final three-dimensional shape of the part is dictated by a cast receptacle. Freeze casting, often referred to as freeze-drying, is employed in particular on ceramics and hybrid ceramic/polymer composites [12, 22] where a material suspension, generally consisting of the material powder, solvent, and additives, is exposed to a freezing cycle that

allows the solvent to form crystal geometries within the part. The freezing cycle is followed by a solidification and sublimation process to remove the frozen solvent, thus resulting in embedded porous configurations. It has been shown that by controlling the freezing temperature vector across the cast, oriented or dendritic networked porosities can be achieved [12]. Centrifugal and gravity-set casting are two examples of methods used to influence the particle size, type and porous distribution inside the manufactured structure [1]. In gravity casting, suspensions of different particle sizes or types are poured in a cast and sedimented, dried, compacted and then sintered, resulting in a gradient of porosity and mechanical properties [1]. Similarly, in centrifugal casting, the predominant sedimentation drivers are the centrifugal and Coriolis forces [1] instead of gravity, resulting in similar effects. Another casting approach used in influencing porosity, commonly employed with ceramics and polymers, is solvent casting and particulate leaching. In this method, a solution comprised of a solvent, a polymer/ceramic, and suspended porogen sacrificial particles are precipitated or solidified into a cast or mold; the porogens are subsequently dissolved or sublimated from the final part to generate the required porosity [6, 8, 23]. Tape casting is another method commonly used to manufacture thin layers of ceramic green tapes from slurries with different porogen sizes and concentrations, followed by staking the tapes together and sintering them to produce a gradient porosity [9]. Using casting methodologies, porosity may be influenced by using a range of thermal, mechanical and chemical approaches. Some of the shortcomings of casting methods are that the porous characteristics are process-specific, requiring multiple steps to achieve the desired porosity specifications, with poor control over the degree of connectivity between pores. There are also limitations in entirely removing the sacrificial porogen materials, use of harsh solvents, and very limited capability of producing complex three dimensional shapes.

Gas foaming is another category of methods used in influencing porosity within structures. One such example is supercritical foaming or fluid-gassing of polymers [6]. A supercritical fluid is in a state above its critical pressure and temperature, where fluid follows the typical behaviour of a gas. In this state, a gas such as CO₂ is introduced and diffused in the polymer matrix. The blend is plasticised at high pressure to produce a foam [24]. In metallic materials, porous structures formed using gasses are called gasars and are formed by dissolution of a gas into a metal at high pressures, forming a so-called supersaturated melt, followed by solidification at lower pressure [1, 23]. The controlled solidification of the metal with embedded gas bubbles has been found to generate oriented or ordered porosity due to an effect of unidirectional solidification that is dependent on

the gas type and pressure, initial mould temperature, cooling rate, and direction of heat removal [1]. Gas foaming using foaming agents is another common approach for integrating gas bubbles into materials in a liquid state. Typically for polymers such as hydrogels, gas foaming agents such as sodium bicarbonate are mixed in with the polymer solution and allowed to chemically decompose and generate gas by-products [23]. In general, for porous structures produced using gas foaming methods, fracture may occur when returning the matrix to atmospheric pressure and room temperature. Another shortcoming is that, although high levels of porosity can be achieved, pore interconnectivity is generally low [6]. Gas foaming methods are also highly sensitive to process parameters, with limited control over pore size and pore spatial distribution. Limited reproducibility and ability to manufacture complex three-dimensional shapes are also important manufacturing constraints.

Melt infiltration into graded preforms is an indirect method to generate porous structures with influence on porosity, pore orientation and pore interconnectivity [1]. A preform, typically composed of a salt or wax, is constructed to mimic the orientation of the desired final interconnected porous characteristics. The material in a molten or liquid state is infiltrated into the open-cell preform, generally under pressure. The preform and material composite are then cured or solidified and the preform is removed as a final step [1]. Porogens can be infiltrated in the melt to further increase porosity. This method offers an indirect multi-step approach to porosity control and is also not adept at producing three-dimensional complex geometries.

Various conventional methods can be employed to manufacture porous samples from powder materials. Powder metallurgy is one of the most common approaches, where powders, typically ceramics, piezoceramics, or metallic composites, are deposited in a mould, compressed, and then sintered at high temperatures [3]. Control of porous properties can be achieved by stacking layers of powders with different composition [25] or size [26] in the mould before pressing and sintering [2, 27, 28]. If heat is applied during compaction, the methodology is referred to as hot pressing [3, 28]. The sintering or thermal annealing processes can influence porosity gradients and can be achieved by applying heat [26], microwave energy [29] or pulsed electrical current [25]. Powder metallurgy is very popular, however the shortcomings are that the cooling process is shown to induce thermal stresses and micro-crack defects within the manufactured structure, pore interconnectivity is not guaranteed, and only simple geometries can be produced using this approach.

The most common conventional methodologies for manufacturing porous structures with func-

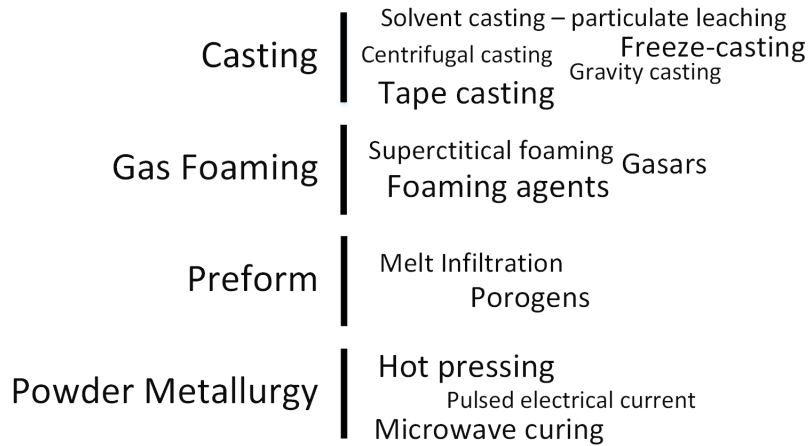


Figure 1.2: Conventional methods for producing functionally graded porous structures

tionally graded porosity are summarized in Figure 1.2. Although these approaches can result in influence over pore size and distribution within the part itself, the methods are process-specific and highly sensitive to variations in process parameters, generally resulting in poor reproducibility. Furthermore, if a change in porous design is required, multiple steps in the process have to be redesigned. These approaches are also not conducive to manufacturing parts with complex three-dimensional characteristics, which is a driving engineering design parameter. New methodologies, called additive manufacturing approaches, can be employed to address some of these limitations.

1.1.2.2 Additive Manufacturing Methodologies

Materials with functionally graded porous internal properties and complex three dimensional external characteristics are referred to as designer structures [21]. Additive manufacturing (AM) approaches are being refined toward achieving the goal of fabricating such designer structures. AM methodologies allow for parts to be built incrementally, layer-by-layer, based on information provided from a computer-aided design (CAD) program [30, 31]. New methodologies for correlating CAD data to functionally graded material properties and layer manufacturing characteristics, called digital manufacturing [32], are currently being developed. Additive manufacturing technologies strive to have each layer built to have the specific morphological configuration that would result in the desired micro- and macro- structure of the final part. In essence, AM offers the possibility of automated manufacturing of highly reproducible custom-shaped parts with controlled internal structure and custom external three dimensional architecture [30].

There are various AM techniques¹ that can be used to construct designer structures, depending on the type of raw materials used. Based on the ASTM F2792 - 12a standard terminology for additive manufacturing technologies [34], the general categories of AM methodologies are: (i) liquid-based methods such as direct light processing (DLP), stereolithography (SL), (ii) solid or slurry extrusion-based methods such as fused deposition modelling (FDM), low temperature deposition modelling (LDM), and (iii) powder-based methods such as selective laser sintering (SLS), direct metal laser sintering (DMLS), electron beam melting (EBM), and three-dimensional printing (3DP). These methods are summarized in Figure 1.3.

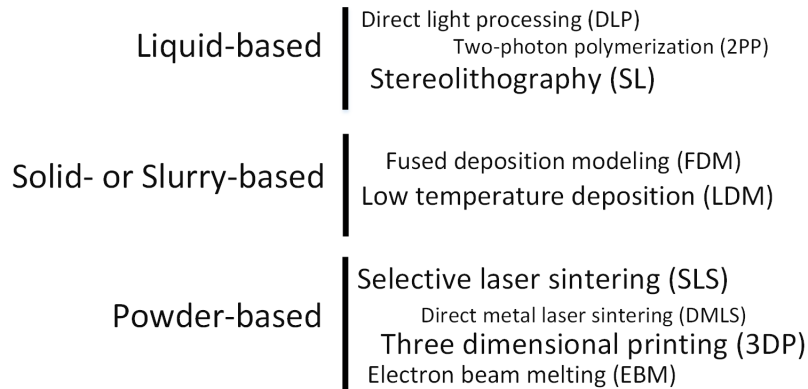


Figure 1.3: Classification of additive manufacturing methods for producing functionally graded porous structures

One class of AM systems relies on photopolymerization of liquid-based materials. The idea behind this AM fabrication method is to use radiant energy to excite and initiate the polymerization process in low molecular weight monomers that are capable of forming long chain polymers [35]. The family of polymers is called photopolymers. Biophotopolymers are a type of photopolymers that can biologically degrade by hydrolytic cleavage [36]. A photopolymerization approach is direct light processing (DLP), where an array of micro-mirrors is used to direct light onto a photosensitive resin only at specific locations within each layer [37]. Stereolithography (SL) is another photopolymerization method, where an ultraviolet (UV) laser moves in the x-y plane to irradiate and solidify a layer of UV curable polymer at specific locations [38]. In general, photopolymerization is one of the most accurate additive manufacturing techniques, with a high resolution, but it is limited to using photopolymeric materials [8]. The exposure to high temperatures required for fabrication may induce thermal degradation of the material, affecting its mechanical strength and chemical integrity [35].

¹The materials presented in Section 1.1.2.2 are adapted from the author’s published work [33], unrestricted

Solid- or slurry-based AM methodologies rely on extrusion of melted materials or solids suspended in slurries. The most common method is called fused deposition modelling (FDM). A typical FDM machine deposits molten thermoplastics extruded through a heated nozzle displaced in the x-y plane to produce one layer following a specific geometric path based on CAD data. The layer is then displaced in the z-direction, and a new layer can be built sequentially [30]. The molten material deposited onto each layer will soften the material deposited in the previous one and upon solidification, the two layers will be joined together. Low temperature deposition (LDM) is a method that uses a non-heating liquefying deposition head to deposit a slurry that solidifies due to a low temperature manufacturing environment [39]. The most important benefit of these methods is the fact that there is a low risk of residual build materials being trapped inside the part. There is, however, a scarce choice of materials that can be used for fabrication using these approaches [30]. Furthermore, these techniques require the integration of extra support structures for building complex shapes with over-hanging features. Using these methods, the nozzle dimension is one of the key limiting parameters that influence the feature size.

Another class of AM techniques apply to powder-based materials. One such method is Selective Laser Sintering (SLS), where a laser beam, typically a CO₂ laser, is used to locally raise the temperature of composite powders up to the glass transition temperature resulting in fusion of neighbouring particles and previous deposition layer [35]. The powder can be a polymer, ceramic, metal, or composites [31]. The laser is displaced in the x-y plane to create a layer based on CAD slice data. A roller mechanism spreads a new layer of powder and the process is repeated. The benefit of SLS is that there is generally no need for post-processing steps. The process also allows for a wide variety of materials to be used. The major disadvantage is that it is difficult to remove the powder trapped within the parts, limiting the overall feature size that can be achieved using this method [31]. Also, because of the high temperature involved during the manufacturing process, the materials may thermally degrade, reducing the mechanical strength of the part [31]. High temperatures will also lead to unwanted bonding amongst adjoining powder particles, decreasing resolution, accuracy, and repeatability, and making it difficult to build features less than 400 μm [35]. The feature size is also limited by the laser spot size. Direct metal laser sintering (DMLS) is a similar technique, where the raw materials are metals or metal composites. Three dimensional printing (3DP) is another category of powder-based additive manufacturing methodologies. This technique is very popular and is discussed in detail in Section 1.2.

1.2 Additive Manufacturing Approach via 3DP

1.2.1 Description of 3DP Methodology

A type of powder-based additive manufacturing (AM), colloquially known as three dimensional printing (3DP) or adhesion bonding [35], allows parts to be manufactured in a layer-by-layer fashion based on information provided by a software program. A three dimensional (3D) model is first designed in a computer aided design (CAD) software and then sectioned into bottom-up images corresponding to parallel slices or layers. 3DP employs powders as the substrate material for constructing the designed parts in a layer-by-layer fashion [5]. Within each layer, the powder particles are first spread onto a building area using a counter-rotating roller and then cemented together at locations corresponding to the slice layer image by injecting a binder using an ink-jet or similar printing technology [40, 41, 42]. The building area moves down, allowing for new layers of powder to be spread sequentially until the part is completed. The resulting product is referred to as green part. Further post-processing is typically required to fully cure or anneal the green part [6, 35]. An illustration of the conventional 3DP process is shown in Figure 1.4.

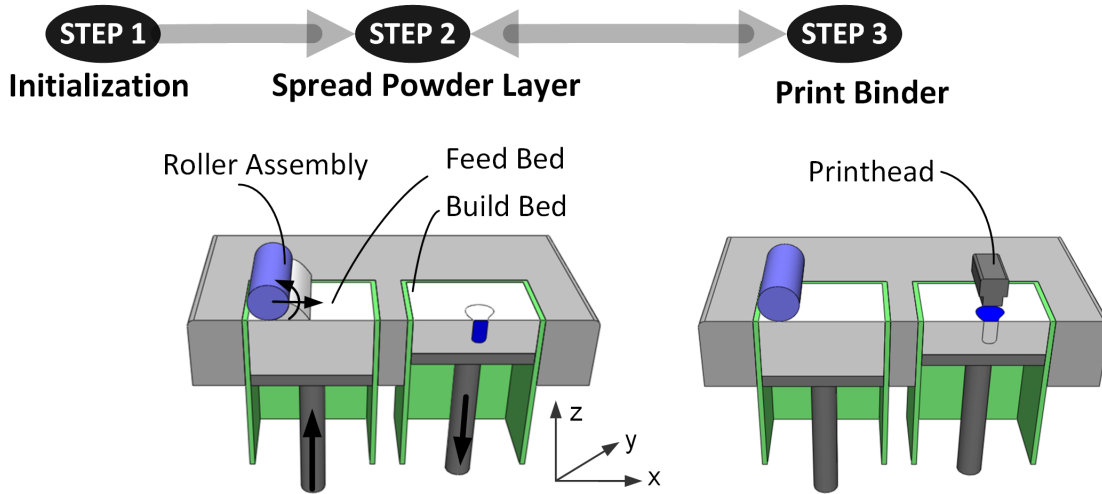


Figure 1.4: Conventional 3DP manufacturing system. In Step 1, the system is initialized. In Step 2, the feed bed is moved up by a piston, pushing excess powder above the feed bed rim. The build bed is actuated down, by an amount equivalent to the layer thickness. A counter rotating roller spreads the powder from the feed bed to the build bed. In Step 3, a printhead deposits a binder based on the corresponding slice image of the layer. The process is repeated until the part is completed

The 3DP technology was developed at Massachusetts Institute of Technology (Cambridge, Massachusetts) and patented in the early 1990's [40, 41, 42]. Since then, researchers have explored

the capabilities of this manufacturing approach in different areas of application such as shape memory alloys [43, 44], carbon performs [45], metallurgy tooling [46], metallic prostheses [47], and biomedical and tissue engineering scaffolds [48, 49, 50]. The 3DP process has great versatility and can be tailored for a wide range of industrial and biomedical applications. As such, research groups have focused on the tuning and optimizing the powder-based 3DP process parameters to control the chemical, structural and mechanical functionality of the resulting parts in an attempt to achieve control over heterogeneous or functionally graded porous properties.

1.2.2 Current Research in 3DP Parameter Optimization

One of the important 3DP process parameters is the liquid binder in terms of chemical composition [51, 52], concentration [51, 52, 53], and discrete saturation levels on the powder substrate [44, 54, 55]. Vorndran et al. [52], for instance, analysed different types of binder-powder substrate interactions to determine an appropriate binder solution that would produce samples with a desired compressive strength and porosity. To achieve a similar goal, the research done by Gbureck et al. [53] focused on studying the effect of varying the concentration of liquid binders. In a different approach, Suwanprateeb et al. [54] used two binder saturation levels to wet powder substrates and observed that an increased binder saturation level increased the flexural strength of green parts. In all these investigations, the binder composition, concentration and saturation levels are kept homogeneous throughout the manufactured part, which is a limiting factor of conventional 3DP systems in constructing functionally graded constructs.

Another class of 3DP parameters involve the substrate powder materials in terms of the blend composition [50, 51, 52, 56, 57, 58, 59, 60, 61] and powder particle sizes [62] employed in the conventional 3DP process. Researchers [59, 60] have investigated the effect of mixing the powder build material with different coating ratios of a powder binder to enhance the flowability of the powder for the 3DP process and to study the effect on the shrinkage, porosity and mechanical strength of the final part. The effect of powder particle size on the physical, structural and mechanical properties of the scaffolds was studied by Will et al. [62]. In all these experiments, the powder composition and size is homogeneous throughout each manufactured part, which is a limiting capability of conventional 3DP in constructing functionally graded materials.

Layer thickness [44, 54, 55, 63, 64] and layer orientation [63, 48, 65] within the part make up another set of parameters for the 3DP process. Suwanprateeb et al. [54] used a range of thickness

settings and concluded that layer thickness has a significant impact on part strength, with the lowest performance attributed to the highest layer thickness. Layer stacking orientation also has a significant effect on part strength and porosity, as it was found that irregular-shaped particles with an aspect ratio greater than one adopt a preferred orientation during powder spreading, with a direct influence on thermal annealing outcomes [48]. In all these experiments, the layer thickness is constant throughout the manufactured part, which is a limiting capability of conventional 3DP in constructing functionally graded materials.

The effect of integrating open or closed macro-channels with different orientations, sizes and shapes during the AM process on the porosity, mechanical strength of the parts has also been studied [49, 50, 51, 62, 66, 67]; overall, these studies demonstrated difficulty in achieving features below 500 μm in size using this fabrication method.

The extensive research done on optimizing the 3DP process parameters demonstrates the growing interest in utilizing this technology across diverse areas of application. Researchers have utilized the features and benefits of 3DP, while continuously pushing the boundaries imposed by the limitations of commercially available systems.

1.2.3 Advantages and Shortcomings of Conventional 3DP

A significant benefit of the 3DP methodology is that a wide variety of materials in powder form such as polymers, ceramics, metals, and composites can be used to manufacture products [5, 8, 35, 68]. Other advantages include: the ease of customizing, scaling and reproducing complex-shaped designs with no need for support structures [8, 30, 31, 35]; green part manufacturing at room temperature [30, 31, 35, 65, 68]; and digital control of 3D shape design and macro features such as embedded interconnected channels [6, 8, 21, 30, 35, 56, 65]. For some applications, such as tissue scaffold design, the inherent microporosity resulting from the arrangement of powder particles in the AM process is also a highly beneficial feature [21, 30, 31]. The versatility of this methodology is the the driving factor in selecting 3DP methodologies as the focus of this research in manufacturing structures with functionally graded porous characteristics.

To understand the motivation behind this research, it is important to review the current limitations of 3DP AM technologies. One of the most pressing drawbacks is that the smallest feature size of conventional powder-based 3DP techniques is limited by the binder droplet volume [5], powder particle size with appropriate flowability [5, 31, 69], powder compaction force

[70] and the high potential for having trapped particles inside cavities formed within the part [5, 30, 31, 35]. Overall, it is difficult to achieve features below $500\mu m$ in size using this fabrication method [5, 30, 31, 35, 68]. This issue becomes even more pressing in manufacturing constructs with complex conformal channels, as it becomes increasingly difficult to remove trapped support materials from features within the parts. Other emerging limiting aspects of conventional powder-based 3DP techniques are the use of only one powder size or powder type during manufacturing, the application of a constant compaction force during powder layer spreading, the utilization of a single layer thickness setting throughout the part, and the lack of control over the greyscale gradient of binder volume dispersed within each layer. These aspects impose limitations in manufacturing of porous scaffolds with heterogeneous or functionally graded properties as required in various industrial and biomedical applications, and are the focus of this work.

1.3 Proposed Additive Manufacturing System and Methodology

1.3.1 System Components and Functionality

To address the current limitations in 3DP technology, a mechatronic system was designed to control the fabrication of functionally graded internal features, porosities and material properties of parts. To this end, a multi-scale 3DP manufacturing system was developed, where a collection of control modules were incorporated to achieve the required performance. Such controlled devices include a counter-rotating roller module, multiple supply bed selection and alignment module, sacrificial porogen particle insertion module, sacrificial polymer deposition module, ultraviolet curing module, and an environment control module. A schematic of this system is shown in Figure 1.5.

The sacrificial porogen particle insertion module and sacrificial polymer deposition module assemblies are used to produce a controlled porous feature size in the range of $100\text{-}500\ \mu m$ that can be achieved by selectively depositing either porogens or sacrificial polymeric structures on specific layers. The porogen and/or sacrificial polymer can thermally disintegrate during post-processing, leaving behind controlled porosities and/or interconnected channels. This approach allows for control of internal features by avoiding loose support powder material from being trapped inside complex cavities of parts. The multiple supply bed selection and alignment module can be used to select from different available powder types or sizes in real time during manufacturing, enabling

control over micro-porosity and material composition. The counter-rotating roller module can be used to selectively control the powder compaction force while spreading powder material from the feed bed to the building area, which further modulates the control over micro-porosity, powder density and mechanical properties.

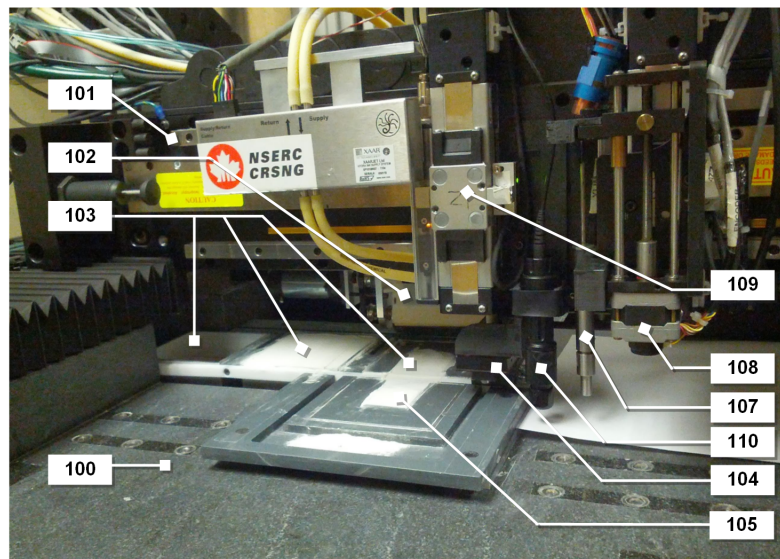
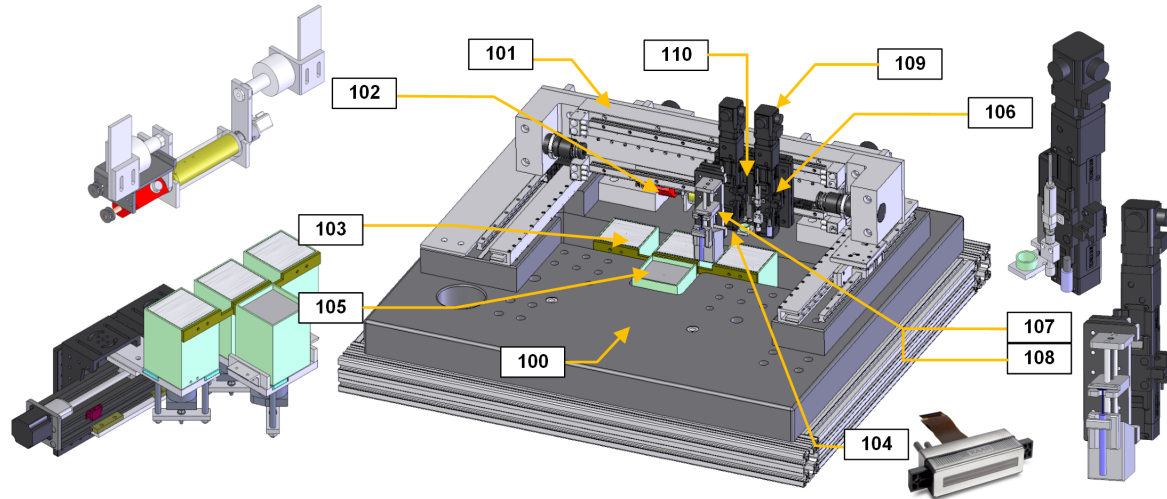


Figure 1.5: Novel multi-scale 3DP additive manufacturing system for fabrication of functionally graded porous structures. (100) Granite support, (101) Precision xy gantry assembly, (102) Counter rotating roller module, (103) Multiple supply bed selection and alignment module, (104) Binder dispensing printhead module, (105) Build bed module, (106) Sacrificial progen particle insertion module, (107) Micro-syringe sacrificial polymer deposition module, (108) Micro-syringe deposition control, (109) Precision control z-axis, (110) UV curing module

The versatile multi-scale 3DP mechatronic system has been developed over the course of this research. The high level part fabrication cycle is illustrated in Figure 1.6. Each step in

this fabrication cycle is described in detail in Appendix A, where some of the procedures are outlined for each sub-set of execution steps. The motion system components and capabilities are summarized in Appendix B. The outlined steps in Figure 1.6: (2) spreading powder layer, (3) printing binder over powder layer, and (4) depositing and curing sacrificial polymer networks are the focus of this thesis and will be addressed individually. A more descriptive diagram of the multi-scale 3DP process is shown in Figure 1.7.

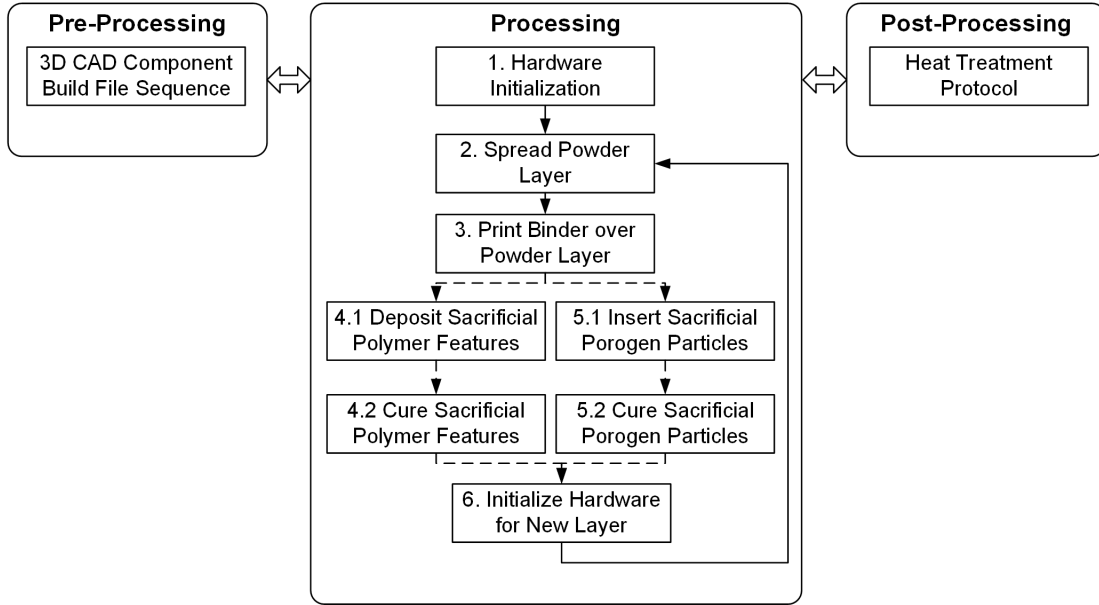


Figure 1.6: Fabrication cycle for the novel multi-Scale 3DP mechatronic system for manufacturing of structures with functionally graded properties

1.3.2 Manufacturing Design Cycle

In this thesis, an additive manufacturing cycle as shown in Figure 1.8 is proposed for designing complex-shaped parts with functionally graded porous properties. This cycle illustrates an effective approach to ensure that the shape, structural and mechanical properties of the part are met, provided that the materials have been selected appropriately. The first step is to select the area of application for the intended part, in order to define functional design requirements such as required macro- and micro- porous gradient properties, pore shape and interconnectivity, and three-dimensional shape architecture. Secondly, it is important to gain knowledge into the general load kinetics and kinematics at the site where the part will be used in order to estimate the magnitude and direction of contact forces that the part should withstand safely and

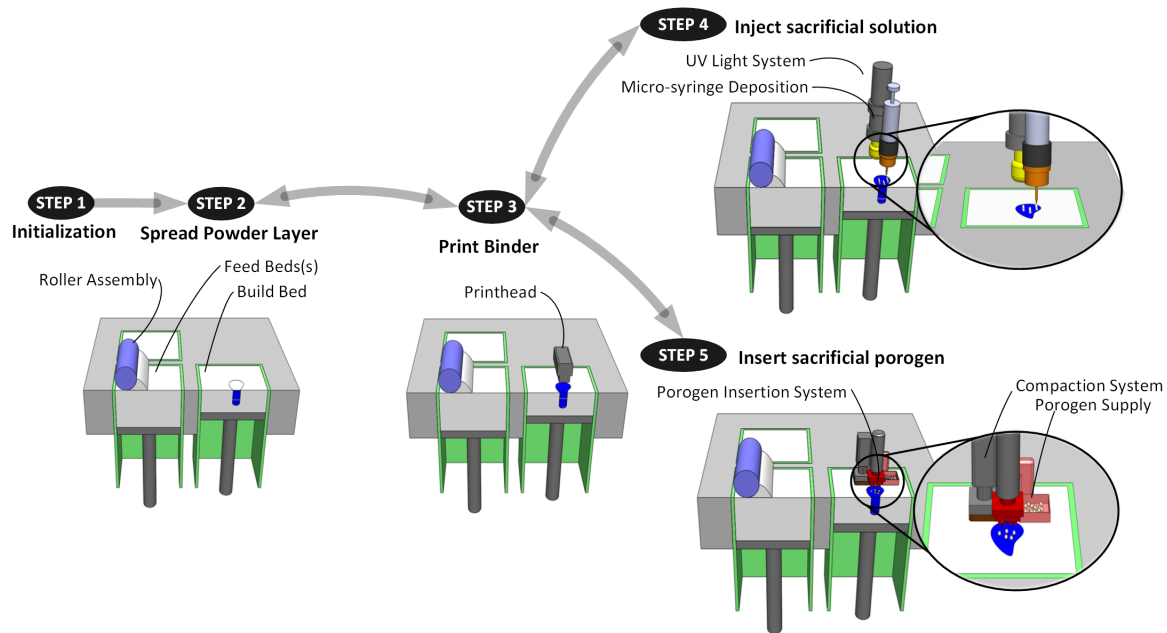


Figure 1.7: Multi-scale 3DP manufacturing system. 1) The hardware is initialized. 2) One of multiple feed beds is selected, aligned, and actuated up by a piston, pushing excess powder above the feed bed rim. The build bed is actuated down, by an amount equivalent to the layer thickness. A counter rotating roller spreads the powder from the feed bed to the build bed. 3) A printhead deposits a binder based on the corresponding slice image of the layer. 4) If needed, a sacrificial polymer can be deposited at specific locations within the layer. 5) If needed, sacrificial porogen particles can be deposited at specific locations within the layer. The process is repeated until the part is completed

repeatedly. Based on the application functionality and loading requirements, in the third step, the AM parameters can be tuned to provide the required mechanical and structural properties of the part. In the fourth step, appropriate anisotropic compensation factors should be considered to compensate for the shrinkage that typically occurs during the thermal annealing process [70]. The design cycle is iterative in nature, as seen in Figure 1.8. This design cycle is applied to test and validate the new multi-scale 3DP platform.

1.3.3 Multi-scale 3DP System Applied to Bone Substitutes

The capabilities of the newly developed multi-scale 3DP system for producing structures with functionally graded porous properties have been tested in the context of manufacturing bone substitute implants. The incentive behind fabricating constructs with a direct application in bone and joint reconstruction surgeries lies in understanding the demand for such devices. Musculoskeletal diseases involve a variety of conditions such as arthritis, osteoporosis, traumatic musculoskeletal

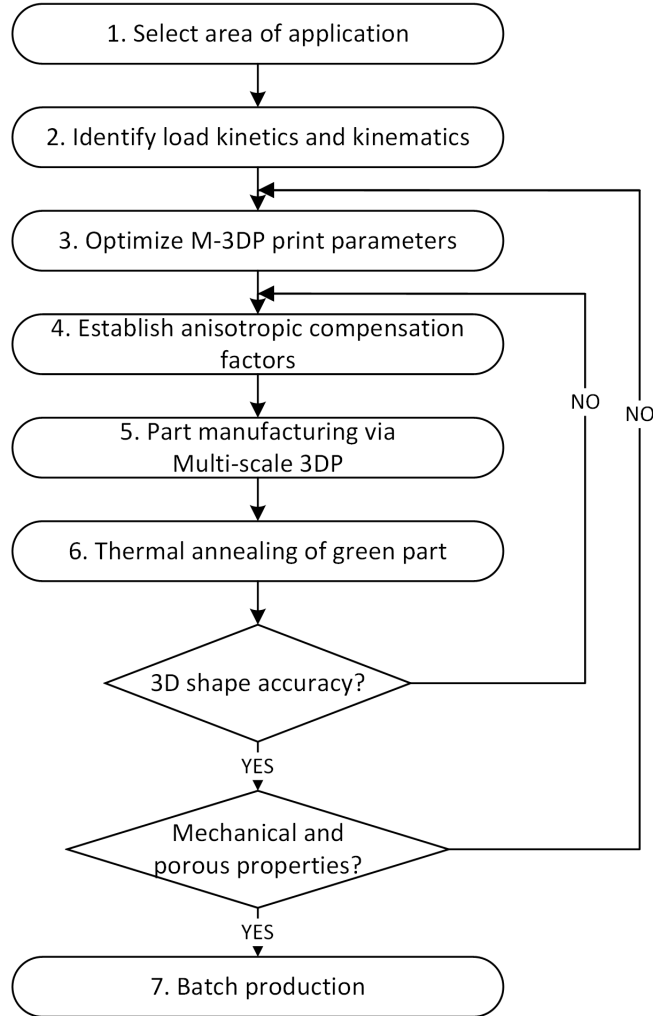


Figure 1.8: Design cycle for the novel multi-Scale 3DP mechatronic system for manufacturing structures with functionally graded properties

injuries, spinal injuries and spinal deformities [71]. Although they are mostly non life-threatening, these conditions can become very debilitating, diminishing the quality of life of the affected individuals by causing ongoing pain, discomfort, inflammation and restrictions in range of motion [71]. Aside from clinical repercussions, musculoskeletal conditions represent a major financial burden on the healthcare sector [71, 72]. The current conventional treatment for advanced joint and bone trauma is to fully or partially replace the affected area with tissue grafts [73] or artificial prosthetics [18] to restore near-normal functions. Current state-of-the-art prosthetic implants fail to meet structural and functional requirements that would render them as permanent remediation solutions [18]. As a result, thousands of patients undergo painful and costly subsequent surgeries

for implant replacements or readjustments. Cell-based or tissue graft solutions have been proven to ameliorate the quality of life of patients, but are limited in terms of size and anatomical shape of defect that can be addressed, as well as the availability of healthy donor tissue and morbidity of donor site [20, 73, 74]. There is a pressing need for a more successful approach to bone and osteochondral reconstruction procedures that takes into account both biological and anatomical factors. One such approach focuses on tissue engineered biocompatible and bioresorbable bone substitutes that can replace the defect area, gradually mature and seamlessly integrate with the native tissue [6].

1.3.3.1 Material Considerations

The bone substitute material must be highly biocompatible to avoid the expression of unwanted immune responses to the implant and at the same time to encourage cell attachment and proliferation [7, 69]. The bone substitute must be bioresorbable such that it is capable of bulk degradation and resorption through natural pathways with no residual *in vivo* side effects [6, 7, 75]. The material itself has to be osteo-conductive to encourage fast bone ingrowth from surrounding healthy tissue [76] and also non-toxic, non-mutagenic, non-carcinogenic, non-teratogenic [31]. For load bearing applications, a type of ceramic called calcium polyphosphate (CPP) is amongst one of the more promising materials for producing bone substitutes. Calcium polyphosphate is a form of condensed calcium phosphate with a lower ratio of Ca:P that forms linear polymeric-like phosphate chains [76]. This material is biocompatible and biodegradable forming calcium orthophosphate which is a “naturally occurring and readily metabolizable substance” [76]. The material is also osteoconductive, allowing rapid bone ingrowth into the implant [76, 77]. *In vivo* and *in vitro* studies have also shown that CPP also encourages cartilage formation and anchorage [77]. CPP has been chosen as the the material of interest in manufacturing of bone substitutes via multi-scale 3DP.

1.3.3.2 Structural Considerations

An ideal bone substitute should closely adhere to the the internal configuration of the natural bone to be replaced or enhanced [5, 7]. For such implants, from a structural standpoint, it is necessary to implement a gradient in porosity and mechanical properties, from a dense external configuration matching the characteristics of cortical bone to the highly porous region with in-

terconnected porosity matching the characteristics of cancellous bone [3, 5, 7]. The implant must also be designed to have an anatomically correct shape and initial internal structure that can allow it to mimic the surrounding native tissue in terms of mechanical properties, physiological and biological properties. It has been shown that the development and proliferation of cells within the scaffold material is reliant on the implant porosity, pore size and pore interconnectivity [69]. For bone substitutes, the range in required pore size varies between 100 – 500 μm [69, 78, 79]. A highly porous material with a high level of pore interconnectivity and surface area is desirable since it encourages cell ingrowth, the exchange of nutrients and waste materials, as well as vascularization [69, 80]. Porosity ranges between 30-90% have been investigated for bone engineered scaffolds, depending on the target implant site. In this thesis, the newly developed multi-scale 3DP system capabilities were tested in the context of fabricating functionally graded porous constructs with an application in bone substitutes, with target porous properties as described in Table 1.1.

Table 1.1: Porous properties of cancellous and cortical bone in humans

Bone Type	Porosity (%)	Pore Size (μm)	Apparent Density (g/cm^3)
Cancellous bone [81, 5]	50-90	≤ 1000	0.30 ± 0.10
Cortical bone [81, 5]	3-12	100-500	1.85 ± 0.06

1.3.3.3 Mechanical Property Considerations

The high level of porosity and pore interconnectivity that is ideal for a bone substitute may be limited by the mechanical strength requirements for that specific implant, especially in the case of load bearing applications. The bone substitute should provide physical support, starting from the seeding process *in vitro* until the tissue is remodelled *in vivo*. The implant must provide sufficient mechanical support to endure *in vivo* stresses and load bearing cycles [6]. Table 1.2 summarizes the range in mechanical properties of human cancellous and cortical bone, and are the benchmark for comparing the strength of parts manufactured using the multi-scale 3DP approach.

Table 1.2: Mechanical properties of cancellous and cortical bone in humans

Bone Type	Tensile Strength (MPa)	Compressive Strength (MPa)	Young's Modulus (GPa)
Cancellous bone [69]	N/A	4-12	0.02-0.5
Cortical bone [69]	60-160	130-180	3-30

1.4 Motivations

Literature suggests that structures with functionally graded porous internal properties and complex three-dimensional external characteristics have a wide range of industrial and biomedical applications. Such structures display a gradient in structural and mechanical properties in response to a change in functionality at two or more interfaces between the structure and the environment in which they operate. Extensive research is currently being conducted in developing and refining fabrication methodologies for controlling the heterogeneous properties required for these parts.

Conventional manufacturing methodologies such as casting, gas foaming, infiltration into preforms, and powder metallurgy have been shown to influence the pore size and pore distribution within parts made up of ceramic, metallic, polymeric, and composite materials; however, these methods are generally process specific, with poor reproducibility and high sensitivity to process parameters. Conventional methods are pre-tuned for specific part characteristics and require a process overhaul if the porous design requirements are modified. Furthermore, these approaches are not adept for manufacturing complex-shaped constructs, which is a limiting design constraint.

Additive manufacturing methodologies allow the parts to be built incrementally, in a layer-by-layer fashion based on three-dimensional part characteristics designed in a CAD environment. Depending on the type of materials used in the manufacturing process, additive manufacturing can be categorized into liquid, solid or slurry, and powder based approaches. Liquid, solid and slurry based systems are limited in terms of what materials can be used in the process, while powder methodologies show flexibility in terms of the range of ceramic, metal, polymer and composite substances that can be used as raw materials. This thesis focuses on a powder-based additive manufacturing approach called three dimensional printing due to its versatility in processing materials, fabrication at room temperature, and overall ease of operation.

In a continuous effort to control heterogeneous structural characteristics within parts, a new trend in additive manufacturing software development is to correlate CAD data with functionally graded material properties and layer manufacturing characteristics. This endeavour is detailed through the recently proposed ASTM F2915-12 standard specification for additive manufacturing file format (AMF) developed by ASTM Committee F42, with a focus on geometric fidelity, multiple material composition, graded materials, and heterogeneous physical properties. Presently, there are no powder-based additive manufacturing systems commercially available that can inte-

grate such advanced digital manufacturing capabilities. To this effect, in this thesis, a multi-scale 3DP fabrication technology is described whereby a collection of mechatronic modules are incorporated to achieve the required performance that would allow for control of internal functionally graded properties as dictated by digital manufacturing CAD requirements. These modules include a counter-rotating roller module, multiple supply bed selection and alignment module, sacrificial porogen particle insertion module, sacrificial polymer deposition module, ultraviolet curing module, an 8 bit greyscale printhead for binder jetting, and an environment control module. In essence, the developed multi-scale 3DP system offers the possibility of automated manufacturing of reproducible custom-shaped parts with controlled internal structure and custom external three dimensional architecture.

The motivation for this thesis is to further the current state of the art of powder-based additive manufacturing via 3D printing by investigating a new multi-scale 3DP system and associated methodologies for controlling the heterogeneous or functionally graded porous structure and composition of complex-shaped constructs and establishing the effect of fabrication process parameters on resulting mechanical properties. The capabilities of the newly developed multi-scale 3DP system are tested in the context of manufacturing bone substitute implants.

1.5 Thesis Objectives

The objective of this thesis is to develop an *“additive manufacturing methodology and system for fabrication of porous structures with heterogeneous or functionally graded properties”*.

To meet this objective, the following tasks were undertaken:

- **Additive manufacturing system development:** Design, integration and software orchestration of a collection of mechatronics systems that work synchronously to achieve a desired functionality.
- **Additive manufacturing system and product characterizations:** Analyse the performance of additive manufacturing modules and characterize their respective effect on heterogeneous or functionally graded properties (i.e. chemical, structural, and mechanical properties) in the context of fabricating bone substitutes.
- **Additive manufacturing design cycle validation:** Outline and implement an additive manufacturing design cycle in the context of fabricating complex-shaped bone constructs.

1.6 Thesis Outline

This thesis includes seven chapters. Chapter 1 outlines the problem definition and literature review on the current state of the art technologies and a proposed multi-scale 3DP additive manufacturing system for fabricating structures with functionally graded porous properties. The capacity to control internal structural porous properties using this proposed system is then investigated by integrating sacrificial elements with a controlled feature size as described in Chapter 2, by controlling the amount of binder levels onto the powder substrate as observed in Chapter 3, by controlling the powder type or size as seen in Chapter 4, or by controlling the layer orientation as seen in Chapter 5. Chapter 6 outlines an additive manufacturing design cycle that allows for optimization of process parameters and ensures three-dimensional part fidelity. In Chapter 7, conclusions and proposed future studies are presented.

Chapter 2

Control of Functionally Graded Properties via Micro-Dispensing of Sacrificial Photopolymer Materials

The focus of this chapter is on fabricating functionally graded porous structures with embedded interconnected conduit networks by depositing a sacrificial photopolymer on powder substrates during the additive manufacturing process using a novel multi-scale 3DP system. The modules of interest in this approach are a precision micro-syringe deposition (μ SD) module and a UV curing module, in conjunction with a custom powder-based 3DP system described in Chapter 1, Section 1.3. The pore size target using this methodology is in the range of 100-500 μm , with an interconnected network structure. In this work, the two main considerations in successfully achieving porous structures using sacrificial features are: (1) investigating the behaviour of the material system consisting of the powder substrate and sacrificial photopolymer to determine the effects of thermal disintegration of the sacrificial polymer ¹, and (2) characterizing the photopolymer deposition process onto the powder substrate using modelling and experimental approaches². The work described in this chapter applies directly to manufacturing bone substitutes with functionally graded porous properties; however, the sacrificial element approach can be employed for other applications utilizing different powder substrates by following a similar methodology. To the author's knowledge, there are no such approaches yet described in the literature for 3DP.

¹Adapted from the author's published work [82], license agreement in Appendix F

²Adapted from the author's published work [83], license agreement in Appendix F

2.1 Material Considerations for Embedding Sacrificial Polymers

The main purpose of this materials study is to demonstrate that the proposed sacrificial photopolymer can be deposited onto and embedded into particulate powder substrates using the multi-scale 3DP system in conjunction with a micro-syringe deposition (μ SD) module, and that the thermal annealing process for the green part ensures that the photopolymer is fully removed during the post-processing stage to prevent host immune responses or other detrimental side effects post implantation. In this work, this is achieved by selecting a bioceramic with known biocompatibility and determining if the 3DP- μ SD process is a feasible manufacturing approach, as well as if the introduction of the photopolymer changes the final chemical and crystalline properties of the thermally annealed part.

2.1.1 Materials and Methods

2.1.1.1 Brief Description of the Combined μ SD-3DP System

The multi-scale 3DP technique employs ceramic powder as the substrate material. The structure is built in a layer-by-layer fashion in multiple steps as shown in Chapter 1, Figure 1.7. The purpose of the μ SD system is to deposit sacrificial polymers throughout the part to produce a network of tracks that mimic the required complexity of internal interconnected channels. The deposited structures will be disintegrated during thermal annealing of the green part, leaving behind the corresponding macro-porous channels and cavities as seen in Figure 2.1. The first step in the process is the development of a 3D CAD model based on the required internal and external architecture while considering manufacturability constraints. The CAD model is then dissected into thin 2D image slices, which can be manufactured using the powder-based multi-scale 3DP system system in a layer-by-layer fashion. Within each layer, the powder is first spread using a counter-rotating roller mechanism and then selectively bonded together at specific locations by injecting a binder using an inkjet-like printing technology. A new layer of powder is subsequently spread on top of the current layer. The manufacturing cycle is repeated until the part is completed. If needed, on specific layers, a sacrificial photopolymer is injected to create the required voids and conformal channels. The green part is subsequently exposed to a multi-stage thermal annealing protocol to first remove the sacrificial polymer and binder, and then create sinter necks between powder particles.

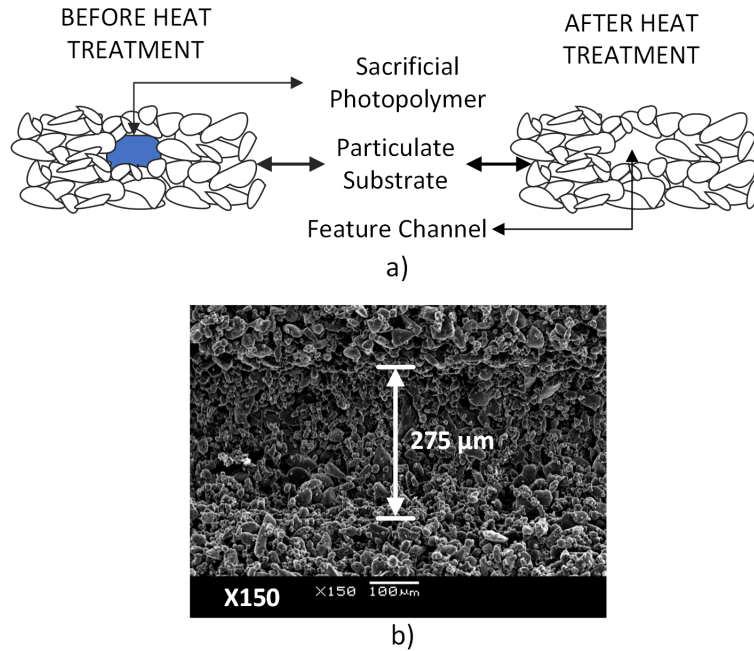


Figure 2.1: (a) Combined additive manufacturing via 3DP- μ SD for creating structures with interconnected features. (b) An example of a channel obtained after the heat treatment protocol, viewed under scanning electron microscopy (SEM), longitudinal aspect, 150x magnification

For the polymer deposition process, the relevant hardware modules are illustrated in Figure 2.2. The μ SD process control module is comprised of a modified modular piston-driven pump apparatus (70-2225 UL Modular Pump, Harvard Apparatus, Quebec, Canada) mounted on a high precision x-y-z positioning system. The μ SD process control module is used to control the deposition of the photopolymer track on the powder substrate. The μ SD system uses a ceramic deposition nozzle (1573-xx-437GM, CoorsTek, Inc. Gaiser Products Group, Ventura, CA, USA) adapted for this application. The custom ceramic nozzle minimizes droplet accumulation at the tip, does not chemically interact with the material, preserves its dimensional properties under elevated temperatures and is reliable for multiple injection cycles. The UV curing process module is a solid-state UV spot light (SUV-01, Algitron, Woburn, MA, USA), 385 nm wavelength, 2.0-3.2 W/cm^2 intensity, 4 mm spot diameter size at a distance of 20 mm, and is used to cure the photopolymer track extruded through the μ SD system. There is a physical offset of 2.5 cm in the y-direction between the μ SD nozzle and the UV curing head to avoid photopolymerization of fluid inside the nozzle.

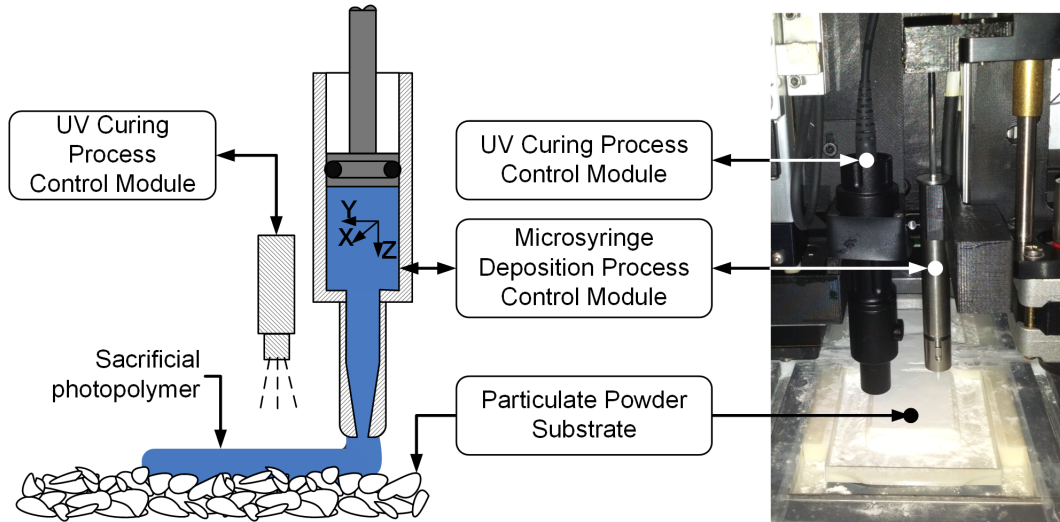


Figure 2.2: Relevant hardware components of the μ SD system

2.1.1.2 Sacrificial Photopolymer Deposition Process Description

The photopolymer was injected using the custom μ SD system under continuous UV light exposure from a curing height of 10 *mm*. Different injection process parameters were tested for feasibility. An experimental and modelling characterization of the process will be discussed Section 2.2. For feasibility studies, the injection head velocity varied from 1 to 2.5 *mm/s*, and the value of the flow rate was between 2.5 and 10 $\mu\text{L}/\text{min}$. A nozzle size of 150 μm was used, at a work height of approximately 100 μm , where as a rule-of-thumb, the deposition height should be between half or one full nozzle diameter [84]. These values were selected based on empirical hardware testing trials. The proposed photopolymer achieved consistent and accurate deposition tracks, proving that this photopolymer was a feasible choice in terms of injectability and curing time. Figure 2.3 depicts an actual view of the 3DP- μ SD system, along with an example of deposited tracks onto the powder substrate.

2.1.1.3 Substrate Powder Material

In this study, the powder material used in the AM process was calcium polyphosphate (CPP) powder (University of Toronto, Toronto, ON, Canada) with an irregular particle shape and size between 75-150 μm , blended with polyvinyl alcohol (PVA) powder (Alfa Aesar, Ward Hill, MA) with particle size <63 μm . The powder mix had a composition of 90 wt% CPP and 10 wt% PVA. To ensure a homogeneous powder blend, the powders were mixed for 4 hours using a rotating jar

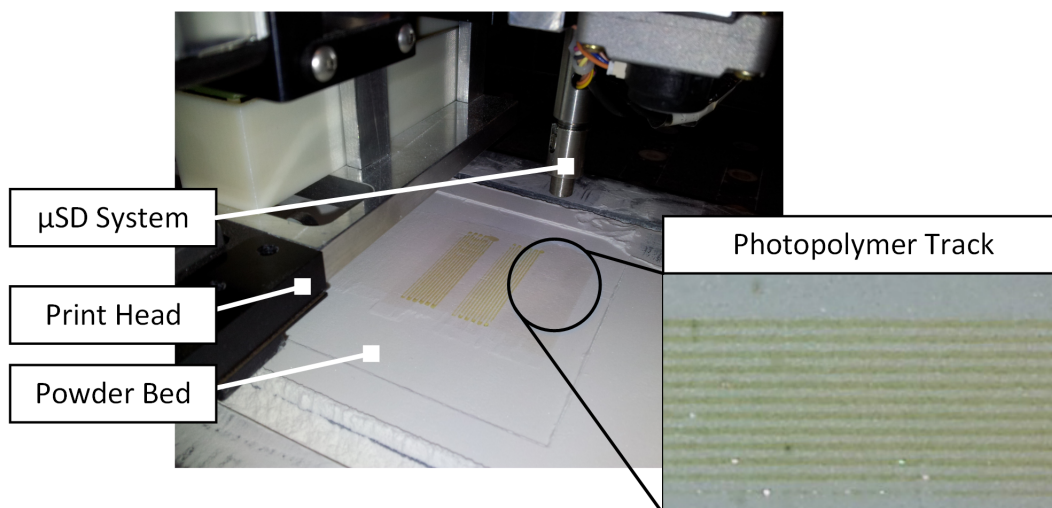


Figure 2.3: Multi-scale 3DP fabrication system showing the micro-syringe deposition system (μ SD) and a close-up view of a typical manufactured layer with the deposited photopolymer structure on the powder substrate

mill (US Stoneware, OH). The PVA powder was used as an additional binding agent to ensure green part strength.

2.1.1.4 Liquid Binder Material

In this study PVA in a 4 wt% solution in deionized water was used as the liquid binder. The binder was dispersed on the powder substrate during the additive manufacturing process by a piezo-based print head (XAAR1001, Xaar, Cambridge, UK).

2.1.1.5 Sacrificial Photopolymer Material

The proposed photopolymer solution was comprised of a monomer, a reactive dilutant mixed to achieve the desired injectability, and a photoinitiator (PI) to control the UV light sensitivity. Ethoxylated (10 bisphenol A diacrylate) (EBA) (Ebecryl 150, Cytec, NJ, USA) was used as a monomer. Cellulose acetate butyrate (CAB) (Sigma Aldrich, Oakville, Canada) was dissolved in acetone, with the solution functioning as the dilutant. Phenylbis(2,4,6-trimethylbenzoyl)phosphine oxide (Irgacure 819) (Sigma Aldrich, Oakville, Canada) was utilized as a PI. The components were utilized as received and mixed in solution at room temperature with a composition of 13 wt% CAB, 56 wt% EBA, 30.5 wt% acetone, and 0.5 wt% PI. A PI concentration of 0.5 wt% resulted in an acceptable photopolymerization time of approximately 3 s when exposed to a UV

light (SUV-01, Algitron, Woburn, MA, USA) radiated from a maximum distance of 20 *mm*. For the sake of simplicity, in this study, the solution is referred to as EBA*.

2.1.1.6 Sample Preparation

Samples were manufactured using the combined three dimensional printing and micro-syringe deposition (3DP- μ SD) methodology. To this effect, 25 layers (150 μ m in layer thickness, 50 x 50 mm^2 area) of CPP were first spread and bonded. Subsequently, the μ SD system was used to deposit four parallel tracks of the photopolymer on each sample under UV exposure. Sample A, intended for optical microscopy, was built with photopolymer tracks deposited at a head velocity of 2 *mm/s*, flow rate of 7 μ L/*min*, with tracks 4.5 *mm* in length, 2 *mm* apart. Sample B, intended for scanning electron microscopy, was built with photopolymer tracks deposited at a head velocity of 2 *mm/s*, flow rate of 7 μ L/*min*, with tracks 20 *mm* in length, 2 *mm* apart. The tracks in both samples A and B were covered with another ten layers of CPP as previously described. The green parts were sintered using an established post-processing thermal annealing protocol described below.

2.1.1.7 Post-processing Thermal Annealing of CPP

The green parts were left overnight and then exposed to a heat treatment to fully anneal them. Samples were air-annealed in a high-temperature furnace (EQ-GSL-1500X-40, MTI Corporation, Richmond, CA, USA). The heating rate was 10 $^{\circ}C/min$ from room temperature to 400 $^{\circ}C$, holding for 1 h, followed by another heating cycle of 10 $^{\circ}C/min$ up to 600 $^{\circ}C$ and a dwell time of 1 h, ending with another heating cycle of 10 $^{\circ}C/min$ to 950 $^{\circ}C$ with a dwell time of 1 h to ensure the formation of crystalline CPP and vaporization of any residual carbon from the structures. The cooling process was not controlled.

2.1.1.8 Geometry Characterization of Formed Channels

To ensure the formation of channels after the heat treatment protocol, a sample (sample A) with integrated channels was embedded in epoxy, dissected in vertical plane using a band saw, and polished to observe the formation of channels under an optical microscope (Olympus Japan BH Optical Microscope, Carsen Medical & Scientific Co. Ltd., Markham, Ontario, Canada). In addition, to better observe the quality of the formed channels after the heat treatment protocol,

another sample (sample B) with integrated channels was dissected in the longitudinal plane and observed using a scanning electron microscope (SEM; JSM-6460, Jeol, Akishima, Tokyo) at 20 *kV* accelerating voltage. To make the sample electrically conductive, it was sputter-coated with a 10 *nm* thick gold layer (Desk II, Denton Vacuum, LCC, Moorestown, NJ, USA).

2.1.1.9 Polymer Thermal Decomposition Characterization

One of the initial steps in validating the combined 3DP- μ SD methodology was to establish the thermal degradation pathway and degradation temperature profile of the photopolymer using differential scanning calorimetry (DSC)-thermo gravimetric analysis (TGA) (SDT Q600, TA Instruments, Grimsby, Canada) under the same heat treatment protocol used for curing the samples. The EBA* photopolymer solution was injected through the micro-syringe and UV-cured to form a small drop weighing 10 *mg*. The same experimental analysis was performed on 10 *mg* of pure PVA polymer to ensure that this binder polymer also fully degrades during the heat treatment protocol.

2.1.1.10 Surface Chemical Composition Characterization

For investigating the surface chemical composition of CPP structures after sintering, two types of heat-treated samples were prepared: a CPP-PVA baseline sample and a CPP-PVA-EBA* sample containing the photopolymer. The samples were 5 *mm* diameter and 2 *mm* in height, with one 4 *mm* long EBA* track deposited diametrically, on top for the CPP-PVA-EBA* sample. The chemical composition after sintering of the CPP-PVA and CPP-PVA-EBA* samples was analyzed using a field emission scanning electron microscope (FESEM) with energy dispersive X-ray spectroscopy (EDAX) (LEO1530, Carl Zeiss AG., Peabody, MA, USA). Due to the non-conductivity of samples, a 10 *nm* gold layer coating was deposited using a sputter coater (Desk II, Denton Vacuum, LCC, Moorestown, NJ, USA) prior to FESEM-EDAX analysis. Both samples were investigated at a magnification of x350. Two investigation areas were the focus of each sample, 250 and 50 μm^2 respectively.

2.1.1.11 Surface Material Composition Characterization

X-ray diffraction (XRD) was used to examine the material composition and crystallinity of the heat-treated CPP-PVA and CPP-PVA-EBA* samples to establish if there are any significant

differences introduced through the presence of the photopolymer during the fabrication process. The XRD analysis equipment (RAPID II X-ray Detector, Rigaku, TX, USA) was operated with 50 *kV* and 40 *mA*. The exposure time was 15 *s*, and the angle of interest was selected between 15° and 65°.

2.1.2 Results

2.1.2.1 Geometry Characterization of Formed Channels

As shown in Figure 2.4, the multi-scale 3DP- μ SD process resulted in the creation of channels inside CPP porous implants, which was one of the goals of this study. The SEM images depicted in Figure 2.5 show that, qualitatively, the tracks produced using the Multi-scale 3DP method are visible, and well defined. Some channels show variability in terms of channel width as seen in Figure 2.5 a) from approximately 275 to 225 μm , while the channel in Figure 2.5 b) is relatively constant in width at around 260 μm . The channels were originally spaced 2 *mm* apart; however, due to the part shrinkage during the post-processing heat treatment, the distance between channels was reduced by $\sim 12.5\%$.

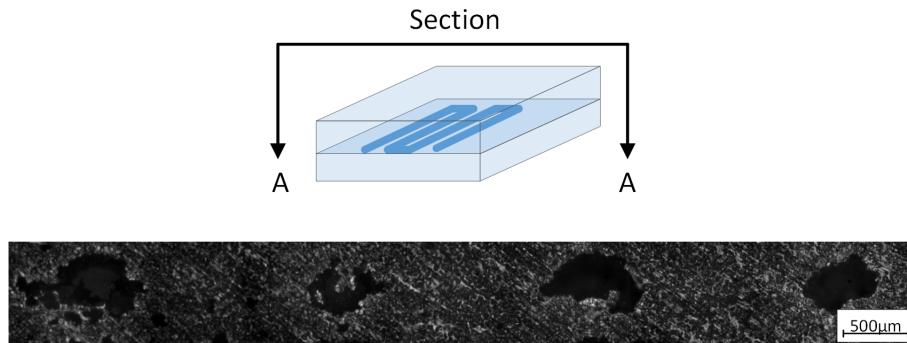


Figure 2.4: Cross-section of CPP part with integrated channels after heat treatment, viewed under an optical microscope. The part was encapsulated in epoxy, sliced in the vertical plane, and polished

2.1.2.2 Polymer Thermal Decomposition Properties

TGA was performed on the EBA* and PVA materials, respectively, to determine the change in weight of the sample as a function of increasing temperature and eventually identify temperatures necessary to initiate thermal degradation and also the maximum temperature necessary to complete the pyrolysis process. The resulting DSC-TGA analysis for the photopolymer is illustrated

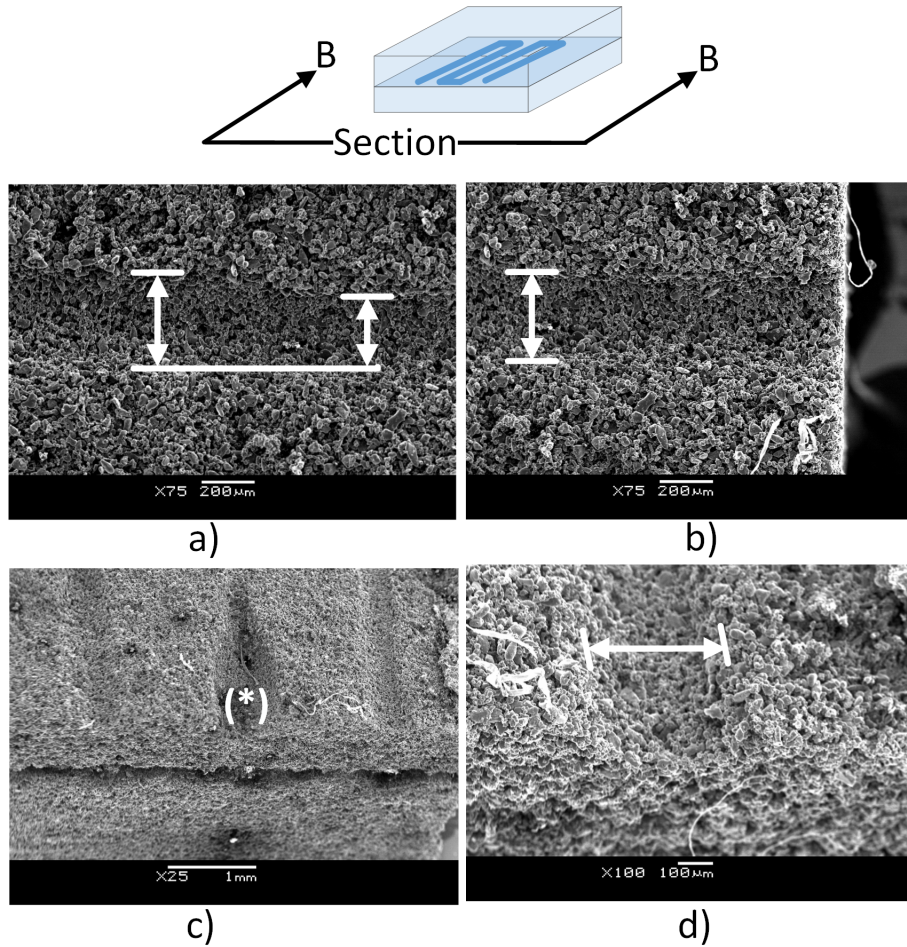
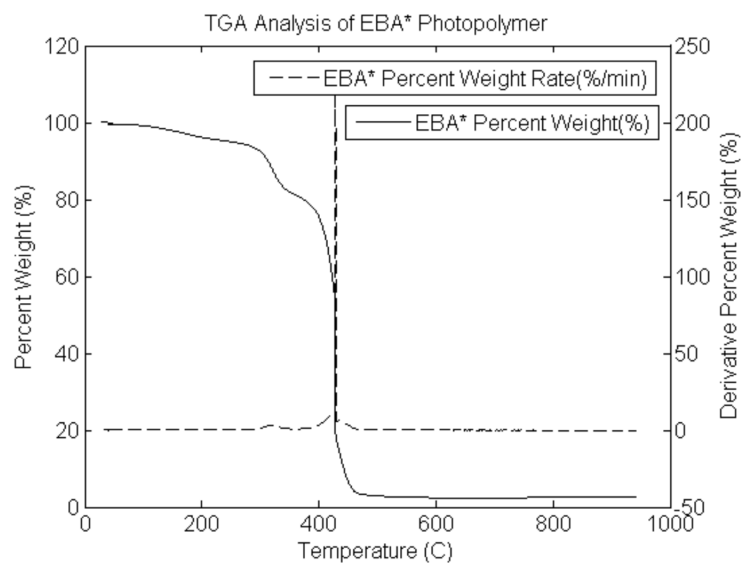
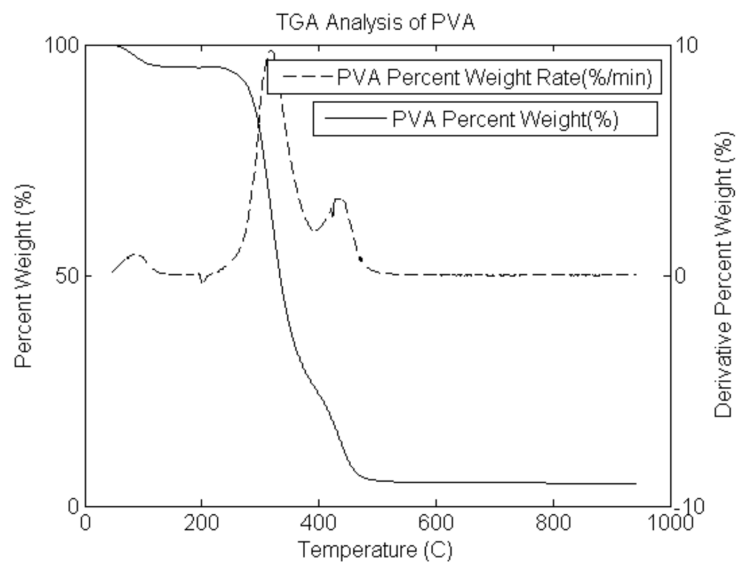


Figure 2.5: Cross-section of CPP part with integrated micro-channels after heat treatment viewed under SEM a), b) top view x75 magnification, and c), d) view from a 30 ° inclination with x25 and x100 magnifications respectively. (*) Shows a defect in the channel

in Figure 2.6 a). As can be seen, decomposition becomes significant after 300 °C, with an accelerated degradation region for EBA* at ~450 °C. The resulting DSC-TGA analysis for the PVA sample is illustrated in Figure 2.6 b). As observed, the degradation process becomes significant after 200 °C, and peaks in two regions between 300-325 °C and 400-425 °C, where the mass loss rate is accelerated. After 500 °C, both EBA* and PVA have been completely decomposed at a temperature significantly below the maximum thermal annealing temperature of CPP (950 °C).



a)



b)

Figure 2.6: Polymer thermal decomposition TGA results of a) EBA* and b) PVA

2.1.2.3 Surface Chemical Composition Properties

Figure 2.7 illustrates a result obtained through the FESEM-EDAX analysis. Table 2.1 summarizes the chemical composition of each sample in terms of weight percentage (wt%). The elements calcium (Ca), oxygen (O), phosphorus (P), and carbon (C) were present in both CPP-PVA and CPP-PVA-EBA* structures. Based on this analysis, it is apparent that no additional chemical elements are present in the sample produced using the proposed photopolymer. The wt% for

both trials 1 and 2 was very similar between samples. The discrepancies can be attributed to the small sampling size used to determine the results. Figure 2.8 shows the XRD results indicating that there are no significant differences in peaks and intensities between the two types of samples analysed. Based on these results, it can be inferred that there are no significant differences in chemical composition and crystallinity between the two samples, CPP-PVA and CPP-PVA-EBA*, and that the use of the EBA* photopolymer in the fabrication process does not introduce any by-products in the final part. The similarity of the XRD peak positions and intensities with samples investigated in a previous study [85] indicates that the resulting sintered CPP is β -CPP.

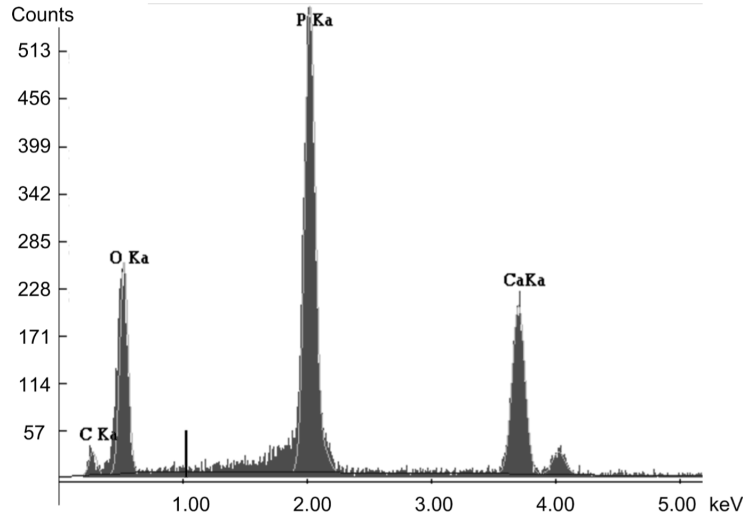


Figure 2.7: FESEM-EDAX analysis of a typical CPP-PVA-EBA* sample after thermal annealing using a $250 \mu m^2$ area

Table 2.1: FESEM-EDAX analysis results

Trials	Elements	CPP-PVA-EBA* (wt%)	CPP-PVA (wt%)
Trial 1), $250 \mu m^2$ analysis area for each sample	C	14.63	13.94
	O	44.10	41.17
	P	26.11	27.01
	Ca	15.16	17.18
Trial 2), $50 \mu m^2$ analysis area for each sample	C	14.05	15.25
	O	43.80	36.86
	P	26.56	28.37
	Ca	15.58	19.52

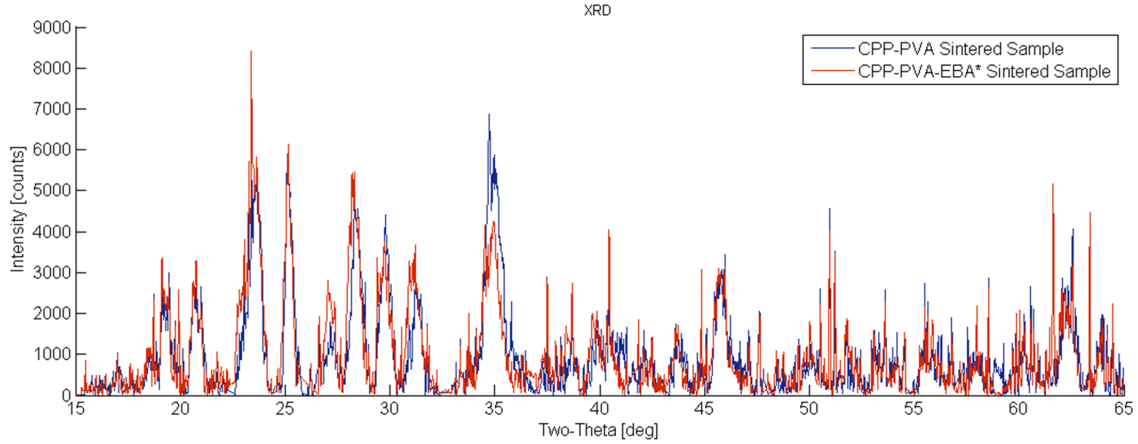


Figure 2.8: XRD analysis of CPP-PVA versus CPP-PVA-EBA* thermally annealed samples

2.1.3 Discussion

A combined 3DP- μ SD technique was developed to produce micro-channels within ceramic structures with an application in manufacturing bone substitutes. The focus of this study was on the characterization of the material system for achieving this task. The pattern of channels can be designed in a CAD environment, where the design of the channels may be developed based on the structural requirements of the final construct. The feature size of such channels has a direct effect on the performance of the implants. Based on biological functionality, the desirable channel feature should be in the range of 100-500 μm in size [69, 78, 79, 81]. To achieve nutrient transport and cell in-growth, the channels must be continuous and not clogged with the constitutive material of the structure. Any attempts towards forming very small features such as complex micro-channels and cavities embedded in parts using the available powder-based AM processes result in clogging, since loose powder becomes trapped within the channels or pores [31]. The newly developed multi-scale 3DP technique addresses this concern, as the resulting channels within CPP structures were continuous and included small features as shown in Figure 2.5. The results of these materials studies were reflective of samples produced without applying any control strategies, which are discussed in Section 2.2.

The cross-sectional shape of the channels depends on the geometry of the injected photopolymer tracks. In addition, it should be noted that the post-processing stage determines the final geometry of the channels based on powder particle size and shape. The powder particle size may have a profound impact on the geometry of the channels as it affects the sintering shrinkage [85, 86]. Parts shrink during sintering when exposed to high temperature and, consequently, the

geometrical features of the channels change as CPP particles start to form sinter-necks and may rearrange after photopolymer burn-off. Therefore the sintering protocol affects the size and shape of the features [85]. Furthermore, CPP structures made via multi-scale 3DP- μ SD are likely to shrink anisotropically if the shape of the particles has an aspect ratio greater than one [48, 48]. The different shrinkage characteristics in the directions parallel and perpendicular to constitutive layers may contribute to the irregular shape of the channels. In addition, the deposition of the photopolymer tracks on the powder substrate is affected by the flatness of the underlying powder layer spread by the counter-rotating roller which, in turn, is drastically affected by the particle size. The finer the particle size, the smoother the powder bed will be, which results in a more uniform photopolymer deposition. A study in Section 2.2 will focus on investigating the size and integrity of the channels by tuning the micro-syringe deposition parameters to control the feature size, and the UV light exposure time to control the shape integrity.

Material characterization studies including TGA and XRD analyses also revealed that there was virtually no residual by-product left from the photopolymer after the heat treatment stage. This issue is very important for evaluating the selected material system, since any residual pyrolysis by-products in the final part may adversely affect the biological response to the implant. A comparison between the TGA analysis for the two polymers shown in Figure 2.6 suggests that both followed the same degradation trend; however, the degradation of PVA occurred over a higher temperature range (200 to 450 °C), while EBA* was almost entirely degraded at around 450 °C. In both cases, the equilibrium weight does not stabilize to about zero, which may be due to the system errors associated with initial calibration, as no visible residue was found after the heating sequence [87]. However, the degradation curves stabilize significantly below the highest curing temperature of 950 °C, which is of interest for this application. In addition, XRD patterns of the CPP-PVA-EBA* and CPP-PVA samples confirm that the sacrificial photopolymer does not influence the crystalline structure of the post-processed part. It can be concluded that the material system was selected properly for the purpose of forming channels within bone substitute constructs.

2.2 Modelling and Experimental Validation of a Micro-syringe Deposition System for Dispensing Sacrificial Photopolymers on Particulate Ceramic Substrates

In this study, to address the feature size limitations of conventional 3DP manufacturing approaches, a combined 3DP- μ SD system was used capable of depositing micro-sized sacrificial polymeric networks on particulate surfaces throughout the construct with controlled feature size in the target range 100-500 μ m. The photopolymer was burned off in a furnace during thermal annealing of the green part to produce interconnected channels. This approach allows for control of internal features by avoiding loose powder material being trapped inside small features of larger-sized parts, which is of concern using current powder-based 3D printing techniques. In this work, the photopolymer deposition on a bioceramic powder substrate was studied experimentally and numerically based on a two-tier model developed for characterizing the fluid flow out of the μ SD nozzle as well as the final geometry of the tracks deposited on the powder layer. Experimental data were used to initialize and validate the model and also establish a characterization of this complex process. ³

2.2.1 Analytical Model Development

The deposited polymer feature size has a direct impact on the resulting porosity and interconnected channel geometry within the final part. It is therefore important to gain insight into the μ SD system behavior and predict the final feature size by developing a model. In this study, a two-tier model was developed to link the fluid injection parameters with the final geometry of the fluid deposited on the powder substrate as described analytically by the cascaded pressure-flow model and deposition geometry model described below.

2.2.1.1 Pressure-Flow Model

An approximate analytical model was used to estimate the flow of a fluid through the nozzle geometry based on the micro-syringe piston displacement. Table 2.2 lists and describes the parameters used in this work.

³The materials presented in Section are adapted from the author's published work [83]

Table 2.2: Nomenclature and associated equations

Term	Description	Equation
D_p	Dispenser piston diameter	2.1
A_p	Piston area	2.1
L_n	Nozzle length	2.2, 2.4
D_n	Nozzle inner diameter	2.3, 2.4
A_n	Nozzle cross-sectional area	2.2
ρ	Fluid density	2.2, 2.4
β	Fluid bulk modulus	2.1
τ_0	Yield stress	2.5, 2.3
τ	Shear stress	2.5
τ_w	Shear stress at nozzle wall	2.3, 2.4
$\dot{\gamma}$	Shear rate	2.5
K	Consistency index	2.5, 2.3
n	Flow behaviour index	2.5, 2.3
Z	Piston position	2.1
Q	Fluid flow leaving the nozzle	2.1, 2.2, 2.4
Q_u	Fluid flow in steady state under a unit of pressure	2.3, 2.2
V_o	Initial volume of fluid in the syringe	2.1
P	Pressure build-up inside the syringe barrel	2.1, 2.2, 2.3, 2.4
g	Gravitational constant	2.4
u	Average fluid velocity through nozzle	2.4
a	Deposition track width	2.6
h	Deposition track height	2.6
v_o, V_{xy}	Velocity of substrate wrt. nozzle	2.6
h_z	Length of tapered end of nozzle	2.6

For the dispensing system considered in this study, we assume that the process is isothermal, fluid properties are time-independent and the flow is fully developed laminar throughout the dispensing barrel and nozzle. The model presented by Chen and Kai [88] in their work on modelling of a positive-displacement fluid dispensing processes, can be adapted to this particular system and it is also relatively straightforward to implement in a programming environment. A schematic of this model is shown in Figure 2.9. The model described by Chen and Kai [88] assumes that non-Newtonian effects inside the syringe barrel are neglected if the dispensing barrel is large enough, minor losses are not significant at low velocities, the static pressure inside the syringe is uniform since the height of the fluid in the syringe is relatively small, the process is isothermal, and the fluid is compressible.

Considering the above assumptions, Equation 2.1 describes the general hydro-dynamic characteristics of the system, predicting the pressure build-up inside the syringe barrel due to the motion of the piston:

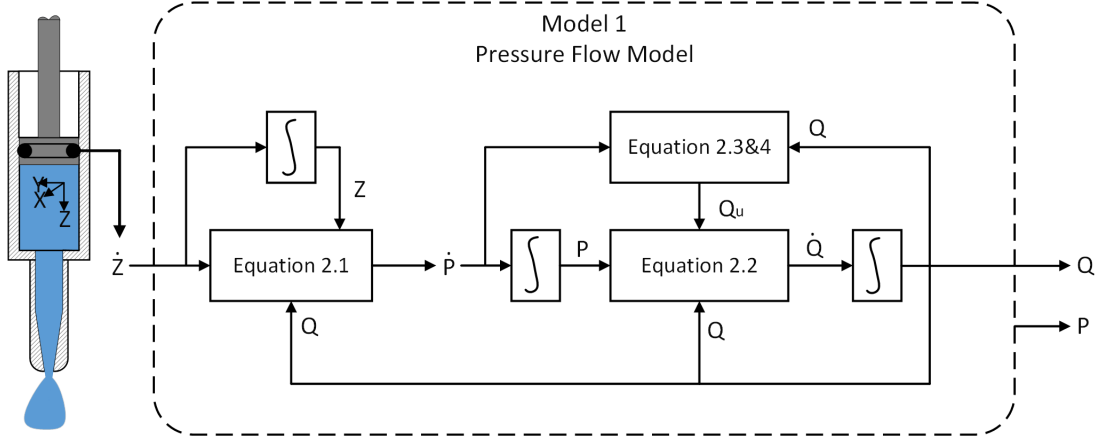


Figure 2.9: Schematic of pressure-flow analytical model

$$A_p \dot{Z} - Q = \left[\frac{V_o - A_p Z}{\beta} \right] \dot{P} \quad (2.1)$$

where V_o is the initial volume of fluid in the dispenser, A_p is the area of the piston, Z is the piston vertical displacement as shown in Figure 2.2 and Figure 2.9, β is the fluid effective bulk modulus under the assumption that there is no gas trapped in the fluid compartment, Q is the flow out of the nozzle and P is the pressure build-up inside the dispenser.

The Laplace function presented in Equation 2.2 was adapted by Chen and Kai [88] and describes the fluid flow rate leaving the nozzle driven by the pressure build-up inside the syringe barrel as previously derived in Equation 2.1. It applies under the assumption that the fluid flow is laminar, time-independent, there is a no slip condition at the nozzle wall, and that there are minimal compressibility effects inside the nozzle.

$$\frac{Q(s)}{P(s)} = \frac{Q_u}{\rho L_n \frac{Q_u}{A_n} s + 1} \quad (2.2)$$

Here, ρ is the fluid density, L_n is length of the nozzle, A_n is the nozzle outlet area, and Q_u is the steady state fluid flow under a unit of pressure calculated using the generalized power law as described in the model by Chen et al. [89] and stated in Equation 2.3 and Equation 2.4 below.

$$Q_u = \frac{\pi D_n^3}{8PK^{1/n}\tau_\omega^3} (\tau_\omega - \tau_o)^{(n+1)/n} * \left[\frac{n}{3n+1} \tau_\omega^2 + \frac{2n^2}{(2n+1)(3n+1)} \tau_\omega \tau_o + \frac{2n^3}{(n+1)(2n+1)(3n+1)} \tau_o^2 \right] \quad (2.3)$$

$$\tau_{\omega} = \frac{D_n}{4L_n}(P + L_n\rho g - 1.12\rho u^2) \quad (2.4)$$

For developing these equations, the Generalized Power Law Equation was used

$$\tau_{\omega} = \tau_o + K\dot{\gamma}^n \quad (2.5)$$

where τ_{ω} is the shear stress at the needle wall and is expressed in terms of the yield stress τ_o , the consistency index K , the shear rate $\dot{\gamma}$, and the flow behaviour index n . In the flow model, it is assumed that there are shear effects at the needle wall as described by Equation 2.4 [88] where u is the average fluid velocity through the needle [89]. The fluid properties are described in Section 2.2.2.3.

Equations 2.1 and 2.2 were discretized and used to approximate the pressure build-up and flow rate of fluid through the μ SD system based on the piston displacement. An illustration of the pressure-flow model architecture as implemented using Simulink (MATLAB 7.11, MathWorks, Natick, MA, US) is shown in Figure 2.9 and described in more detail in Appendix C. The outputs P and Q from this model are used as inputs in developing the secondary deposition geometry model. Table 2.3 lists the dispensing system geometrical parameters as used in this modelling framework. Fluid parameters are summarized in Section 2.2.2.3.

Table 2.3: Geometrical characteristics of dispensing system

Description	Parameter	Value
Piston diameter	D_p	3.36 mm
Nozzle length	L_n	15 mm
Nozzle exit diameter	D_n	250 μ m
Dispenser capacity	C	500 μ L

2.2.1.2 Deposition Geometry Model

A deposition geometry model was used to predict the cross-sectional geometry of the injected track. The inputs to this model are the pressure and flow parameters developed in the pressure-flow model as well as the velocity of the substrate, nozzle geometrical characteristics and fluid properties. Due to the deposition onto a porous surface, to account for liquid imbibition into the powder substrate, the effect of UV exposure latency has been quantified experimentally and can be used as a compensation factor in the modeling scheme. The proposed model was adapted

from work performed by Vozzi et al. [84] on characterizing geometrical features of extrusion-based polymer scaffolds and is used to approximate the width of the deposited patterns based on fluid conditions at the nozzle. In this model, it was assumed that the fluid pressure developed inside the syringe barrel is the main injection driving factor and that the dispensed polymer is a viscous Newtonian fluid. Additionally, the model assumed that the final cross-sectional profile of the dispensed feature can be approximated to be an elliptical segment as explained by Vozzi et al. [84]. Equation 2.6 describes the relationship between the line width and the applied fluid pressure P , velocity of the substrate, empirically measured feature height, and polymer viscosity:

$$a = \frac{\pi D_n P}{16 \mu v_o h h_z} \quad (2.6)$$

where a is the resulting line width, h is an empirical approximation of the height of the deposited polymer pattern, v_o is the velocity of the substrate with respect to the nozzle, D_n is the internal radius of the needle tip, μ is the viscosity of the polymer, and h_z is the length of the tapered zone of the capillary, which is estimated at 1 *mm*. This model assumes knowledge of the line height, which would ideally be a feedback measurement from a vision system. In this study, to test the feasibility of such a feedback scheme, the line height for each set of operation conditions was considered to be a stochastic variable with a probability distribution obtained through empirical data measured during an initialization phase where height measurements are taken at each desired combination of input parameters. The impact of this stochastic variable on the model output was studied by running a Monte Carlo simulation with 100 independent trials to determine the sensitivity of the model to the height parameter. The modeling results were then compared with experimental measurements to quantify the performance of the model. The combined model is illustrated in Figure 2.10.

2.2.2 Materials and Methods

2.2.2.1 Substrate Powder Material

In this study, the powder material used in the AM process was calcium polyphosphate (CPP) powder (supplied by University of Toronto, Toronto, ON, Canada) with an irregular particle shape and size between 75-150 μm blended with polyvinyl alcohol (PVA) powder (Alfa Aesar, Ward Hill, MA) with particle size <63 m. The powder mix utilized a composition of 90 wt%

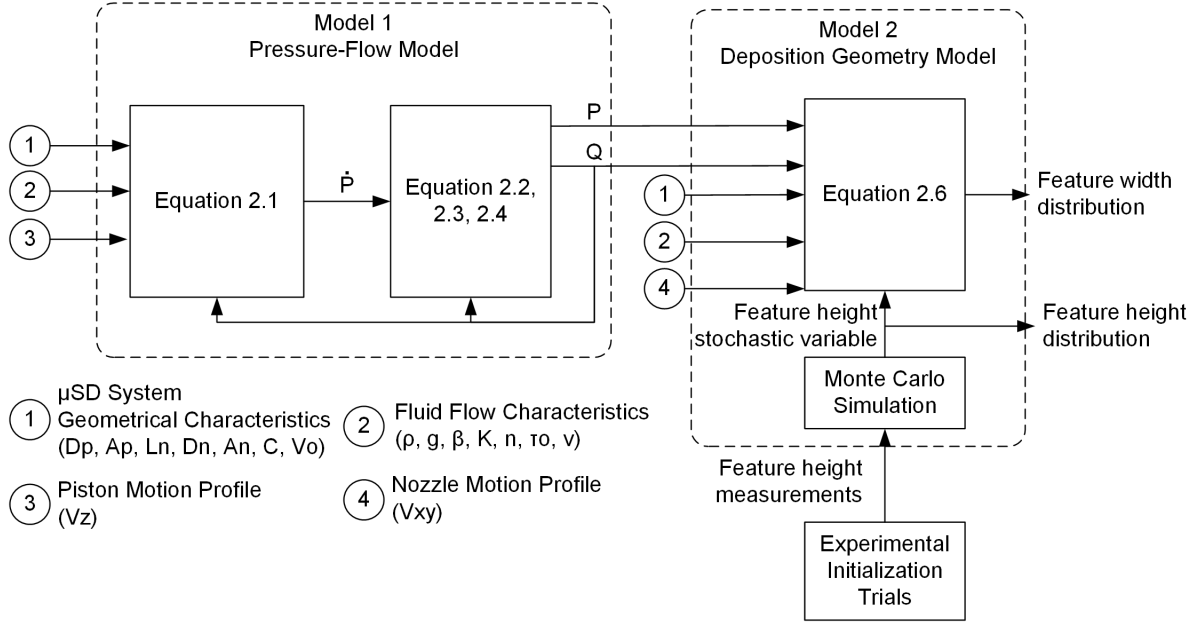


Figure 2.10: Block diagram presentation of the combined analytical pressure-flow model and stochastic deposition geometry model

CPP and 10 wt% PVA. The CPP:PVA blending procedure is described in Chapter 2, Section 2.1.1.3.

2.2.2.2 Liquid Binder Material

PVA with a 4 wt% solution in deionized water was used as the binder. The binder was dispersed on the powder substrate during the multi-scale 3DP process by a peizo printhead (XAAR 1001, Xaar, Cambridge, UK).

2.2.2.3 Sacrificial Photopolymer Material

The composition of the proposed photopolymer solution is described in Chapter 2, Section 2.1.1.5. A UV light (Solid State UV Spot Light, Algtron, Woburn, MA, USA) radiating from a maximum height of 10 mm was used to cure the photopolymer. For the sake of simplicity, in this study, the solution is referred to as EBA*. The solution was dispensed at room temperature. The flow behaviour of the photopolymer was characterized using a rheometer (DW-III Ultra, Brookfield Engineering Laboratories, Middleboro, MA, USA) at room temperature. The shear stress and shear rate data were curve-fitted using the generalized fluid power law to determine the viscosity

μ , consistency index K and flow behavior index n as seen in Figure 2.11.

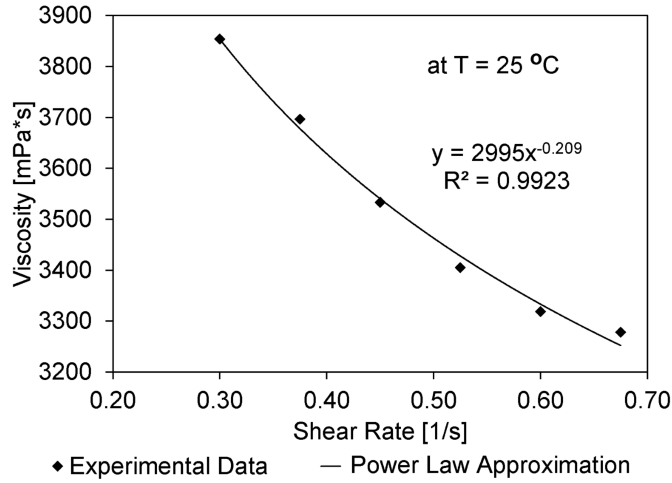


Figure 2.11: Photopolymer fluid power law approximation

Table 2.4 summarizes the fluid flow properties computed based on the power law approximation summarized in Figure 2.11. The viscosity μ was computed as the average over the shear domain. The consistency index K and flow behaviour index n were determined based on the approximated power law arguments, where K is the constant and n is the difference between unity and the approximated exponent argument obtained in the power law interpolation.

Table 2.4: Photopolymer fluid flow properties

Description	Parameter	Value
Viscosity	μ	3334 <i>mPas</i>
Consistency index	K	2995 <i>Pa</i>
Flow behaviour index	n	0.791

2.2.2.4 Sample Fabrication and Preparation

The selected variables of interest for this study in experimental and simulation trials were the μ SD piston linear velocity \dot{Z} and the velocity of the nozzle with respect to the substrate V_{xy} . The piston linear velocity \dot{Z} is directly proportional to the steady state fluid flow Q leaving the nozzle; therefore the effect of parameter \dot{Z} is equivalent to the effect caused by the the corresponding flow Q . The selected parameter values for Q and V_{xy} are shown in Table 2.5. These values were chosen based on a pre-screening experimental feasibility study performed in Section 2.1. The deposition was performed on 10 x 25 mm^2 and 2 mm thick particulate ceramic pre-fabricated

substrates manufactured based on a process described in 2.1.1.1. The nozzle deposition height was maintained at a distance of approximately one nozzle inner diameter of 250 μm as per recommendations found in the polymer deposition process described by Vozzi et al. [84].

Table 2.5: Selected variables in this study. An inconsistent deposition is one where the deposited tracks are intermittent and reliable measurements could not be obtained

Trial	Volumetric Flow $Q(\mu\text{L}/\text{s})$	Substrate Velocity $V_{xy}(\text{mm}/\text{s})$	Model Initialization $n(\text{samples})$	Model Validation $n(\text{samples})$	Empirical Observations
1	0.1104	1.0	6	6	Successful
2		1.5	6	6	Successful
3		2.0	6	6	Inconsistent
4		2.5	6	6	Inconsistent
5	0.1656	1.0	6	6	Successful
6		1.5	6	6	Successful
7		2.0	6	6	Successful
8		2.5	6	6	Successful
9	0.2208	1.0	6	6	Successful
10		1.5	6	6	Successful
11		2.0	6	6	Successful
12		2.5	6	6	Successful
13	0.2761	1.0	6	6	Inconsistent
14		1.5	6	6	Inconsistent
15		2.0	6	6	Inconsistent
16		2.5	6	6	Inconsistent

In this work, 16 samples were fabricated for each of the model initialization and model validation phases. Using the combined 3DP- μSD approach, the samples were manufactured by first printing rectangular pieces 10 x 25 mm^2 and 2 mm thick and subsequently depositing 20 mm long photopolymer tracks in a straight line on the CPP surface. On each sample, four tracks were deposited, each track with a different UV exposure latency duration t . The parts were then encapsulated in an epoxy resin. Height and width measurements of the polymeric tracks were taken by slicing the parts orthogonally at $n = 6$ locations, polishing and measuring as observed in Figure 2.12.

2.2.2.5 Sample Feature Geometrical Characterization

All samples were encapsulated in epoxy, dissected, and polished. The geometrical properties, height and width, of photopolymer features were measured using a calibrated camera (EDMUND Optics Inc., NJ, USA) at 2.3x magnification with a calibration factor of 2.7397. A total of ($n = 6$) measurements were taken for each experimental condition.

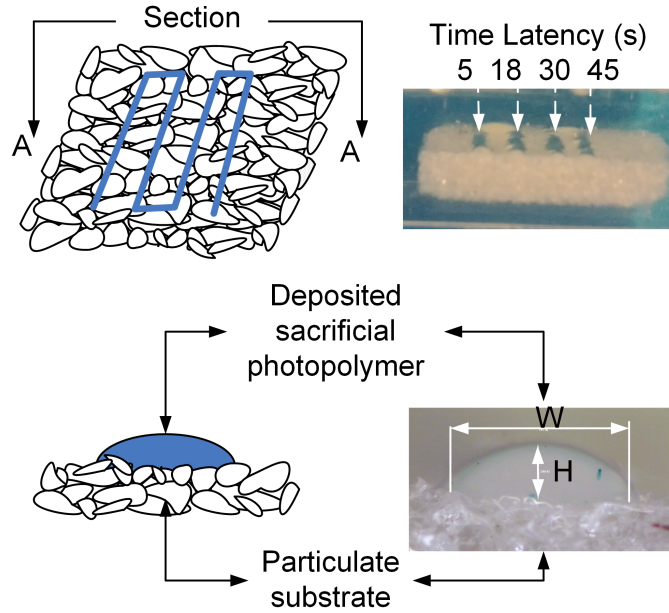


Figure 2.12: Fabricated sample with deposited photopolymer tracks

2.2.2.6 Sample Surface Roughness Characterization

The surface roughness, R_a , was estimated via image processing (MATLAB 7.11, MathWorks, Natick, MA, US) of five CPP surface profile images using a calibrated camera (EDMUND Optics Inc., NJ, USA) at 1x magnification with a calibration factor of 2.7397. The CPP samples for these measurements were not thermally annealed. More details on the methodology are described in Appendix D.

2.2.3 Results

2.2.3.1 Experimental Measurements vs. Simulated Outputs

Experimental data showed that tracks with width ranging from 200-500 μm and height from 20-200 μm were feasible, depending on system input variables. The measured widths from experimental trials were compared with the corresponding predictions from the developed model to investigate the model effectiveness. All comparisons between experimental and simulated data are for the 5 s UV latency exposure condition, as the UV light required at least 5 s to align with the deposition track. Figure 2.13 summarizes the experimental and corresponding simulated results at different fluid flow rates, under varying nozzle head velocities. The results show that the simulated outputs were considerably higher than the experimental measurements.

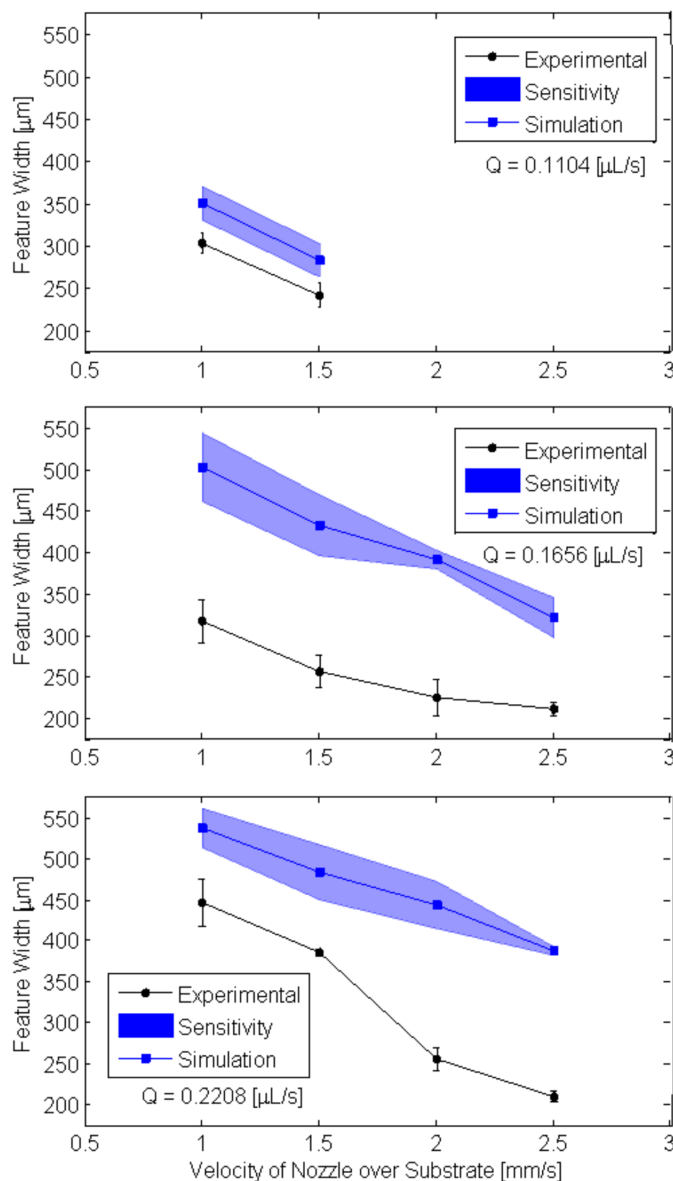


Figure 2.13: Track width with respect to velocity of the nozzle at different volumetric flows. Experimental vs. modelled data with a sensitivity domain based on Monte Carlo simulations

The simulated outputs in Figure 2.13 include a Monte Carlo sensitivity band illustrating the model sensitivity with respect to the stochastic feature height measurement obtained in the initialization trial. The model results were an average of 14%, 38%, and 38% higher for a fluid flow of $0.1104 \mu\text{L/s}$, $0.1656 \mu\text{L/s}$, and $0.2208 \mu\text{L/s}$ respectively. These values can be considered as adjustment factors, where the model simulation results are compensated based on the deviation between simulated and experimental results at each flow condition respectively.

2.2.3.2 Effect of UV Exposure Latency on Experimental Measurements

Four latency times were implemented: 5 s, 18 s, 30 s, and 45 s. The 45 s latency did not produce measurable or reliable samples, as the fluid infiltrated the porous substrate almost entirely. The results in Figure 2.14 show that a latency of 18 s decreases line width by an average of 17%, while a latency of 30 s decreases the line width by an average of 36% when compared with the line width measured at time latency of 5 s respectively.

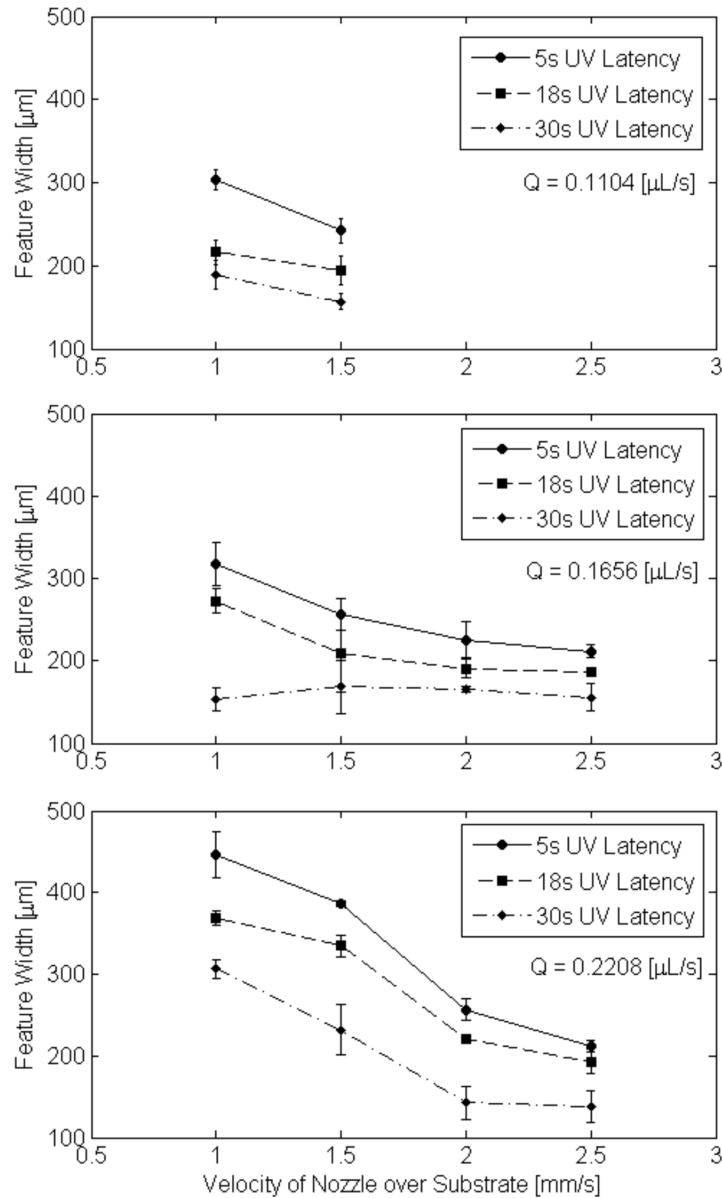


Figure 2.14: Graphs illustrate the effect of UV exposure latency of 5 s, 18 s, and 30 s on the experimental measured line width. An increase in UV latency decreases the observed width

2.2.3.3 Desired Feature Range vs. Experimental and Simulated Results

The main purpose of this work was to test the capability of the combined μ SD and 3DP system in producing features within a desired range. The desired feature range selected for this study is applicable for bone substitute implant manufacturing and is between 100 μm and 500 μm in diameter. Figure 2.15 illustrates the cross-sectional area of experimental and compensated simulated features versus the minimum and maximum threshold of cross-sectional areas corresponding to the desired features in the range 100-500 μm in diameter respectively.

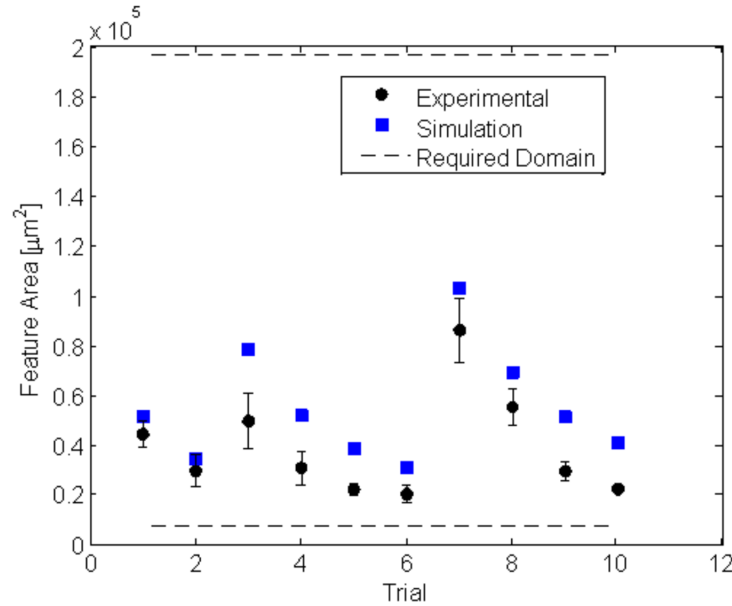


Figure 2.15: Cross-sectional area of experimental and simulated features versus the minimum and maximum threshold of cross-sectional areas corresponding to features in the range 100-500 μm in diameter respectively

2.2.3.4 Surface Roughness Results

The surface roughness was approximated using the arithmetic average of absolute values R_a to be $32.45 \pm 3.83 \mu m$. The data obtained for each one of the five CPP sample profile images is summarized in Appendix D.

2.2.4 Discussion

In this work, the focus was to characterize the geometrical features of polymeric tracks deposited onto porous substrates using a combined 3DP- μ SD novel approach. This method is superior to

the indirect approaches currently used in this field due to its simplicity, as it does not require extensive manufacturing steps such as developing a mold or a mask. In addition, it establishes a platform for incorporating micro-scale interconnected channels with a feature size of 100-500 μm inside ceramic parts, which is not possible with conventional 3DP methods. Experimental trials were performed to study the effect of operational input parameters such as velocity of the nozzle with respect to the substrate, volumetric flow throughput, and ultra violet exposure latency on the geometrical characteristics of the deposited photopolymer onto a particulate substrate. An analytical model was proposed to predict the process performance in terms of characterizing fluid flow and geometrical properties of the deposited feature. The experimental results were used to validate the model performance.

Experimental data showed that the μ SD process was capable of successfully depositing controlled features with a cross-sectional width between 200-500 μm and the height between 20-200 μm , which were within the desired range for various applications such as manufacturing of porous bone substitutes. Both the experimental and simulated results were within the lower spectrum of the desired feature range as seen in Figure 2.15. The feature size can be further increased by increasing the inner diameter of the nozzle in accordance with the mathematical model for deposition geometry used in this study. Furthermore, as seen in Figure 2.13, the width of tracks decreased when the process speed increased from 1 through 2.5 mm/s . Therefore, the nozzle size and velocity could be used to further control the desired feature width.

The experimental data were compared to outputs from the proposed model. The set of simulated and experimental results were summarized in Figure 2.13. The two sets of data show similar trends, with simulated data having consistently higher values than the experimental results. The lower experimental results can be attributed to factors such as liquid imbibition into the porous substrate, influenced by the fluid contact angle and surface tension, powder particle size and substrate pore size, fluid saturation levels [90], as well as the time latency between deposition and UV exposure.

The UV exposure latency was a considerable factor affecting the feature shape integrity after deposition as seen in Figure 2.14. Ideally, the photopolymer should be cured as it is being extruded through the nozzle in order to preserve the integrity of the deposited track. To avoid clogging, the UV spot light had a physical offset from the nozzle which required a time to re-align the deposition substrate with the UV spot light. Based on these experimental results, it can be concluded that the feature width can also be controlled by adjusting the latency, as a latency

of 18 s decreased line width by an average of 17%, while a latency of 30 s decreased the line width by an average of 36% when compared with the line width measured at time latency of 5 s, respectively.

Fluid migration and imbibition through the porous powder substrate are other factors that affect the shape integrity of the deposited feature. In this work, the surface roughness was estimated at $32.45 \pm 3.83 \mu m$, which is significant when depositing fluids in the μL scale. Fluid migration through porous powder media is influenced by the contact angle between fluid and substrate, liquid surface tension, powder particle size, and pore size as discussed by Lee et al. [90] in their study on the feasibility of constructing parts with interconnected channels using powder-based 3DP. Improved feature integrity can be achieved by increasing the viscosity of the fluid to reduce the rate of fluid imbibition, resulting in better shape preservation after fluid extrusion. This conclusion is supported by the theory developed by Batten [91] in his theoretical work on liquid imbibition in porous substrates. Based on these insights, it can be concluded that in this process, the feature width can also be controlled by changing the viscosity of the photopolymer. In this work, viscosity is proportional with the wt% of cellulose acetate butyrate (CAB) in solution; care must be taken to ensure safe injectability when increasing viscosity.

To better predict experimental results, the developed model can be enhanced by using compensation factors to account for fluid imbibition and UV exposure latency. Based on experimental and simulated data presented in Section 2.2.3.1, the compensation factors 14%, 38% and 30% corresponding to the 0.1104, 0.1656, and 0.2208 $\mu L/s$ flow rate, were not proportional with the fluid flow. This indicates that the rate of fluid imbibition may be influenced by fluid saturation levels in the powder substrate. The phenomenon of local fluid saturation is complex, especially through irregular porosities, and is influenced by the primary and secondary capillary flow as described by Markicevic et al. [92]. They have shown that liquid saturation in the direction of principal flow through a porous medium can have a complex profile depending on pore boundary conditions and interfacial forces. Based on these observations, the model proposed by Markicevic et al. [92] can be adapted and included in the present μSD model to predict the interaction between the powder substrate and photopolymer in the time span between deposition and photopolymerization. Using this approach, the compensation factors can be dynamically computed during runtime, rendering the model more relevant for deposition on a porous substrate.

2.3 Summary

This chapter focused on a novel combined 3DP- μ SD process for manufacturing porous structures with conformal internal conduits, with a direct application in manufacturing bio-ceramic bone substitutes with embedded micro-sized channels. This methodology addresses current obstacles associated with powder-based additive manufacturing in terms of embedding complex channels with a small feature size within the internal architecture of parts. In this work, it was shown that these obstacles can be addressed using the newly developed μ SD in conjunction with a 3DP methodology by producing porous ceramic structures with embedded internal channels with features in the range of ~ 100 - $500 \mu m$ which are desirable for bone repair. A CPP-PVA-EBA* material system was proposed for this manufacturing approach, to fulfil an important material design criterion, which is avoiding any significant pyrolysis residuals in the final product after the heat treatment protocol. The experimental analysis showed no significant signs of pyrolysis residuals left in the CPP structures, and no additional phase was observed in crystalline CPP material. As a result, the injectable photopolymer can effectively be used in a combined 3DP- μ SD process to act as a sacrificial element required for making complex micro-scale channels inside CPP ceramic structures.

The combined 3DP- μ SD methodology for depositing sacrificial substrates onto porous particulate substrates is a promising and novel approach for embedding interconnected macro-channels within parts. Using the combined 3DP- μ SD process, the internal feature characteristic can be controlled via process input parameters such as fluid flow, deposition nozzle speed, nozzle diameter, and UV exposure latency. It was shown that by using a $250 \mu m$ nozzle for a flow range between 0.1104 and $0.2208 \mu L/s$ and a nozzle velocity with respect to the substrate between 1 and $2.5 mm/s$, with a UV exposure latency of $5 s$, the resulting features range in width between 200 and $500 \mu m$ and in height between 20 and $200 \mu m$ on particulate substrates. The deposition process has been characterized experimentally and in simulation. The simulated results are approximately 14% to 38% higher than experimental results over the same input parameter range. The experimental results and relevant literature suggest that for a specific diameter of a deposition nozzle, the feature size can be controlled by changing the fluid flow, the process speed, the UV exposure latency, and the fluid viscosity. These factors are shown to affect the geometrical integrity of the sacrificial polymer post-injection and can be used as process control parameters. Furthermore, the developed model can be used in an online control paradigm, if

compensation factors are included, to account for the effects of depositing on a porous substrate. To conclude, the idea of using a combined 3DP and μ SD approach was validated experimentally. The complexity of controlling the μ SD process is amplified by the interaction of the sacrificial fluid with the porous substrate. To better understand and control the process, the μ SD system was modeled to quantify the effects of input parameters on the final geometrical characteristic of the feature and to devise future control strategies to improve the performance of the proposed system. A potential control strategy for the fluid-flow system is described further in Appendix E. The sacrificial element approach can be used in fabricating constructs with embedded conformal channels for other biomedical and industrial products manufactured via 3DP.

Chapter 3

Control of Functionally Graded Properties via Greyscale Binder Levels

The newly developed rapid layered manufacturing approach via multi-scale 3DP has a great versatility and can be tailored for a wide range of industrial and biomedical applications [5]. Emerging limiting aspects of conventional powder-based 3DP techniques are the use of only one powder size or powder type during manufacturing, the application of a constant compaction force during powder layer spreading, and the lack of control over the greyscale gradient of binder volume dispersed within each layer. These aspects impose limitations in manufacturing of porous scaffolds with functionally graded properties.

Researchers have investigated the liquid binder as a 3DP process parameter in terms of chemical composition [51, 52], concentration [51, 52, 53], and discrete saturation levels of binder volume [44, 54, 55] on the powder substrate. Vorndran et al. [52] analyzed different types of binder-powder substrate interactions occurring during the 3DP process to determine an appropriate binder solution that would produce samples with a desired compressive strength and porosity. To achieve a similar goal, the research done by Gbureck et al. [53] focused on studying the effect of varying the liquid binder concentration on substrate powders. In a different approach, Suwanprateeb et al. [54] used two binder saturation levels onto hydroxyapatite powder substrates and observed that an increased binder saturation level increased the flexural strength of green parts. Khalyfa et al. [51] analyzed the effect of a range of binder types and concentrations on

the green part hardening time of tetracalcium phosphate (TTCP). In all these investigations, the binder composition, concentration and saturation levels are kept homogeneous throughout the manufactured part, which is a limiting factor of conventional 3DP systems in constructing functionally graded materials.

In this chapter, the focus is to quantify the effect of greyscale binder distribution levels on two different layer thickness settings to establish a relationship between the binder volume dispersed and the resulting mechanical properties of samples. Ideally, using the newly developed multi-scale 3DP platform, the binder can be dispersed in a gradient of binder volume within each layer to achieve parts with functionally graded mechanical properties. The properties analysed were dimensional shrinkage after sintering, bulk porosity and density, and mechanical strength in uniaxial compression.

3.1 Materials and Methods

3.1.1 Powder Substrate Material

In this study, the powder material used in the multi-scale 3DP process is calcium polyphosphate (CPP) powder (University of Toronto, Toronto, ON, Canada) with an irregular particle shape and size between 75-150 μm blended with polyvinyl alcohol (PVA) powder (Alfa Aesar, Ward Hill, MA) with particle size $<63 \mu m$. The details of producing the homogeneous powder blend are described in Chapter 2, Section 2.1.1.3.

3.1.2 Liquid Binder Material

In this study, the liquid binder used in the multi-scale 3DP process is an aqueous solvent (ZbTM58, Z Corporation, Burlington, MA). The liquid binder was dispersed on the powder substrate during the multi-scale 3DP process by a peizo-based print head (XAAR, 1001 model, Xaar, Cambridge, UK). The ZbTM58 binder was used instead of PVA solution described in 2 to increase the lifespan of the printhead and to allow for a comparison of performance between the newly developed additive manufacturing system and the commercially available ZPrint 310 Plus (3D Systems, Burlington, MA) used in previous studies [48, 85].

3.1.3 Sample Fabrication

The multi-scale 3DP mechatronic platform was developed to address some of the current limitations of powder-based additive manufacturing via powder-droplet adhesion bonding as described in Chapter 1, Section 1.3. This system is equipped with a XAAR 1001 (XAAR, Cambridge, UK) piezoelectric printhead connected to a Hydra Ink Supply System (XAAR, Cambridge, UK) capable of dispensing a binder with an 8-bit greyscale color-map distribution at 360 dpi, with 7 drop sizes in the range of 6 to 42 pL . Printing was done at a height of 2.5 mm from the substrate, at a velocity of 100 mm/s , in a single swathe. In this study, the effect of different greyscale binder levels on the resulting part mechanical properties is studied. Binder greyscale level is defined here as the volume of binder per unit area with respect to the maximum droplet size of 42 pL , considered to be 100%. The novel multi-scale 3DP system was used to manufacture parts in a layer-by-layer fashion using proprietary software developed in LabView (National Instruments Corporation, Austin, TX, US), with a methodology as described in Chapter 2, Section 2.1.1.1.

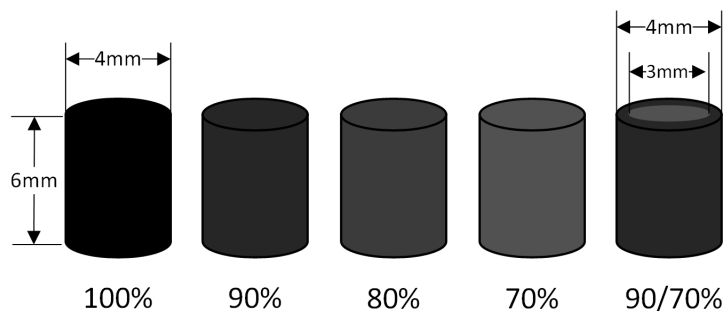


Figure 3.1: An illustration of samples manufactured with different greyscale levels of 70, 80, 90, 100, and 90/70% respectively, ($n = 10$)

Two categories of parts were produced, one with 190 μm and the other with 150 μm layer thickness respectively. The first category of layer thickness of 150 μm was selected to compare back to previous studies [48, 85] done using the conventional additive manufacturing ZPrint 310 Plus platform. The 190 μm layer thickness was selected as an upper limit based on the maximum layer thickness typically employed using this technology, which is approximately 200 μm . For each category, $n = 10$ green part CPP cylinders with a uniform grey scale of 70, 80, 90, and 100% respectively were produced in a layer-by-layer fashion. The cylinders were 4 mm in diameter and 6 mm in height. An additional set of cylindrical CPP parts were produced with 70% greyscale 3 mm interior and a 90% greyscale 1 mm contour and a height of 6 mm . These samples are referred to as 90/70% greyscale samples. Samples produced below 70% greyscale were not strong

enough to survive de-powdering. Figure 3.1 shows an illustration of the manufactured samples.

The green parts were then air-annealed in a high-temperature furnace (Lindberg/Blue M, ThermoScientific, Burlington, ON, Canada) with a pre-established heat treatment protocol [93]. The ambient humidity was controlled to 50%. The heating rate was 10 °C/min from room temperature to 400 °C, a dwell for 2 h, then 10 °C/min up to 500 °C, followed by 5 °C/min up to 630 °C, dwell for 1 h, ending with another heating cycle of 10 °C/min up to 950 °C with a dwell time of 1 h. Cooling was not controlled.

3.1.4 Dimensional Shrinkage Characterization

The green ceramic parts, when exposed to the heat treatment protocol, are expected to shrink [85, 48]. The parts were characterized dimensionally by measuring the diameter d and height h using a digital calliper (Absolute-Digimatic, Mitutoyo Corp., Japan) before and after thermal annealing. Dimensional data was used to measure shrinkage using the following Formula 3.1:

$$Shrinkage_x(\%) = \frac{x_G - x_S}{x_G} 100 \quad (3.1)$$

where x is the dimensional feature measured (height or diameter), G refers to the green part and S refers to the sintered part respectively.

3.1.5 Porosity Characterization

The bulk porosity of the sintered cylindrical samples was determined by ethanol displacement Archimedes principle based on the ASTM C373 standard. An ethanol bath kit (Sartorius YDK01 Density Determination Kit, Sartorius AG, Goettingen, Germany) and a precision micro-scale balance (APX-203, Denver Instrument, Bohemia, NY, US) were used to first determine the dry weight (W_{dry}) of each specimen. Each specimen was then immersed in ethanol and sonicated (VWR Ultrasonics Cleaner B2500A-DTH, VWR International, West Chester, PA, US) for one hour at 30 °C and soaked for another hour. Subsequently, the weight of the specimen suspended in ethanol (W_{susp}) was measured. Each specimen was then removed from ethanol, dabbed with a lint free cloth to remove excess ethanol and then weighed immediately to determine the wet weight (W_{wet}). The bulk porosity P_{bulk} and bulk density ρ_{bulk} were determined based on the formulae below, where the density of ethanol $\rho_{ethanol}$ was considered at room temperature to be

0.785 g/cm^3 and the theoretical density of non-porous CPP ρ_{CPP} was considered to be 2.850 g/cm^3 [76]. Equations 3.2 and 3.3 describe the formulae used to measure bulk density and bulk porosity.

$$\rho_{bulk} = \rho_{ethanol} \frac{W_{dry}}{W_{wet} - W_{susp}} \quad (3.2)$$

$$P_{bulk} = \left(1 - \frac{\rho_{bulk}}{\rho_{CPP}} \right) 100 \quad (3.3)$$

3.1.6 Uniaxial Compression Characterization

A population of $n = 10$ cylindrical samples for each category with 150 μm layer thickness and grey scale levels 70, 80, 90, 100, and 90/70% respectively, of dimension 4 mm diameter and 6 mm tall, were subjected to uniaxial compression using a calibrated 1-kN load cell, at a loading rate of 0.2 mm/min (Instron 5548 Micro-Testing, MA). A similar population of samples, with a layer thickness of 190 μm and grey scale levels 70, 80, 90, 100, and 90/70% respectively were subjected to uniaxial compression using a calibrated 5-kN load cell, at a loading rate of 0.2 mm/min (Instron 8501 Micro-Testing, MA).

3.1.7 Statistical Analysis

Porosity, density, shrinkage, and compression strength data are reported as means and standard deviation. A one-way ANOVA single factor analysis of variance was used to evaluate the statistical significance of measurements, followed by Tukey-Kramer *post hoc* pairwise comparisons to identify the so-called honest significant differences (HSD) between classes of samples using STATISTICA V12 (StatSoft, Tulsa, OK). A significance level of $p < 0.05$ was considered. A population of $n = 10$ was considered for all categories of samples respectively.

ASTM C1239-07 was used to analyse and report the performance of ceramics under uniaxial compression that fail in a brittle fashion. The Weibull distribution described in Equation 3.4 was used to predict the probability of failure of the ceramic part [94] as well as to provide a statistical means of evaluating the quality of the measured data set:

$$P(\sigma) = 1 - \exp \left[- \left(\frac{\sigma}{\sigma_o} \right)^m \right] \quad (3.4)$$

where P is the failure probability, σ_o is the central value or scale parameter showing the Weibull characteristic strength describing the value up to which 63% of samples are expected to fail, and m is the shape parameter, also known as the Weibull modulus. The Weibull modulus is a measure of reproducibility in the measured samples [81]. In this work, a population of $n = 10$ was considered for all categories of samples. Equation 3.5 was used as a probability estimator, where i is the corresponding rank of the sample measurement.

$$P(\sigma) = 1 - \frac{(i - 0.3)}{(n + 0.4)} \quad (3.5)$$

3.2 Results

3.2.1 Dimensional Shrinkage Results

The physical shrinkage of parts has been determined by comparing the diameter d and height h of parts before and after sintering. The results for each category with 150 μm and 190 μm layer thickness respectively and type of parts (70, 80, 90, 100, and 90/70% greyscale respectively) are summarized in Table 3.1. A statistical significance of ($p < 0.05$) illustrates that there is an effect of binder greyscale level on shrinkage for the 150 μm layer thickness category. For the 190 μm layer thickness category, the *post hoc* HSD comparisons showed pairwise similarities, showing a weak effect of binder greyscale level on this category of samples.

Table 3.1: Dimensional shrinkage (%) in diameter d and height h of two categories of parts, with 150 and 190 μm layer thickness respectively, printed at 70, 80, 90, 100, and 90/70% greyscale levels, ($n = 10$)

150 μm layer thickness		
Greyscale	$Shrinkage_d(\%)$	$Shrinkage_h(\%)$
70%	6.8 ± 2.4	8.9 ± 3.6
80%	7.5 ± 2.2	8.5 ± 2.5
90%	11.2 ± 1.3	11.1 ± 1.9
100%	9.2 ± 1.7	10.1 ± 2.9
70/90%	10.0 ± 1.2	11.5 ± 2.0
190 μm layer thickness		
Greyscale	$Shrinkage_d(\%)$	$Shrinkage_h(\%)$
70%	8.2 ± 1.9	10.9 ± 3.6
80%	8.4 ± 1.7	10.4 ± 3.5
90%	6.6 ± 3.6	10.6 ± 4.1
100%	6.9 ± 1.5	10.6 ± 4.4
70/90%	7.8 ± 0.7	8.1 ± 3.5

3.2.2 Bulk Porosity and Density Results

The bulk density and bulk porosity were calculated using the Archimedes principle as described in Section 3.1.5. The porosity results for cylindrical samples manufactured using 150 and 190 μm layer thickness respectively and 70, 80, 90, 100, and 90/70% greyscale respectively are summarized in Figure 3.2. The bulk density results are summarized in Table 3.2. Similarly to shrinkage findings, a statistical significance of ($p < 0.05$) illustrates that there is an effect of binder greyscale level on bulk density and porosity for the 150 μm layer thickness category. For the 190 μm layer thickness category, the *post hoc* HSD comparisons showed a weak effect of binder greyscale level on density and porosity.

Table 3.2: Bulk density of two categories of parts, with 150 and 190 μm layer thickness respectively, printed at 70, 80, 90, 100, and 90/70% greyscale respectively, ($n = 10$)

Greyscale	$\rho_{bulk}(g/cm^3)$ 150 μm Layer thickness	$\rho_{bulk}(g/cm^3)$ 190 μm Layer thickness
70%	1.47 ± 0.06	1.33 ± 0.05
80%	1.46 ± 0.04	1.39 ± 0.04
90%	1.59 ± 0.05	1.33 ± 0.04
100%	1.61 ± 0.04	1.38 ± 0.07
70/90%	1.46 ± 0.04	1.40 ± 0.10

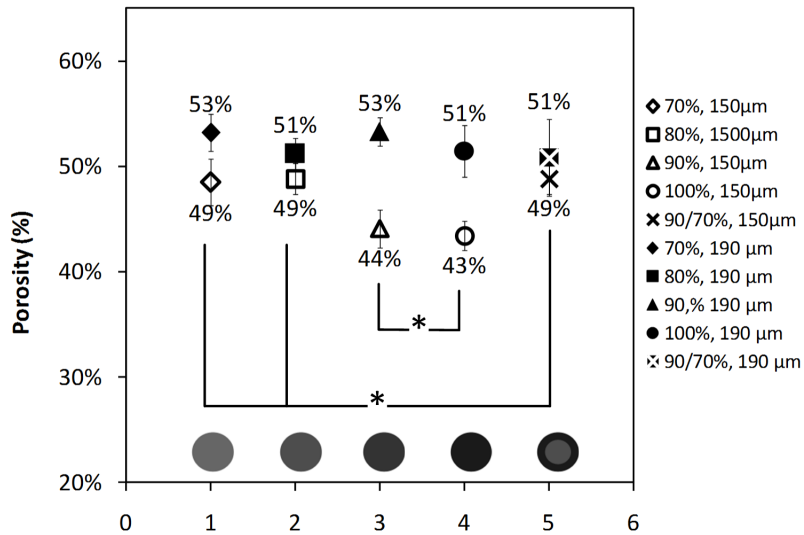


Figure 3.2: Bulk porosity characteristics of cylindrical samples with layer thickness of 150 μm and 190 μm , at greyscale of 70, 80, 90, 100, 90/70% respectively. ($n = 10$). (*) Illustrates Tukey HSD statistical pairwise similarities

3.2.3 Mechanical Strength - Uniaxial Compression Results

The uniaxial compression test results for cylindrical samples manufactured using 150 and 190 μm layer thickness and 70, 80, 90, 100, and 90/70% greyscale respectively are shown in Table 3.3, along with the corresponding Weibull moduli, where σ_c is the uniaxial compressive strength, ε_c is the nominal corresponding strain, E_T is the tangent modulus, m is the Weibull modulus.

Table 3.3: Mechanical compression parameters for samples with layer thickness of 150 and 190 μm , printed at 70, 80, 90, 100, and 90/70% greyscale level respectively, ($n = 10$)

Parts manufactured at 150 μm layer thickness				
Method	$\sigma_c(\text{MPa})$	$\varepsilon_c(\%)$	$E_T(\text{MPa})$	$m(R^2)$
Greyscale 70%	4.83 ± 1.30	3.28 ± 0.60	208.4 ± 39.3	3.83 (0.94)
Greyscale 80%	6.77 ± 1.86	3.38 ± 0.80	274.6 ± 44.5	3.57 (0.96)
Greyscale 90%	13.37 ± 1.73	4.26 ± 0.86	412.0 ± 94.6	8.05 (0.83)
Greyscale 100%	13.20 ± 2.30	3.56 ± 0.85	495.4 ± 62.8	6.09 (0.97)
Greyscale 70/90%	15.53 ± 1.90	4.04 ± 0.69	625.7 ± 69.7	7.52 (0.76)
Parts manufactured at 190 μm layer thickness				
Method	$\sigma_c(\text{MPa})$	$\varepsilon_c(\%)$	$E_T(\text{MPa})$	$m(R^2)$
Greyscale 70%	3.75 ± 0.44	3.24 ± 0.79	158.2 ± 31.2	9.12 (0.96)
Greyscale 80%	4.17 ± 0.61	3.04 ± 0.64	136.6 ± 43.2	7.00 (0.74)
Greyscale 90%	3.73 ± 0.35	2.79 ± 1.12	145.2 ± 34.8	11.30 (0.93)
Greyscale 100%	3.37 ± 0.62	3.22 ± 0.90	143.5 ± 38.9	5.88 (0.85)
Greyscale 70/90%	2.82 ± 0.51	3.91 ± 0.98	96.5 ± 27.8	5.91 (0.91)

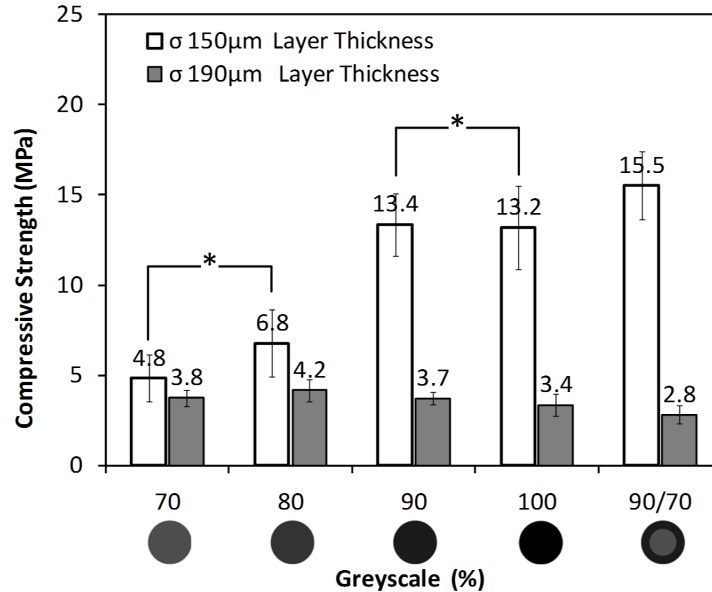


Figure 3.3: Ultimate compressive strength of samples with layer thickness of 150 μm and 190 μm , at greyscale levels of 70, 80, 90, 100, and 90/70% respectively, ($n = 10$). (*) Illustrates Tukey HSD statistical pairwise similarities

Figure 3.3 shows a graphical comparison between ultimate compressive stress results obtained for the category of parts printed with 150 and 190 μm layer thickness. For the 190 μm layer thickness category, aside for the 90/70% samples, the HSD statistical pairwise analysis showed that the greyscale level had limited effect on the σ_c , ε_c and E_T . For the 150 μm category, a statistical significance ($p < 0.05$) illustrates that there is an effect of binder greyscale level on mechanical performance of samples. Figure 3.4 shows the linear regression for the Weibull distribution used to predict the probability of failure of the ceramic parts.

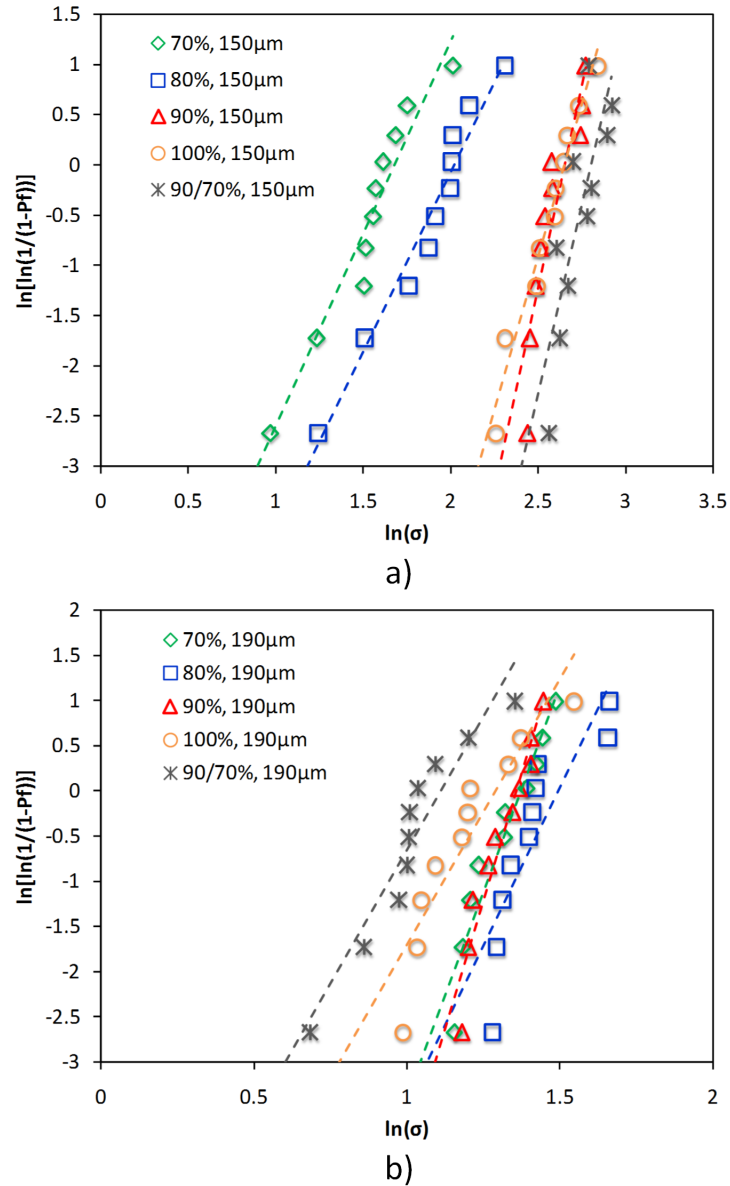


Figure 3.4: Weibull failure probability functions and linear interpolations for compressive strength of samples printed with layer thickness of a) 150 μm and b) 190 μm , ($n = 10$)

3.3 Discussion

An advanced multi-scale 3DP platform was developed to address some of the current limitations of powder-based AM technology. The novel system is capable of discrete 8-bit, 256 level greyscale control of binder volume jetted onto the powder substrate. In this study, the effect of varying the greyscale levels dispersed on two categories of powder layer thickness on mechanical properties was investigated. The properties under investigation were dimensional shrinkage after heat annealing, bulk porosity and bulk density, and mechanical strength in uniaxial compression.

The diametral shrinkage measurements had a high standard deviation for both categories of samples manufactured with 150 and 190 μm layer thickness respectively; however, it can be observed that the average diametral shrinkage measurements listed in Table 3.1 follow the same trends as the corresponding compressive strength illustrated in Figure 3.3. The effect of greyscale showed significance ($p < 0.05$) on samples manufactured at 150 μm layer thickness. A significant diametral shrinkage of $11.2 \pm 1.3\%$ occurred in samples manufactured at 150 μm layer thickness and 90% greyscale level. Based on pairwise *post hoc* HST analyses, the greyscale level did not seem to have a significant impact on the diametral and height shrinkage for the category of parts with a layer thickness of 190 μm . The high statistical variability in dimensional shrinkage measurements was in part caused by the fact that the de-powdering of green parts was done with excessive care due to concerns of maintaining part integrity.

Bulk density and bulk porosity are inter-dependent variables. The porosity measurements shown in Figure 3.2, and implicitly the bulk porosity summarized in Table 3.2, illustrate that the grey scale level had no significant impact on the resulting porosity and density for samples with a layer thickness of 190 μm , where the porosity ranged between $50.8 \pm 3.6\%$ and $53.2 \pm 1.8\%$ and bulk density ranged between $1.33 \pm 0.05 g/cm^3$ and $1.40 \pm 0.10 g/cm^3$. The *post hoc* pairwise analysis for this category of samples corroborates this finding. This suggests that the jetted binder volume in each layer was not sufficient for this category of samples to result in proper powder wetting and to infiltrate the powder layer enough to produce a considerable layer densification [5]. The category with the lowest porosity, and consequently the highest values of bulk density, corresponded to the 150 μm layer thickness. For this category of samples, the binder greyscale level had a noticeable impact on the overall mechanical properties. Within this category, the sample printed with 100% greyscale had the highest bulk density at $1.61 \pm 0.04 g/cm^3$ and lowest corresponding porosity at $43 \pm 1.38\%$. In this case, the lower layer thickness combined

with the highest greyscale level allows for proper binder adsorption, creating an adhesive effect by glueing the adjacent powder particles together in an agglomerate [64, 95].

The uniaxial compression results summarized in Table 3.3 and illustrated in Figure 3.3 show that the greyscale level did not have a significant effect on the parts manufactured with a layer thickness of $190 \mu m$, where the uniaxial compressive strength ranged between $2.82 \pm 0.51 MPa$ and $4.17 \pm 0.61 MPa$. This conclusion is also supported by pairwise **post hoc** HST analyses. This is due to improper layer wetting [5]. When the printing layer thickness is large, as the binder lateral infiltration is higher than the infiltration in the vertical direction, the adhesion between layers may not be sufficient to ensure good green part integrity [96]. This resulted in poor mechanical properties for this category of samples.

For samples with layer thickness of $150 \mu m$ ($p < 0.05$), there is a general increase in compressive strength with greyscale level, from $4.83 \pm 1.30 MPa$, corresponding to 70% greyscale, up to $13.37 \pm 1.73 MPa$ and $13.20 \pm 2.30 MPa$ corresponding to greyscale levels 90 and 100% respectively. The highest compressive strength of $15.53 \pm 1.90 MPa$ occurred in parts printed at greyscale level 90/70%. These results can be explained by saturation effects of liquid binder in the porous powder media substrate [90], as well as by understanding the packing orientation of particles in the 3DP process [48]. Saturation is defined as the ratio of the binder volume to available pore volume in the powder substrate [90]. When the powder substrate is over-saturated, the capillary effect initially allows the binder to infiltrate the powder laterally and horizontally. Provided that the curing rate of the binder allows [5], when the vertical infiltration meets the previous underlying layer, the binder is impeded from further spreading vertically [64]; therefore, the excess binder may disturb the orientation of particles in the powder layer by forming agglomerates and by pursuing spread in the horizontal direction. The paper by Shanjani et al. [48] suggests that the irregular-shaped CPP particles with an aspect ratio > 1 have a preferred particle orientation in the powder layer, as dictated by the direction of spread imposed by the counter-rotating roller. This orientation has an impact on mechanical properties. At $150 \mu m$ layer thickness, for the 90% and 100% greyscale samples, the amount of jetted binder may be over-saturating the substrate and disturbing the particle orientation within the substrate. These samples are therefore not superior in strength to the parts manufactured using a 90/70% binder greyscale level, even though they do show a slightly higher bulk density and lower porosity, where common knowledge suggests that a higher density results in improved mechanical properties [5, 76].

The compressive strength measurements for parts manufactured using 150 μm layer thickness correspond with the requirements for cancellous bone (4-12 MPa) [69], however they are well under the requirements for cortical bone (130-180 MPa) [69]. The range of compressive strength measurements reported for CPP parts manufactured using the new multi-scale 3DP machine (3-16 MPa) are below the values reported for CPP manufactured using a ZPrinter 310 Plus (ZCorp) machine (34-50 MPa) [48, 85]. This discrepancy is due to the fact that the counter-rotating roller parameters (linear and rotational velocity) have not been tuned in the multi-scale 3DP machine to improve the powder compaction force. The values of the Weibull modulus m reported for the CPP samples fabricated using the multi-scale 3DP machine in this study (4-11) are comparable with Weibull moduli reported for calcium phosphate samples in literature (3-9) [97] and (5-10) [48] indicating good reliability in measurements presented in this work, as the Weibull modulus is inversely proportional with data scatter. A higher m correlates with a good distribution of pore distribution within the part and good repeatability [98].

The porosity obtained in this work (43-54%) is between the desired range for cancellous bone (50-90%) and cortical bone (3-12%) [81]. The porosity range for CPP samples obtained using the newly designed multi-scale 3DP methodology (43-54%) is higher than the porosity obtained for CPP using the conventional 3DP approach (35-38%) using a ZPrinter 310 Plus (ZCorp) [48, 85]. This discrepancy outlines the need for further parameter optimization in the newly developed machine, intended for future work. The bulk density obtained in this work (1.3-1.6 g/cm^3) is between the desired range for cancellous bone (0.30 g/cm^3) and cortical bone (1.85 g/cm^3) [81]. These results illustrate that this methodology shows promise in developing bone substitutes.

3.4 Summary

A multi-scale 3DP additive manufacturing system was developed to achieve control of functionally graded properties within porous structures. The validity of the system was tested on manufacturing porous bone substitutes. In this chapter, the greyscale binder dispersion capability was investigated to quantify the effect of different binder volume dispersion levels shrinkage, porosity, bulk density, and uniaxial compressive strength. The greyscale levels and layer thickness have proven to have an effect on mechanical properties. The greyscale binder dispersion is a valid 3DP parameter in controlling the functionally graded properties of porous structures manufactured using the proposed approach.

Chapter 4

Control of Functionally Graded Properties via Multi-powder Composition

This chapter addresses the feasibility of fabricating porous constructs with functionally graded structural properties by implementing multiple powder sizes during the additive manufacturing fabrication process. The newly developed multi-scale 3DP system allows for the capability of selecting between three powder feed compartments during runtime to produce layers with different material composition at selected locations throughout the part. To the author's knowledge, such a system is not commercially available, nor is it discussed in the literature thus far. This chapter presents an initial study of the multi-powder manufacturing capability, with further considerations for layer spreading and printing parameter optimizations as the focus of future work. To evaluate the performance of the multi-powder system configuration, two powder particle sizes were selected, CPP bioceramic powder with 75-150 μm particle size (hereafter referred to as large), and <75 μm particle size (hereafter referred to as small). Three categories of parts were manufactured, with small, large and dual (50/50) powder composition respectively. The structural properties (porosity, geometry, and sinter neck consistency) and mechanical properties (compression strength behaviour) of the samples were analysed to determine the impact of powder particle size on the final part characteristics. Figure 4.1 illustrates the multiple powder bed capability of the newly developed multi-scale 3DP machine used in this investigation.

In the literature, the effect of powder particle size on the physical, structural and mechan-

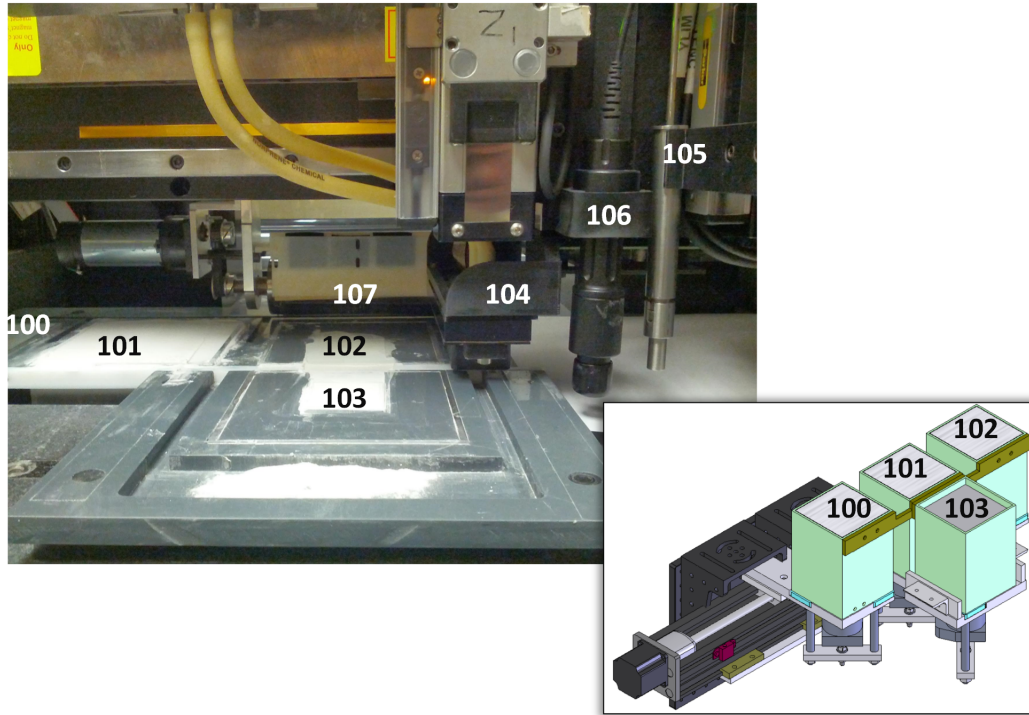


Figure 4.1: An illustration of the newly developed multi-scale 3DP machine showing the powder beds integrated in the system. (100, 101, 102) Feed bed compartment modules, (103) Build bed module, (104) Printhead, (105) Micro-syringe deposition module, (106) UV curing module, (107) Roller module

ical properties of the constructs has been reported by Will et al. [62], where hydroxyapatite (HA) homogeneous powder compositions with different weight ratios of coarse, average $50 \mu\text{m}$ particle size, and fine powder, average $4 \mu\text{m}$ particle size, were used in the 3DP process, with resulting porosity between 30% to 60%. It was found that the parts with the highest content of fine powder had the highest compressive strength. Other investigations [96, 99] focused on improving the surface finish of parts by integrating such bimodal powder size compositions in the additive manufacturing process, with positive results. These preliminary investigations show that the powder particle size distribution has an effect on mechanical and structural properties, and furthermore, on the three dimensional finish of the printed parts. It is therefore desirable to be able to manipulate the powder particle size within specific layers during the fabrication process in order to control the functionally graded properties of the final part.

4.1 Materials and Methods

4.1.1 Powder Substrate Material

Calcium polyphosphate (CPP) powder (University of Toronto, Toronto, ON, Canada) with an irregular particle shape was used in this study. Two categories of powder were used, large CPP with size between 75-150 μm and small CPP $<75 \mu m$, each blended with polyvinyl alcohol (PVA) powder (Alfa Aesar, Ward Hill, MA) with particle size $<63 \mu m$. The powder blend preparation process is described in Chapter 2, Section 2.1.1.3.

4.1.2 Liquid Binder Material

In this work, the liquid binder used in the multi-scale 3DP process is an aqueous solvent (ZbTM58) (Z Corporation, Burlington, MA). The binder was dispersed on the powder substrate during the multi-scale 3DP process by a peizo-based print head (XAAR, 1001 model, Xaar, Cambridge, UK).

4.1.3 Powder Size Characterization

The powder size was determined by placing a thin layer of powder on a conductive substrate and using secondary electron emission scanning electron microscopy (SEM, JSM-6460, Jeol, Akishima, Tokyo) at 20 kV accelerating voltage to visualize the particles. To make the powder electrically conductive, it was sputter-coated with a 10 nm thick gold layer (Desk II, Denton Vacuum, LCC, Moorestown, NJ, USA). The particle length, across the longest orientation and the width, perpendicular to the length, were recorded using the SEM AnalySIS tool.

4.1.4 Sample Fabrication

The multi-scale 3DP system was used to manufacture three categories of samples, with small, large, and dual powder composition as seen in Figure 4.2. The fabricated parts were 4 mm in diameter and 6 mm tall, printed at a greyscale level 90/70%, and layer thickness of 150 μm , using the manufacturing methodology as described in Chapter 2, Section 2.1.1.1. The 90/70% binder greyscale distribution as described in 3 was chosen due to superior mechanical properties. Ten samples of each category were fabricated. The green parts were then air-annealed in a high-temperature furnace (Lindberg/Blue M, ThermoScientific) with an established heat treatment

protocol [93]. The ambient humidity was controlled to 50%. The heating rate was $10\text{ }^{\circ}\text{C}/\text{min}$ from room temperature to $400\text{ }^{\circ}\text{C}$, a dwell for 2 h , then $10\text{ }^{\circ}\text{C}/\text{min}$ up to $500\text{ }^{\circ}\text{C}$, followed by $5\text{ }^{\circ}\text{C}/\text{min}$ up to $630\text{ }^{\circ}\text{C}$, dwell for 1 h , ending with another heating cycle of $10\text{ }^{\circ}\text{C}/\text{min}$ up to $950\text{ }^{\circ}\text{C}$ with a dwell time of 1 h . Cooling was not controlled.

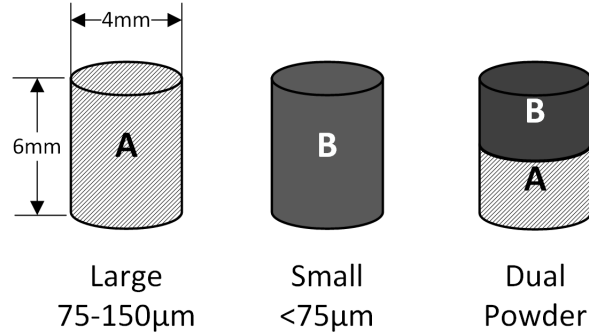


Figure 4.2: An illustration of samples manufactured with large, small, and dual powder sizes, ($n = 10$) respectively

4.1.5 Dimensional Shrinkage Characterization

The parts were characterized dimensionally by measuring the diameter d , and height h , using a digital calliper (Absolute-Digimatic, Mitutoyo Corp., Japan) before and after thermal annealing. Chapter 3, Section 3.1.4 defines the formula used to describe shrinkage in this work.

4.1.6 Porosity Characterization

The bulk density and porosity of samples was calculated based on the Archimedes principle as described in detail in Chapter 3, Section 3.1.5.

4.1.7 Structural Characterization

The microstructure of the cylindrical CPP samples with different powder size composition was observed after thermal annealing using secondary electron emission scanning electron microscopy (SEM, JSM-6460, Jeol, Akishima, Tokyo) at 20 kV accelerating voltage. The samples were sputter-coated with a 10 nm thick gold layer (Desk II, Denton Vacuum, LCC, Moorestown, NJ, USA) to make them electrically conductive.

4.1.8 Uniaxial Compression Characterization

A population of $n = 10$ cylindrical parts for each of the three categories of samples with small, large, and dual powder type compositions were subjected to uniaxial compression using a 1-kN load cell, at a loading rate of 0.2 mm/min (Instron 5548 Micro-Testing, MA) to study their behaviour under compressive loading.

4.1.9 Statistical Analysis

Porosity, density, shrinkage and compression strength results are reported as means and standard deviation. A one-way ANOVA single factor analysis of variance was used to evaluate the statistical significance of measurements as described in Chapter 3, Section 3.1.7. The Weibull distribution function, as detailed in Chapter 3, Section 3.1.7, was used to predict the probability of failure of the ceramic parts, as well as to provide a statistical means of evaluating the quality of the measured data set.

4.2 Results

4.2.1 Powder Size Characterization Results

The SEM image analysis revealed the distribution of powder size along the length and width of particles as illustrated in Figure 4.3, for each of the two categories of powder, large (75-150 μm) and small (<75 μm). It is important to note that for the small powder type, there was a bulk of particles below 5 μm in size that were not included in the results due to measurement accuracy concerns; these particles may influence flowability of this powder type category. For the small powder type, in general, most of the particles were below 30 μm in feature size. A visual comparison of the powder particle size and shape for each of the two types of powder can be seen in Figure 4.4. The powders have an overall irregular shape, with an aspect ratio > 1 .

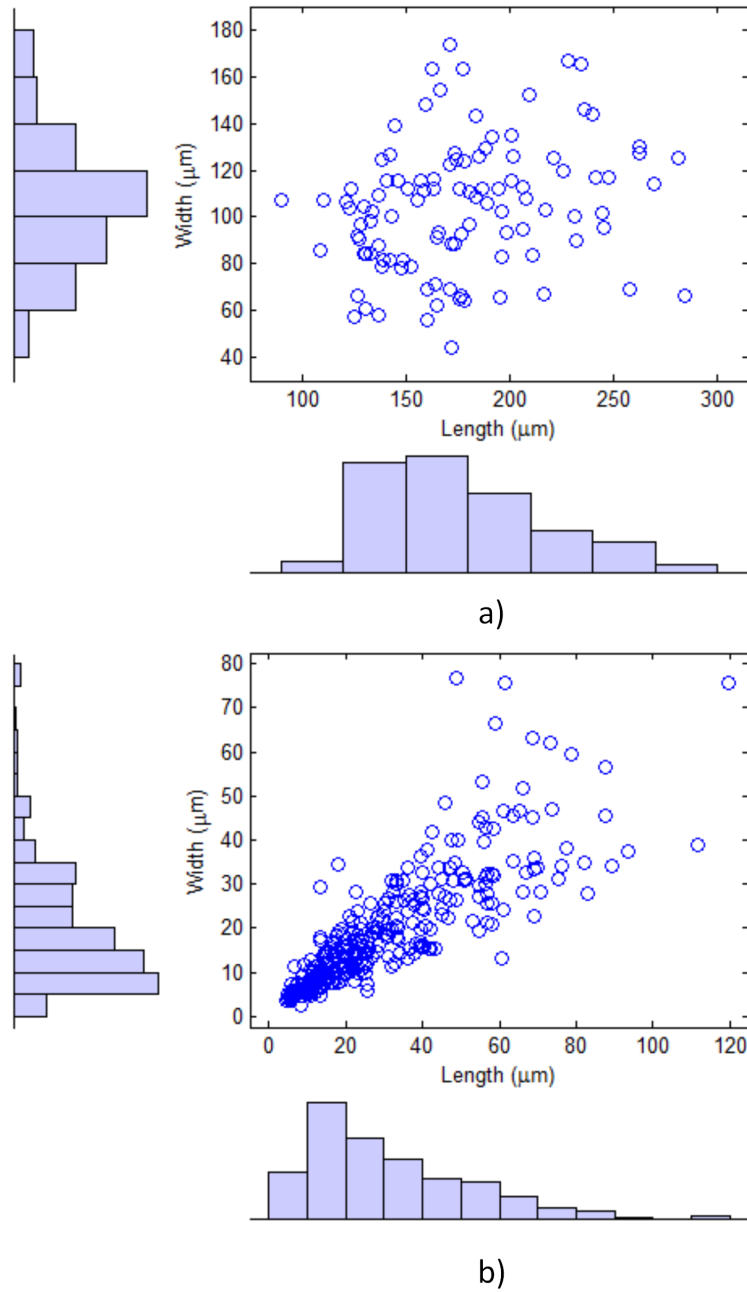


Figure 4.3: The particle size distribution for a) large particle size, sieved between 75-150 μm , ($n = 105$) and b) small particle size, sieved at $<75 \mu\text{m}$, ($n = 300$)

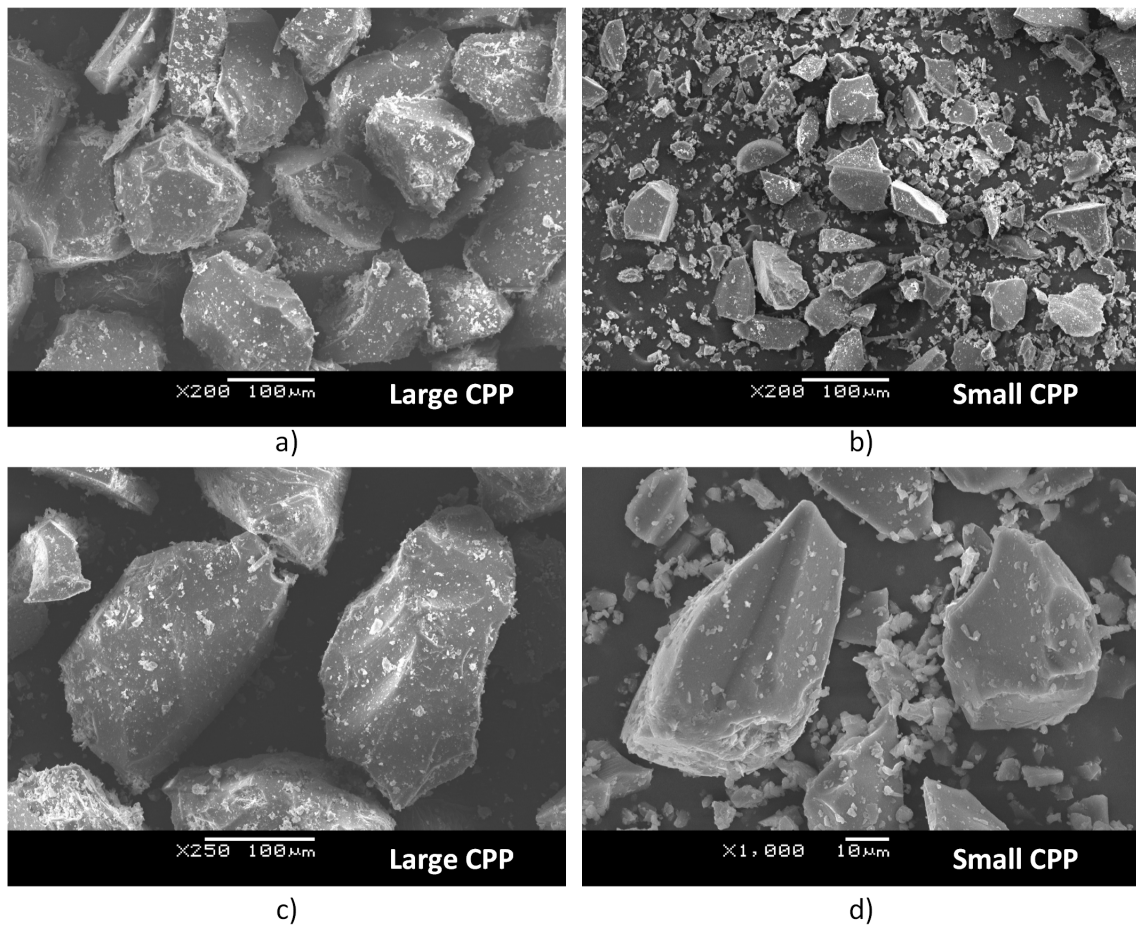


Figure 4.4: SEM view of powder with a),c) large particle size, sieved 75-150 μm at magnification x200, x25; b),d) small particle size, sieved $<75 \mu\text{m}$ at magnification x200, x1000

4.2.2 Structural Characterization Images

Figure 4.5 illustrates the structural characteristics of samples manufactured using large and small CPP particle sizes after thermal annealing. It can be seen from Figure 4.5 that the after sintering, the samples produced using the large powder type retained the outline of the largest particles, displaying a high surface roughness. For the samples produced using the small particle size, individual particles are hard to distinguish, as the particles appeared to fuse together very well during sintering.

4.2.3 Dimensional Shrinkage Results

Table 4.1 illustrates the shrinkage of parts after thermal annealing. The physical shrinkage of each category of parts was determined by comparing the diameter d , and the height h , before and

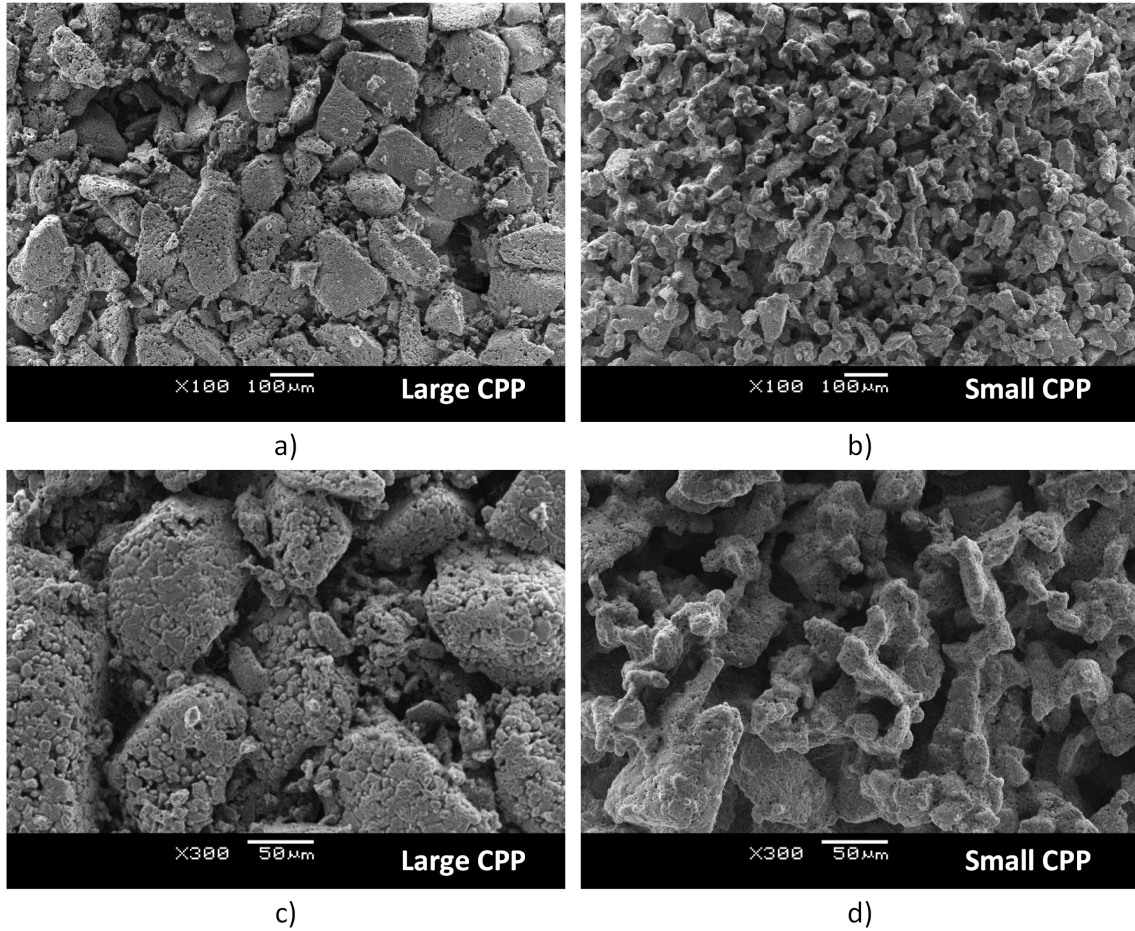


Figure 4.5: SEM view of sintered samples with a), c) large particle size at magnification x100, x300; b),d) small particle size, at magnification x100, x300

after thermal annealing respectively. It can be seen that the shrinkage was significant for samples with small CPP powder composition. For the dual powder samples, the large CPP zone had the least shrinkage of $\sim 2.7\%$ while the small CPP zone had a significant shrinkage of $\sim 20.1\%$.

Table 4.1: Dimensional shrinkage of parts, with small CPP ($<75 \mu m$), with large CPP ($75-150 \mu m$), and dual CPP (measurements of bottom half large and top half small) powder size composition, ($n = 10$).

Composition	$Shrinkage_d(\%)$ ($p < 0.05$)	$Shrinkage_h(\%)$ ($p < 0.05$)
Small CPP	13.7 ± 2.9	18.9 ± 2.6
Large CPP	10.0 ± 1.2	11.5 ± 2.1
Dual CPP (large)	2.7 ± 1.4	10.5 ± 1.7
Dual CPP (small)	20.1 ± 1.6	

4.2.4 Bulk Porosity and Density Results

The bulk porosity and density of thermally annealed samples was calculated using the Archimedes method as described. Table 4.2 illustrates the estimated bulk density for the three categories of samples. The largest bulk density was recorded for samples manufactured using the large CPP powder particle size. The samples with small CPP powder particles had the lowest bulk density and the highest measurement variation. Figure 4.6 illustrates the bulk porosity of the samples, in comparison to the measured uniaxial compression strength.

Table 4.2: Bulk density (g/cm^3) of parts, with small CPP ($<75 \mu m$), with large CPP (75-150 μm), and dual CPP (top half small, bottom half large) powder size composition, ($p < 0.05$), ($n = 10$)

Composition	$\rho_{bulk}(g/cm^3)$ ($p < 0.05$)
Small CPP	1.27 ± 0.11
Large CPP	1.46 ± 0.04
Dual CPP	1.32 ± 0.03

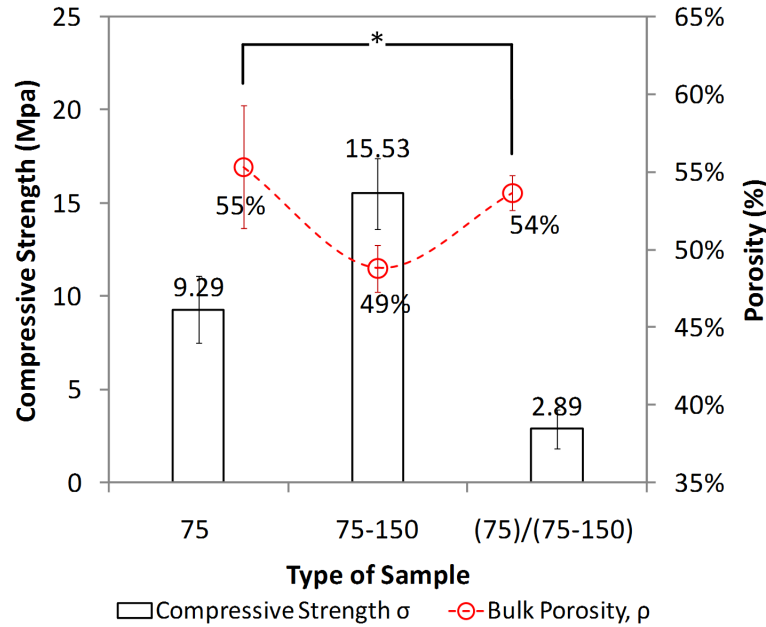


Figure 4.6: Bulk porosity characteristics and compressive strength measurements of cylindrical samples with small, large and dual particle size composition, with ($p < 0.05$). For each trial, ($n = 10$). (*) Illustrates Tukey HSD statistical pairwise similarity

4.2.5 Mechanical Strength - Uniaxial Compression Results

Table 4.3 shows the uniaxial compression test results for samples manufactured using small, large and dual powder composition. These results illustrate that the category with the highest compressive strength corresponds to parts manufactured using large particle size, at 15.5 ± 1.9 MPa. Figure 4.6 illustrates the compressive strength measurements plotted against porosity values, with statistical significance derived from one-way ANOVA. Compressive strength values indicate a good statistical significance ($p < 0.05$), while corresponding porosity measurements show correlations as indicated by the Tukey HSD post-hoc test. Figure 4.7 shows the Weibull linear regression model for compression test measurements for the three categories of samples. In each category, a population of $n = 10$ was used respectively.

Table 4.3: Uniaxial compression results for three classes of parts, small, large, and dual particle size composition, ($n = 10$)

Composition	σ_c (MPa) ($p < 0.05$)	m (R^2)
Small CPP	9.3 ± 1.8	4.8 (0.74)
Large CPP	15.5 ± 1.9	7.5 (0.68)
Dual CPP	2.9 ± 1.1	5.7 (0.98)

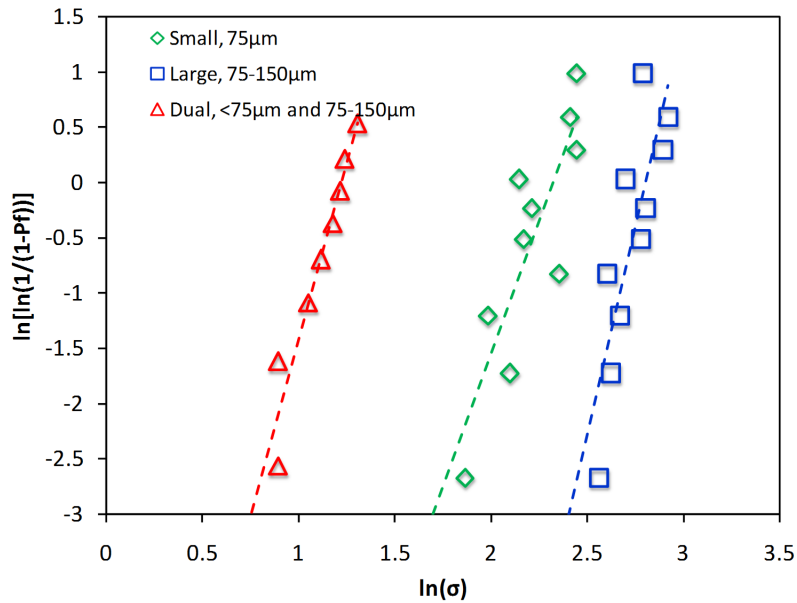


Figure 4.7: Weibull failure probability functions and linear interpolations for compressive strength of cylindrical samples printed with small, large and dual sample particle size composition, ($p < 0.05$), ($n = 10$)

4.3 Discussion

The important achievement of this work is in demonstrating the feasibility of using multiple powders during the multi-scale 3DP manufacturing process, which advances the current state of powder-based additive manufacturing toward new digital manufacturing opportunities. The SEM results shown in Figure 4.4 and Figure 4.5 illustrate visually the significant difference in structural properties between small and large particle compositions before and after thermal annealing respectively. The mechanical compression test results revealed surprising results. The category of samples with the highest compressive strength corresponded to parts manufactured using the large powder size, with a compressive strength of $15.5 \pm 1.9 \text{ MPa}$ as illustrated in Figure 4.6. This result is corroborated by bulk density and bulk porosity measurements illustrated in Figure 4.6 and summarized in Table 4.2, where the sample with the highest bulk density of $1.46 \pm 0.04 \text{ g/cm}^3$ and consequently the lowest porosity of 49% corresponded to the category manufactured with large powder particle size. The lowest performance was seen in dual powder samples, with a compressive strength of $2.9 \pm 1.1 \text{ MPa}$.

The literature suggests that samples with a lower particle size composition manufactured using 3DP approaches would result in parts with a higher mechanical compressive strength [62]. The discrepancy between expected results and the actual results obtained in this chapter can be explained by looking at powder flowability, layer thickness, binder imbibition, and most noteworthy, the thermal annealing protocol as a function of powder particle size. The particle size distribution for the two powder types is shown in Figure 4.3. It can be seen that small powder size category had features mostly below $30 \mu\text{m}$ in length and width, while the length and width of the large powder type were significantly higher, with a peaks between $120\text{-}200 \mu\text{m}$ in feature size. Lu et al. [96] have shown that the binder infiltration rate through particulate porous media is directly proportional to powder particle size for samples composed of $<20 \mu\text{m}$, $20\text{-}45 \mu\text{m}$, $45\text{-}75 \mu\text{m}$, and $75\text{-}150 \mu\text{m}$ TiNiHF powders respectively as used in a 3DP process. They showed that the binder infiltrated faster through $75\text{-}150 \mu\text{m}$ powder particle size. In the present study, for CPP powder size between $75\text{-}150 \mu\text{m}$, the binder may have had enough time to penetrate completely through the layer and thoroughly bind with the previous layer, ensuring good green part strength and resulting in good mechanical performance in compression. Furthermore, small particles tend to have poor flowability [5] and are inclined to agglomerate. This effect causes limited powder compaction during layer spreading [48] and may explain the poor mechanical strength of

the samples manufactured using powder with small particle size in this chapter. The parts with the lowest performance were the dual powder composition samples, with a compression strength of $2.9 \pm 1.1 \text{ MPa}$. This may have been caused by stresses occurring at the interface between the two powder types during thermal annealing, as indicated by the fracture patterns occurring at that location.

Another aspect that influences part strength is the thermal annealing process. In this work, all samples were subjected to the same sintering protocol, optimized for the $75\text{-}150 \mu\text{m}$ powder particle range. Figure 4.8 illustrates examples of thermally annealed CPP samples corresponding to the three categories of manufactured parts. It can be seen that the parts have a significantly different colour, with parts having particle $<75 \mu\text{m}$ in composition appearing grey. This indicates that thermal annealing had a different effect on samples, depending on powder size composition. A more in-depth investigation into an appropriate sintering protocol for samples with different powder size layer composition should be investigated.

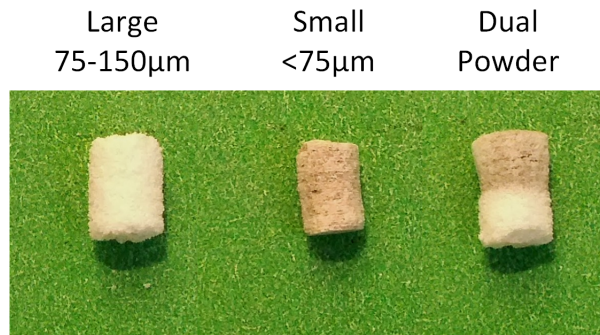


Figure 4.8: Thermally annealed samples with large, small, and dual particle size composition

To increase the performance of powders with small particle size, in terms of lowering porosity and increasing mechanical strength, it is recommended to produce a bimodal homogeneous blend with a low *wt%* ratio of large powder size to small powder size to increase the overall flowability of the material system [62, 99]. Furthermore, it is necessary to tune the linear and rotational velocity of the counter-rotating roller mechanism to achieve the desired compaction of powders during layer spreading for the small powders, as the spread parameters used in this investigations were applicable to powders between $75\text{-}150 \mu\text{m}$ in size. A further approach that could be investigated in an attempt to increase performance in powders with low particle size would be to increase the binder saturation level and/or increase the binder soaking time before spreading a new layer, to ensure good inter-layer adhesion.

Overall, the measured compressive strength values for samples manufactured with different powder size composition at a layer thickness of $150\ \mu\text{m}$ ranged between 2.9 ± 1.1 and $15.5 \pm 1.9\ \text{MPa}$ and were roughly in the domain for cancellous bone ($4\text{-}12\ \text{MPa}$) [69], but not suitable for cortical bone ($130\text{-}180\ \text{MPa}$)[69] substitutes. The CPP parts manufactured using the new multi-scale 3DP system presented in this chapter were also below the compressive strength values obtained for CPP parts using the ZPrinter 310 Plus (ZCorp) machine obtained in previous experiments at $150\ \mu\text{m}$ layer thickness ($34\text{-}50\ \text{MPa}$) [48]. This discrepancy can be attributed to tuning requirements for the counter-rotating roller, which are the focus of a future study. It is important to note that the compressive strength of the CPP parts with $75\text{-}150\ \mu\text{m}$ particle composition manufactured as described in this chapter at a layer thickness of $150\ \mu\text{m}$ using the newly developed system have a compressive strength of $15.5 \pm 1.9\ \text{MPa}$, which is similar to the compressive strength of the CPP part manufactured using the ZCorp 310 Plus (ZCorp) at $175\ \mu\text{m}$ layer thickness, which resulted in a compressive strength of $13.5 \pm 1.9\ \text{MPa}$ as seen in Chapter 5, Section 5.2. These results are very close, the only difference being the layer thickness. This further suggests that fine-tuning of the powder spreading process for the newly developed system is required to produce parts with an increased mechanical strength.

The porosity measurements obtained in this work ($49\text{-}55\%$) were in the desired range for cancellous bone ($50\text{-}90\%$)[81], but outside of the scope for cortical bone ($3\text{-}12\%$)[81]. The results were also higher than the results obtained using the ZCorp 310 Plus equipment in previous studies ($35\text{-}38\%$)[48]. This further indicates that tuning of powder spread parameters is necessary to adjust the compaction of powder based on the type of powder being used in the process. The bulk density results obtained in this chapter ($1.3\text{-}1.5\ \text{g/cm}^3$) were in the range required for cancellous ($0.30\ \text{g/cm}^3$) and cortical bone ($1.85\ \text{g/cm}^3$)[81]. The Weibul moduli obtained in these experiments ($5\text{-}8$) are comparable with reported Weibull moduli for calcium phosphate samples in literature, ($3\text{-}9$)[97] and ($5\text{-}10$)[48], indicating good reliability in measurements presented in this work. These results suggest that the newly developed powder-based additive manufacturing technique is a promising approach in fabricating bone substitutes.

4.4 Summary

A new multi-scale 3DP system was developed to control functionally graded properties of porous structures. In this chapter, the capability of using multiple powder sizes during fabrication was

investigated. Manufacturing trials indicated that the system was capable of producing parts with small particle size $<75 \mu m$, large particle size in the range of $75-150 \mu m$, and dual composition parts, half consisting of layers with small particle size and half with layers consisting of large particle size. Experimental results indicate that the particle size composition had a significant effect on the structural and mechanical properties of parts, however further tuning is necessary in order to establish the correct powder spread parameters and thermal annealing steps for each type of powder size, enabling the fabrication of parts with a desirable mechanical strength. This work has demonstrated that it is possible to use multiple powder sizes or types during the 3DP process, which is an important advancement towards producing functionally graded constructs.

Chapter 5

Control of Functionally Graded Properties via Print Layer Orientation

In 3DP, due to the nature of the layer-by-layer manufacturing process, the effect of the layer stacking orientation within the part may influence the physical, structural and mechanical properties of the constructs. Shanjani et al. [48] and Zhang et al. [63] studied the effect of orienting parts in the building chamber along the direction of the printing axes respectively and concluded that specific orientations of layers within the manufactured part generate superior mechanical strength. This effect has not been explored in detail, as the two research groups that have investigated these effects have focused only on the orientations along the printing axes x , y , z , without considering intermediate orientations. In this chapter, to better understand the correlation between layer orientation and mechanical properties, standard cylindrical parts with 0, 30, 45, 60, and 90° layer stacking orientations with respect to the xz plane were fabricated and subjected to mechanical characterizations in terms of porosity, bulk density, and compressive strength to determine the effects of layer orientation on these mechanical properties. The stacking layer orientation within the part resulting in the highest strength performance along the preferred loading orientation can be implemented to further optimize the mechanical strength of the construct along the orientation of maximum loading, if this is known during the design stage. The choice of layer stacking orientation is a simple setting in the 3DP process that may result in increased strength performance of resulting components.

5.1 Materials and Methods

5.1.1 Powder Substrate Material

In this study, the powder material used in the 3DP process is calcium polyphosphate (CPP) powder (University of Toronto, Toronto, ON, Canada) with an irregular particle shape and size between 75-150 μm blended with polyvinyl alcohol (PVA) powder (Alfa Aesar, Ward Hill, MA) with particle size $<63 \mu m$. The powder blend preparation process is described in Chapter 2, Section 2.1.1.3.

5.1.2 Liquid Binder Material

The liquid binder was an aqueous solvent (ZbTM58) (Z Corporation, Burlington, MA).

5.1.3 Sample Fabrication

For this study, the powder material system [76, 77, 100], binder composition [48], powder material size and layer thickness range [48, 85] have been established through previous work. The focus of this chapter is on establishing the layer orientation within the part that would result in increased mechanical strength along the path of maximum loading. To achieve this, test samples of 4 mm diameter and 6 mm height were manufactured with different layer orientations at 0, 30, 45, 60, and 90° with respect to the vertical axis in the build compartment as seen in Figure 5.1. A 3DP machine (ZPrint 310 Plus, 3D Systems, Burlington, MA) was used to manufacture the parts in a layer-by-layer fashion. The layer thickness was selected to be 150 μm , at a 38 °C working temperature. The cylindrical test parts were designed in a computer-aided design (CAD) software (SolidWorks Corp., Concord, MA) and imported into the 3D printing software (ZPrintTM) in stereolithography (STL) file format. The cylindrical test parts were then oriented within the build bed, as seen in Figure 5.1, with $n = 10$ parts manufactured for each orientation. The green parts were then air-annealed in a high-temperature furnace (Lindberg/Blue M, ThermoScientific) with a pre-established heat treatment protocol [93]. The ambient humidity was controlled to 50%. The heating rate was 10 °C/min from room temperature to 400 °C, a dwell for 2 h, then 10 °C/min up to 500 °C, followed by 5 °C/min up to 630 °C, dwell for 1 h, ending with another heating cycle of 10 °C/min up to 950 °C with a dwell time of 1 h. Cooling was not controlled.

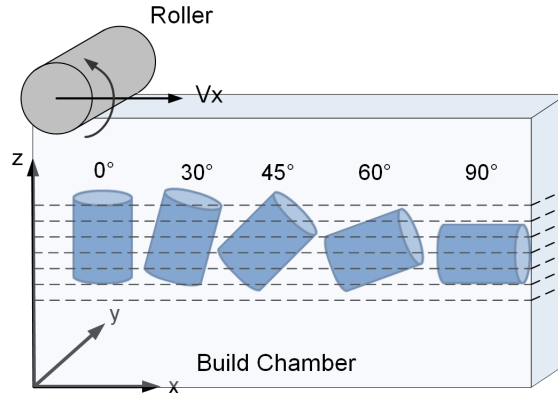


Figure 5.1: Parts printed with 0, 30, 45, 60, 90° layer orientation, arranged in the build compartment. The axes shown correspond to the ZPrintTM software axes

5.1.4 Porosity Characterization

Chapter 3, Section 3.1.5 describes the methodology used to calculate bulk density and porosity.

5.1.5 Structural Characterization

The microstructure of the cylindrical CPP samples with different layer orientations was observed after thermal annealing using secondary electron emission scanning electron microscopy (SEM, JSM-6460, Jeol, Akishima, Tokyo) at 20 kV accelerating voltage. The samples were sputter-coated with a 10 nm thick gold layer (Desk II, Denton Vacuum, LCC, Moorestown, NJ, USA).

5.1.6 Uniaxial Compression Characterization

A population of $n = 8$ cylindrical samples with different layer orientations respectively, of dimension 4 mm diameter and 6 mm height, were subjected to uniaxial compression using a 1-kN load cell, at a loading rate of 0.2 mm/min (Instron 5548 Micro-Testing, MA).

5.1.7 Statistical Analysis

A one-way ANOVA single factor statistical analysis of variance was used as described in Chapter 3, Section 3.1.7. The Weibull distribution described in Chapter 3, Section 3.1.7 was used to predict the probability of failure of the ceramic part as well as to provide a statistical means of evaluating the quality of the measured data set. A population of $n = 10$ was used for density and porosity measurements, and $n = 8$ for compression tests, at different layer stacking orientations.

5.2 Results

5.2.1 Structural Characterization Results

Figure 5.2 illustrates a representative SEM image of a part manufactured at a 60° layer stacking orientation. In Figure 5.2 a), the layer orientations can be distinguished parallel to directions outlined in white. Figures 5.2 b) and c) show examples of sinterneck shapes and sizes under the established thermal annealing protocol. It can be seen that the particles are well fused together, forming a porous mass. The SEM images obtained for the other layer stacking orientations are similar in nature.

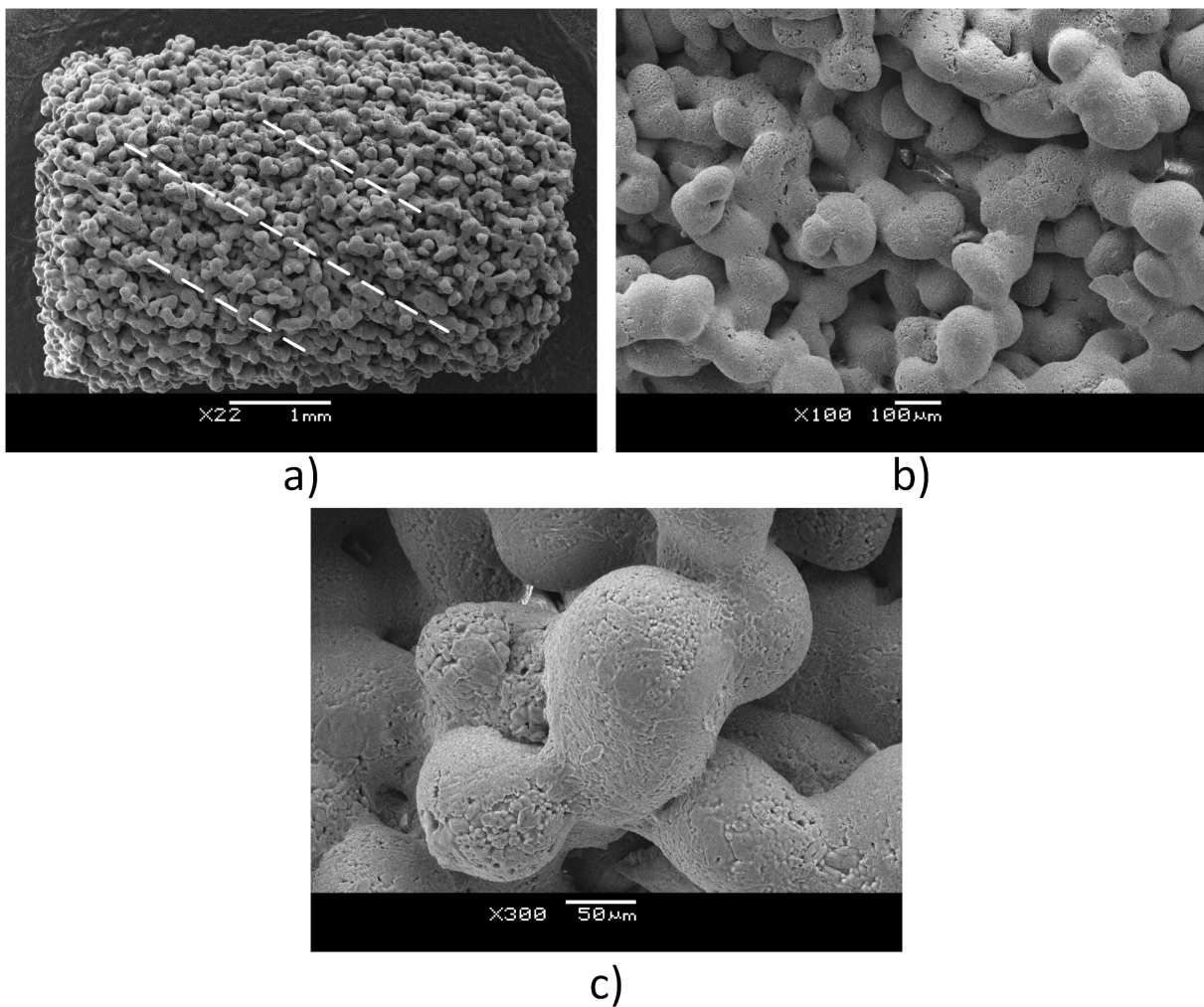


Figure 5.2: Images of a CPP sample with 60° layer stacking orientation as viewed under SEM with a magnification of a) $\times 22$, b) $\times 100$ and c) $\times 300$

5.2.2 Bulk Porosity and Density Results

The bulk density and bulk porosity results for the cylindrical samples with oriented layers at 0, 30, 45, 60, 90° were calculated via ethanol displacement Archimedes principle. The results are summarized in Table 5.1. Figure 5.3 illustrates the bulk porosity measurements with statistical significance and correlations derived from ANOVA Tukey HSD *post hoc* tests. The maximum bulk porosity occurred at an orientation of 0° and 45°, where the porosity value was $38.2 \pm 2.7\%$ and $37.6 \pm 3.1\%$ respectively. The minimum bulk porosity occurred at an orientation of 90°, where the bulk porosity value was $30.0 \pm 2.4\%$.

Table 5.1: Bulk porosity and bulk density characteristics for cylindrical samples printed with layer stacking orientations of 0, 30, 45, 60, and 90° respectively, ($n = 10$)

Layer Orientation	$P_{bulk}(\%)$ ($p < 0.05$)	$\rho_{bulk}(g/cm^3)$ ($p < 0.05$)
0°	38.2 ± 2.7	1.76 ± 0.08
30°	32.2 ± 2.8	1.93 ± 0.08
45°	37.6 ± 2.1	1.78 ± 0.09
60°	34.0 ± 3.2	1.88 ± 0.09
90°	30.0 ± 2.4	2.00 ± 0.07

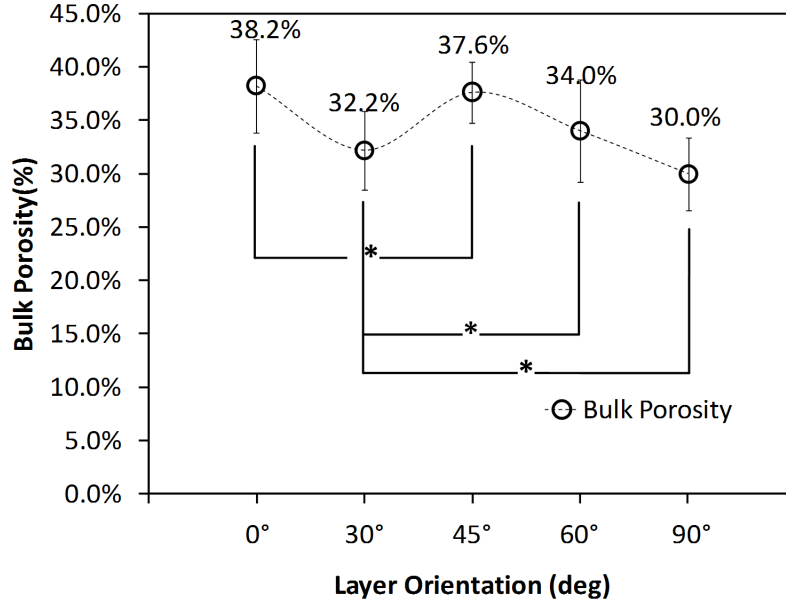


Figure 5.3: Bulk porosity characteristics of cylindrical samples layer stacking orientations 0, 30, 45, 60, and 90° respectively, ($n = 10$). (*) Illustrates Tukey HSD pairwise statistical similarities

5.2.3 Mechanical Strength - Uniaxial Compression Results

The results listed in Table 5.2 indicate that the orientation displaying the maximum compressive strength σ_c is 90° , with $45.13 \pm 6.82 \text{ MPa}$, while the orientations displaying minimum compressive strength are 45° , with $13.43 \pm 4.60 \text{ MPa}$ and 0° , with $13.50 \pm 1.95 \text{ MPa}$.

Table 5.2: Uniaxial compression results and Weibull moduli of cylindrical samples printed with layer stacking orientations of 0, 30, 45, 60, and 90° respectively, ($n = 8$)

Layer Orientation	$\sigma_c(\text{MPa})$ ($p < 0.05$)	$m(R^2)$
0°	13.50 ± 1.95	6.95 (0.91)
30°	20.62 ± 6.23	3.14 (0.93)
45°	13.43 ± 4.60	3.18 (0.80)
60°	28.19 ± 2.46	11.98 (0.95)
90°	45.13 ± 6.82	7.02 (0.90)

Figure 5.4 illustrates the compressive strength measurements with statistical significance derived from ANOVA Tukey HSD *post hoc* tests. Figure 5.5 shows the linear regression computed for the Weibull distribution used to predict the probability of failure of ceramic parts as described previously. In each category, a population of $n = 8$ samples was used.

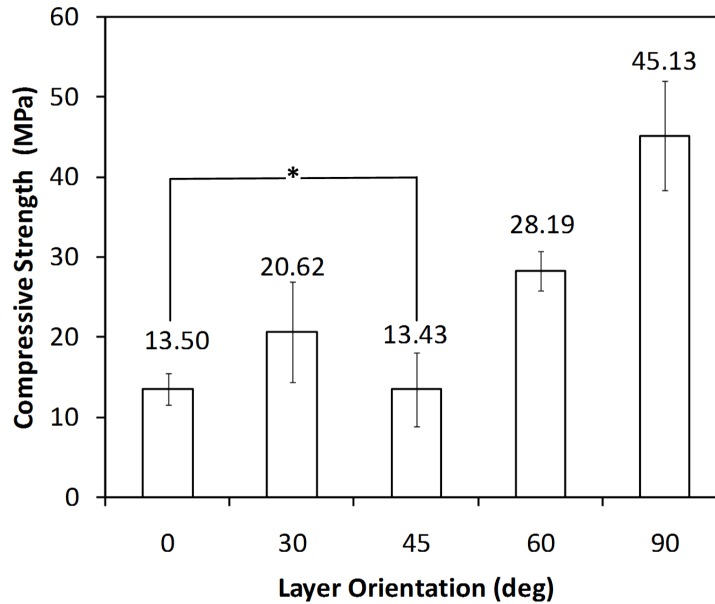


Figure 5.4: Compression strength characteristics of cylindrical samples with layer stacking orientations 0, 30, 45, 60, and 90° respectively, ($p < 0.05$), ($n = 8$). (*) Illustrates Tukey HSD pairwise statistical similarity

5.3 Discussion

This study focused on establishing an orientation that would yield improved mechanical strength characteristics under similar loading conditions, while providing the porosity and bulk density required for bone substitutes. Five categories of test samples, 4 mm in diameter and 6 mm in height, were fabricated, with different layer orientations at 0, 30, 45, 60, and 90° with respect to the vertical axis z in the build compartment as seen in Figure 5.1. Experimental results show that the layer orientation has a statistically significant impact on the measured porosity ($p < 0.05$) and compressive strength ($p < 0.05$) of the samples. The results show that the 45° orientation had the lowest compressive strength, at 13.43 ± 4.60 MPa, while the 90° orientation showed the highest compressive strength, at 45.13 ± 6.82 MPa. This considerable difference in results is supported by the trends in porosity, where the 45° orientation showed one of the highest bulk porosity value at $37.6 \pm 2.1\%$, while the 90° orientation had the lowest porosity at $30.0 \pm 2.4\%$. Generally, a higher porosity would reduce the overall mechanical strength of the part [5].

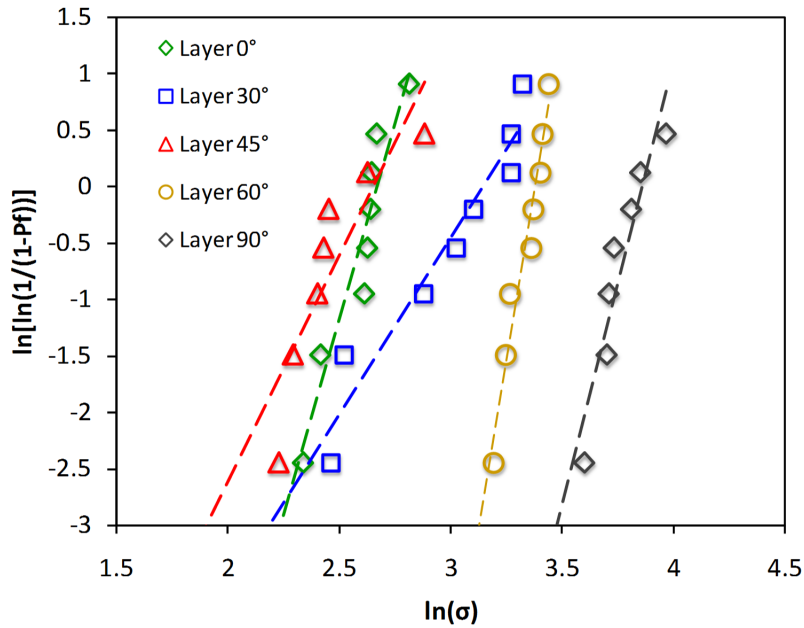


Figure 5.5: Weibull failure probability functions and linear interpolations for compressive strength of cylindrical samples printed with layer stacking orientations 0, 30, 45, 60, and 90° respectively,, ($n = 8$)

The difference in porosity and compressive strength can be attributed to the 3DP process, where the orientation of the irregular-shaped CPP particles within each layer of powder is in-

fluenced by the action of the counter-rotating roller as described by Shanjani et al. [48]. The counter-rotating roller compacts the powder and aligns the irregular-shaped particles having an aspect ratio >1 with the longest axis generally parallel with the build plane. This resulting alignment encourages particles to be in contact at a high radius of curvature between build planes and a small radius of curvature within each build plane. The sinter necks are stronger when the contact angle between particles is smaller, therefore the sinter necks between particles within each build plane (parallel to xy) are expected to be stronger than the sinter necks between build planes (along z axis) [48, 101]. In porous ceramic structures such as CPP, sinter necks represent stress concentration sites; therefore, the stronger the sinter neck, the better the resistance to crack propagation [76]. This means that structurally, the parts fabricated via 3DP are anisotropic in the x , y , and z build directions.

The stress tensor theory for uniaxial compression [102] states that the shear stress and normal stress at an orientation θ can be computed based on Equation 5.1 and Equation 5.2, where the only load acting on the body in uniaxial compression is σ_y , also denoted by $-\sigma$ for compressive loading ($\sigma_x = 0, \tau_{xy} = 0$).

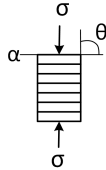
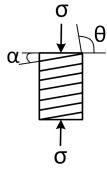
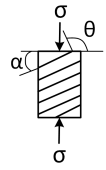
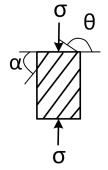
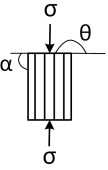
$$\tau_{\theta} = -\frac{(\sigma_x - \sigma_y)}{2} \sin 2\theta + \tau_{xy} \cos 2\theta \quad (5.1)$$

$$\sigma_{\theta} = \frac{(\sigma_x + \sigma_y)}{2} + \frac{(\sigma_x - \sigma_y)}{2} \cos 2\theta + \tau_{xy} \sin 2\theta \quad (5.2)$$

The shear stress and normal stress computed for each print stacking orientation α are summarized in Table 5.3. These theoretical results, along with the structural anisotropy introduced by the 3DP process, explain the experimental behaviour of the oriented parts shown in Figure 5.4 and 5.5, and summarized in Table 5.2. The parts manufactured in the 0 and 45° orientations had the lowest compressive strength, $13.50 \pm 1.95 \text{ MPa}$ and $13.43 \pm 4.60 \text{ MPa}$, respectively. This occurs because the layer orientations within those parts coincide with the direction perpendicular to the principal normal stress for $\alpha = 0^\circ$, and along the direction of the principal shear stress for $\alpha = 45^\circ$, respectively as seen in Table 5.3. The 90° plane, based on the stress tensor theory, does not experience shear or normal stress, therefore the loading is distributed along the parallel stacked build planes, where the interparticle contact results in the strongest sinter neck formation; therefore, these parts show the highest compression strength of $45.13 \pm 6.82 \text{ MPa}$. When comparing the compressive strength of the 30° orientation, $20.60 \pm 6.23 \text{ MPa}$, and 60° orienta-

tion, $28.19 \pm 2.46 \text{ MPa}$, it can be seen that the 30° orientation can sustain a lower compressive strength, as the stacked build planes along the 30° orientation experienced a higher normal stress than compared to the 60° orientation. The experimental results, supported by the stress tensor theory and the structural anisotropy theory, demonstrate that the 3DP process can significantly influence the mechanical strength of parts.

Table 5.3: Normal and shear stress distribution along orientation planes for samples manufactured with stacked layers of orientation $0, 30, 45, 60, 90^\circ$ respectively

					
Print orientation $\alpha(^{\circ})$	0	30	45	60	90
Stress plane angle $\theta(^{\circ})$	90	120	135	150	180
Shear stress on orientation θ	0	$\sigma \frac{\sqrt{3}}{4}$	$\frac{\sigma}{2}$	$\sigma \frac{\sqrt{3}}{4}$	0
Normal stress to orientation θ	$-\sigma$	$-\frac{3\sigma}{4}$	$\frac{\sigma}{2}$	$\frac{\sigma}{4}$	0

The porosity of all samples is between the measured porosity of trabecular bone (50-90%) and cortical bone (3-12%) [81]. In addition, the compressive strength of each category of samples is between the measured ultimate strength of trabecular bone (4-12 *MPa*) and cortical bone (130-180 *MPa*) [69]. From a previous study [48], the pore size for CPP samples appears independent of layer orientation, and ranges between 20-150 μm in size, with a mean of $\sim 56 \mu\text{m}$, which is in an acceptable range for bone substitutes [7, 8, 81]. Furthermore, the values of Weibull modulus m reported for the CPP samples fabricated in this chapter (3-12) are comparable with reported Weibull moduli reported for calcium phosphate samples in literature (3-9)[97] and (5-10)[48] indicating good reliability in measurements presented in this work, as the Weibull modulus is inversely proportional to data scatter. A higher m correlates with a good distribution of porous distribution within the part and good repeatability [98].

5.4 Summary

In this chapter, it has been shown that the layer orientation within the part has a significant influence over the compressive strength of the resulting structure, thus layer orientation is an important optimization parameter in the 3DP design cycle. Furthermore, the results shown in this chapter can be used to further optimize the mechanical strength of the part along the orientation of maximum loading, if this is known during the design stage of the product. The layer orientation within the part is an important design parameter in manufacturing bone substitutes, as the loading kinetics and kinematics on the part can be estimated and layer orientation can be tuned to ensure implant survival under peak loading conditions.

Chapter 6

Additive Manufacturing Design Cycle for Complex-Shaped Structures with Functionally Graded Properties

In this chapter, the additive manufacturing design cycle proposed in Chapter 1, Section 1.3.2 was applied in the context of designing and manufacturing complex-shaped bone substitutes for load bearing applications. It is important to note that the proposed general design cycle can be applied to manufacturing any complex-shaped structure with functionally graded porous properties using additive manufacturing. For designing anatomically complex bone implants, the proposed additive manufacturing cycle was adapted as shown in Figure 6.1. This cycle illustrates an effective approach to ensure that the shape, structural and mechanical properties of the part are met, provided that the materials have been selected appropriately. This chapter focuses on steps 1 through 6 as shown in Figure 6.1 and described below.

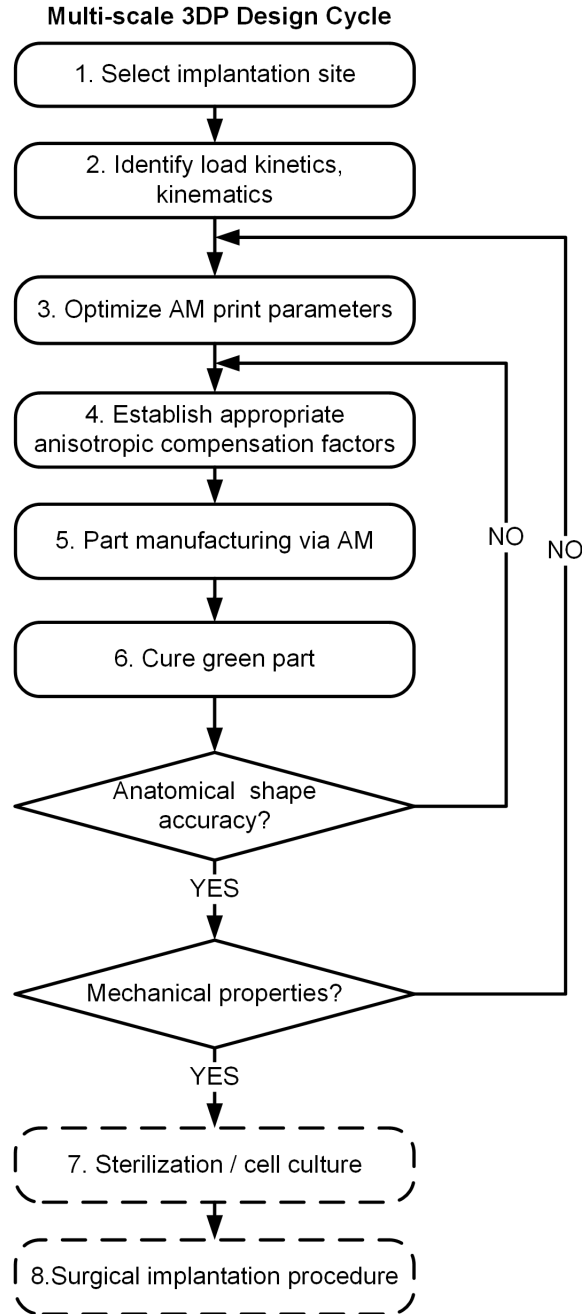


Figure 6.1: Multi-scale 3DP design cycle for bone substitutes with complex internal and external architecture

The first step in the proposed design cycle shown in Figure 6.1 is to establish an implantation site and appropriate implant surgical fixation methods such as location of surgical screws or Kirschner wires, or other bone anchorage 3D design considerations; this step dictates the resulting anatomical shape and the macro and micro-porous properties of the implant based on

the structural characteristics of the natural bone being replaced or enhanced [6, 20]. In the second step, it is important to gain knowledge of the general load kinetics and kinematics at the site in order to estimate the magnitude and direction of contact forces that the implant should withstand safely and repeatedly, by taking into account models and experimental measurements [103, 104, 105]. Based on the implantation site and loading requirements, in the third step, the additive manufacturing print parameters can be tuned to provide the required implant properties. Such parameters may include sacrificial features embedded to control macro-porosities, a gradient of liquid binder levels throughout the part, the category of powder types and sizes that can be embedded within layers independently, as well as the layer stacking orientation within the part. In the fourth step, appropriate anisotropic compensation factors should be considered to compensate for the shrinkage that typically occurs during the manufacturing and curing process [48]. The design cycle is iterative in nature, as seen in Figure 6.1.

The focus of this chapter is to apply the multi-scale 3DP design cycle in fabricating a complex-shaped medial femoral trochlear implant intended for *in vivo* implantation in a sheep model, as a precursor to human trials.

6.1 Case Study

6.1.1 Design Cycle Step 1 - Selection of Implantation Site

Chondral and osteochondral lesions involving the femoral trochlea generally occur either through traumatic impact between the patella and the trochlear groove or develop over time as a result of overload and/or misalignment of the patellofemoral joint, resulting in abnormally high shear forces at the contact surface between the patella and femoral trochlear groove [106]. These lesions are generally common amongst active individuals and athletes [107] and occur at a lower incidence rate amongst the general population [108]. The geometry and complexity of the patellofemoral joint imposes difficulties not only in the diagnosis process, by also in the implementation of remediation strategies. A range of methodologies are available to address trochlear lesions such as microfracture and debridement [106], mosaicplasty [109], autologous chondrocyte implantation (ACI) or matrix-assisted ACI methodologies [73], osteochondral allografts [106, 110], and tibial tubercle osteotomy [111]. For advanced lesions, the patella and trochlear region can be replaced by artificial prosthetics.

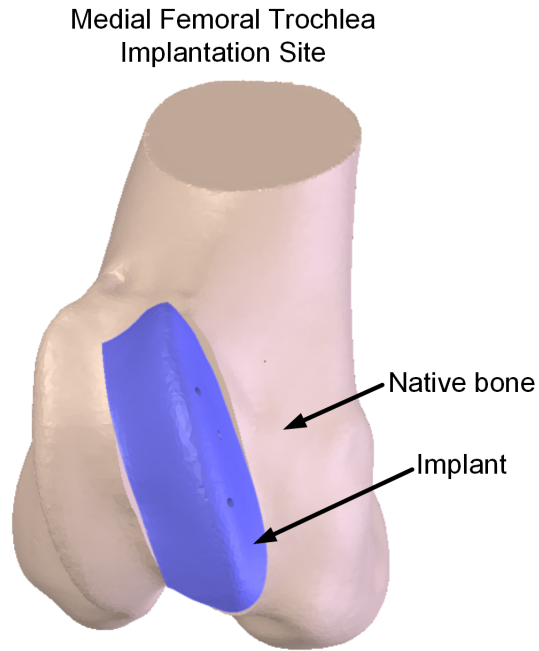


Figure 6.2: Selection of implantation site - medial femoral trochlea in a sheep model

Pilliar et al. [77] have proposed a tissue engineered approach for repairing small osteochondral lesions of the femoral condyle in a sheep model using a biphasic plug implant composed of a cartilage layer and a porous CPP substrate, with positive outcomes. The next step in this study involves the repair of larger defects, such as the medial femoral trochlea, as a precursor to human trials. To this end, a complex-shaped calcium polyphosphate bone substitute has to be manufactured to closely mimic the anatomical and mechanical properties of the bone tissue to be replaced. This chapter focuses on this type of implant in a sheep model, where the selected implantation site and the general shape of the implant are as seen in Figure 6.2.¹

6.1.2 Design Cycle Step 2 - Identification of Load Kinetics and Kinematics

For the medial femoral trochlea bone substitute, it is necessary to have a good knowledge of the magnitude and direction of contact loads at the site of implantation to ensure that the implant can provide dynamic and static mechanical support. The gait loading conditions during the stance phase are not easily measurable *in vivo*, and can be approximated using mathematical models [103, 104]. In a sheep model, loading conditions are inferred through musculoskeletal models and

¹CAD file data for the implant and bone site were kindly provided by Dr. Manuela Kunz, Human Mobility Research Centre, Queen's University

in vivo kinematics measurements [105], where the average peak axial tibio-femoral contact force in the hind right limb of adult sheep was determined to be equivalent to 2.12 *BW* (body weight), with anterior-posterior (A-P) shear forces in average of 0.7 *BW*, and small medial-lateral (M-L) components, below 0.3 *BW* [105]. Based on this knowledge, it was concluded that the axial normal force dominates the gait cycle. ²

6.1.3 Design Cycle Step 3 - Optimization of 3DP Print Parameters

For this study, the powder material system [76, 77], binder composition [48], powder material size and layer thickness [48, 85] have been established through previous work. The optimization parameter chosen for this design cycle step is establishing the layer orientation within the complex-shaped implant that would result in increased mechanical strength along the path of maximum loading. The dominant loading is the axial normal tibio-femoral contact force as discussed previously. Based on the results obtained in Chapter 5 and the inferred loading conditions at the implantation site, the layer stacking orientation for the complex-shaped implant can be deduced as shown in Figure 6.3.

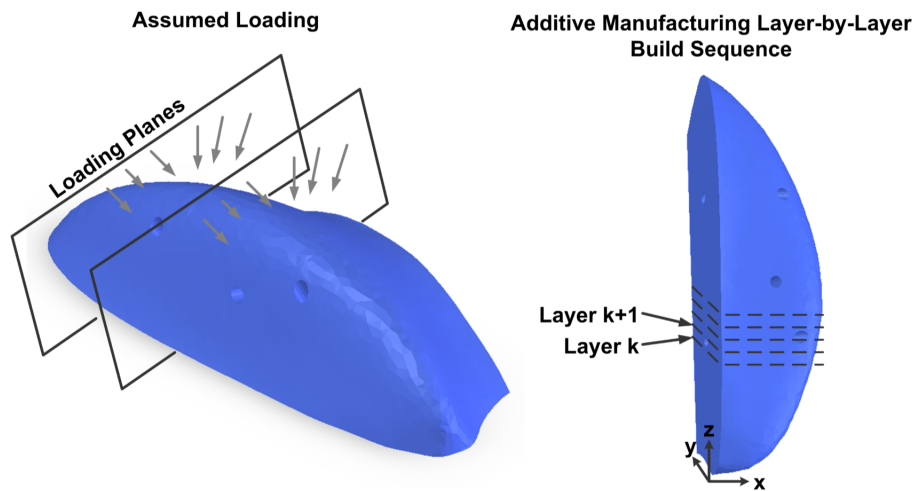


Figure 6.3: Layer stacking orientation for multi-scale 3DP process for the complex-shaped medial femoral trochlear bone substitute in a sheep model

²By comparison, in human models of the force distribution on the tibial plateau during the gait cycle [103, 104], the medial normal force dominates the stance phase with approximately 2.5 *BW*. The medial A-P and medial M-L shear forces were below 0.5 *BW* throughout the gait cycle.

6.1.4 Design Cycle Step 4 - Evaluation of Anisotropic Shrinkage

The 3D shrinkage characteristics of the complex implant are important in estimating scaling factors during the implant design phase to ensure congruity and shape fidelity [30]. To evaluate the shrinkage, it is necessary to measure and compare complex 3D shapes. This can be achieved using various contact and non-contact methods. Contact techniques such as coordinate measuring machine approaches scan the part by tactile probing of the profile, which is slow and may damage the part. Non-contact methods can be used such as employing a charged coupled device camera [112] to determine a point cloud of the implant, using Archimedes principle to establish the volumetric difference post-sintering [113], or using a time-of-flight laser beam based on optical triangulation of emitted and reflected radiation [114]. Another useful approach in digitizing 3D objects is silhouette extraction [115], where a digital camera is used to capture stills of the object in different angles and orientations, while the object is in sharp contrast with the environment. Image filtering and thresholding is used to extract the silhouette of the complex 3D object at each instance. The standard orientation silhouettes can be compared to establish shrinkage between parts.

In this study, a silhouette extraction method was used to establish the shrinkage of a complex-shaped medial femoral trochlea bone substitute. As a first iteration, three implants were fabricated, with isotropic compensation factors of 5, 10, and 15%. The silhouettes of each implant along two orientations, plane xz and yx, were extracted before and after thermal annealing, as seen in Figure 6.4. The silhouettes were processed and compared to an ideal benchmark implant to establish the shrinkage post sintering using an algorithm developed in MATLAB 7.11.0 (MathWorks, Natick, MA, USA). For each orientation, the algorithm sampled the perimeter coordinates at $n = 20$ proportional locations along the z axis to compute the height of the part along the x and y directions and compared the values to determine geometrical deviations. The sampling locations were proportional with the maximum length of each part along the z axis.

6.1.5 Design Cycle Steps 5 and 6 - Additive Manufacturing of Part

A 3DP system (ZPrint 310 Plus, 3D Systems, Burlington, MA) was used to manufacture the parts in a layer-by-layer fashion. A layer thickness $150 \mu m$ was selected, at a $38^\circ C$ working temperature. The parts manufactured were complex-shaped medial femoral trochlea bone substitutes in a sheep model. The design of these implants was based on extracted computed tomography (CT) data

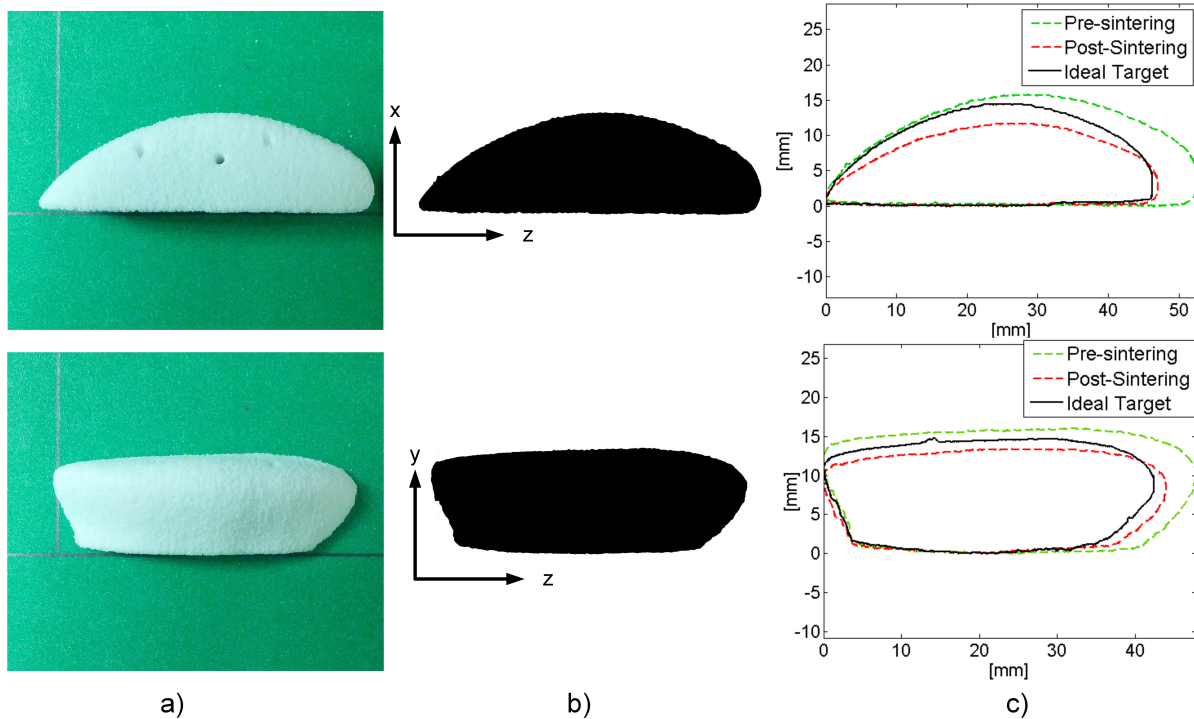


Figure 6.4: The silhouette extraction methodology employs (a) images of the implants in specific orientations to produce (b) thresholded black and white images that can be used to compute the (c) silhouettes of the part. Silhouette contours are then sampled to quantify the shrinkage effects after thermal annealing

(Human Mobility Research Centre, Kingston General Hospital, Kingston, ON) exported in STL file format and imported into the 3D printing software (ZPrint™). It is generally known that parts shrink during the thermal annealing process [48, 85]; therefore, three categories of parts were initially printed in Iteration 1, with +5, +10, and +15% isotropic compensation factors respectively (referred to as FT05, FT10 and FT15) using a print layer orientation as described in Figure 6.3.

In this study, the powder material used in the AM process is calcium polyphosphate (CPP) powder (University of Toronto, Toronto, ON, Canada) with an irregular particle shape and size between 75-150 μm blended with polyvinyl alcohol (PVA) powder (Alfa Aesar, Ward Hill, MA) with particle size $< 63\mu\text{m}$. The powder mix has a composition of 90 wt% CPP and 10 wt% PVA. To ensure a homogeneous powder blend, the powders were mixed for 4 hours using a rotating jar mill (US Stoneware, OH). The PVA powder was used as an additional binding agent to ensure green part strength. The liquid binder was an aqueous solvent (ZB™58, 3D Systems, Rock Hill, SC). The green parts were then air-annealed in a high-temperature furnace (Lindberg/Blue M,

ThermoScientific) with a pre-established heat treatment protocol [93]. The ambient humidity was controlled to 50%. The heating rate was $10\text{ }^{\circ}\text{C}/\text{min}$ from room temperature to $400\text{ }^{\circ}\text{C}$, followed by a dwell for 2 h , then $10\text{ }^{\circ}\text{C}/\text{min}$ up to $500\text{ }^{\circ}\text{C}$, followed by $5\text{ }^{\circ}\text{C}/\text{min}$ up to $630\text{ }^{\circ}\text{C}$, dwell for 1 h , ending with another heating cycle of $10\text{ }^{\circ}\text{C}/\text{min}$ up to $950\text{ }^{\circ}\text{C}$, with a dwell time of 1 h . Cooling was not controlled. Figure 6.5

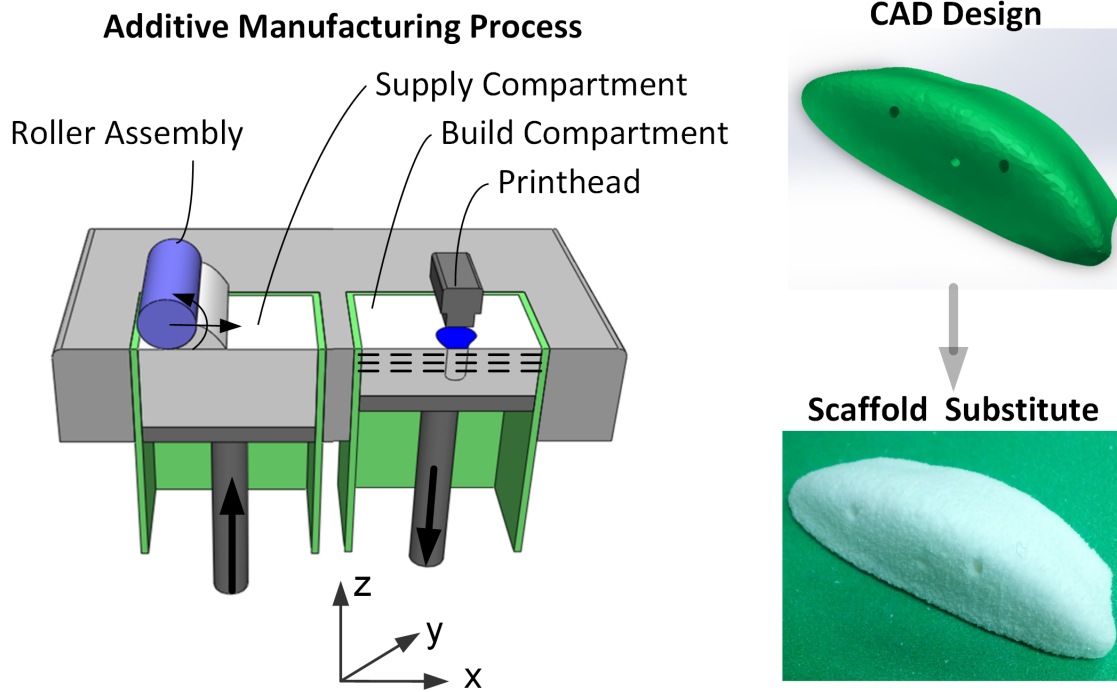


Figure 6.5: Schematic of additive manufacturing fabrication methodology

6.2 Case Study Outcomes

The silhouette of each bone substitute, FT05, FT10 and FT15, was recorded before and after thermal annealing in the xz and yz planes and compared to a benchmark. The femoral trochlea implants with different isotropic compensation factors were analysed to numerically quantify the shrinkage after thermal annealing. Figure 6.6 is an illustration of the comparison between the compensated implants FT05, FT10 and FT15 after sintering, and the benchmark implant shape, along the selected silhouette extraction planes xz and yz respectively. This shows the performance of the compensation factors as the first iteration in the cycle for improving shape fidelity. Qualitatively, it can be seen from Figure 6.6 that further iterations are necessary.

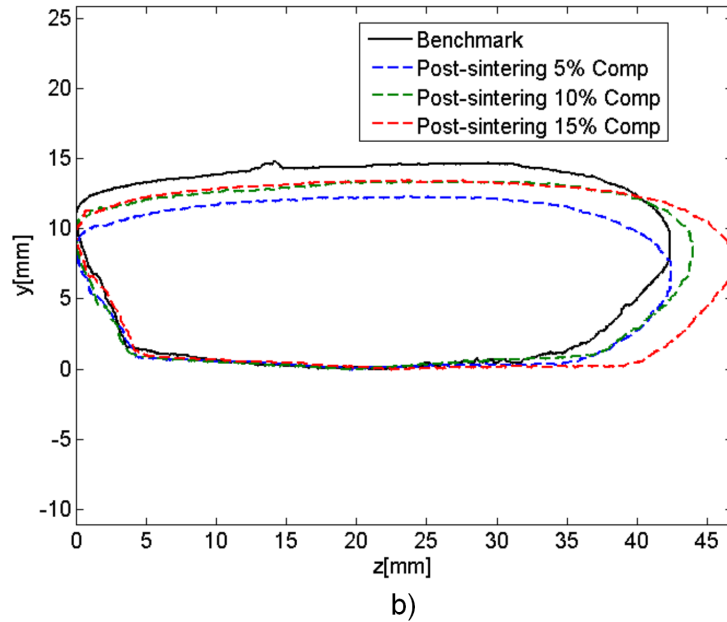
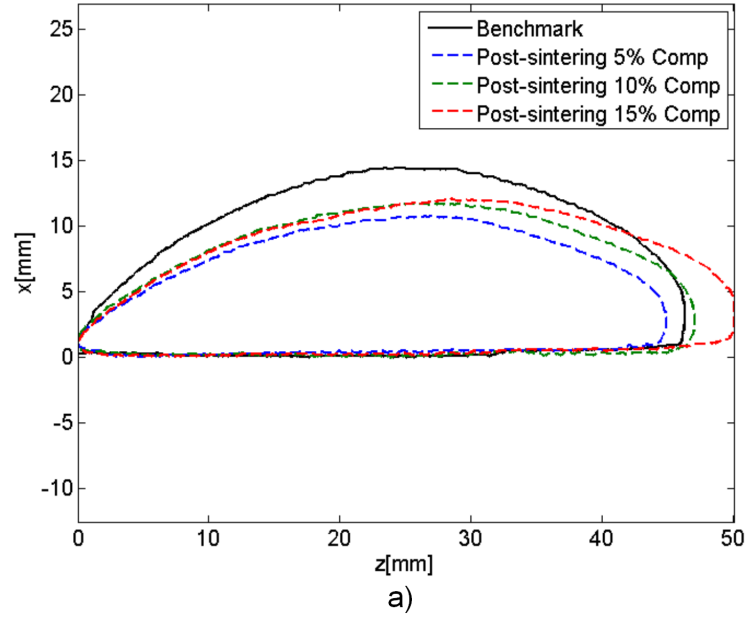
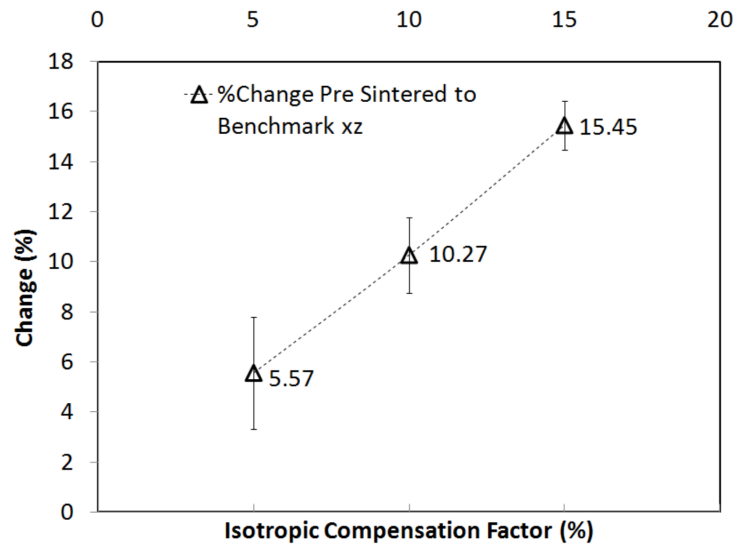
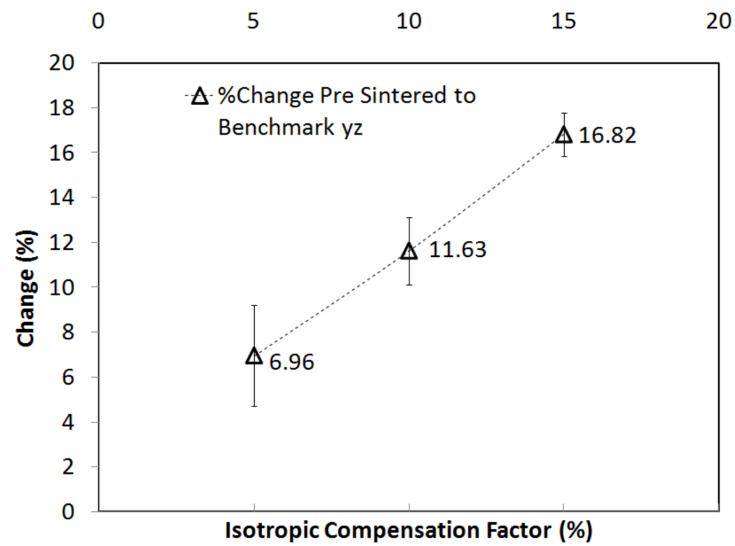


Figure 6.6: Silhouette extraction showing shrinkage after thermal annealing in xz and yz planes for complex shaped medial femoral implant at 5, 10 and 15% isotropic compensation compared to an ideal benchmark

To validate the silhouette extraction algorithm, the silhouette of pre-sintered FT05, FT10, and FT15 compensated parts were compared to the benchmark. As seen in Figure 6.7, the 5, 10, and 15% initial compensation values match closely the computed values within a + 2% tolerance margin, therefore the algorithm is considered to be a reliable tool in quantifying shrinkage.



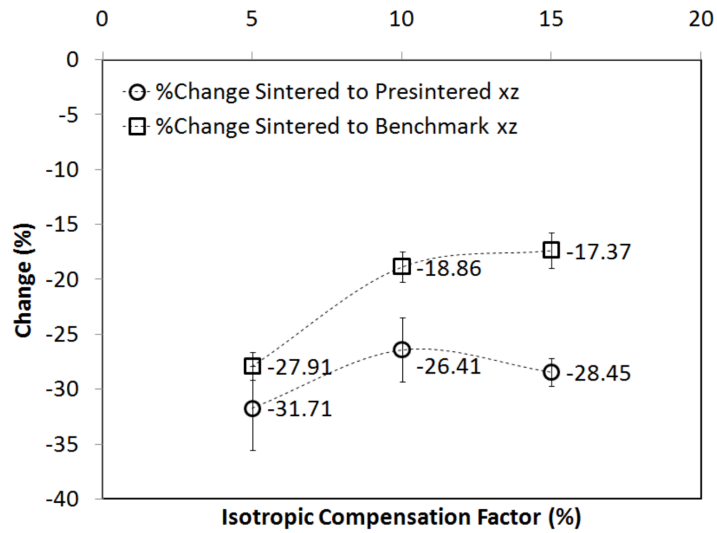
a)



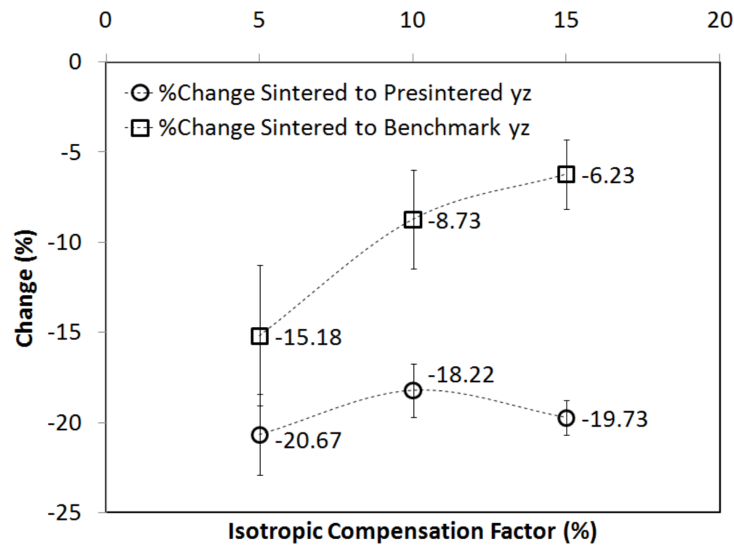
b)

Figure 6.7: Calculated shrinkage in the a) xz plane (x direction shrinkage shown) and b) yz plane (y direction shrinkage shown) for pre-sintered green complex shaped medial femoral trochlea implants at 5, 10, and 15% isotropic compensation compared to an ideal benchmark

Figure 6.8 illustrates the shrinkage results in the xz and yz planes in Iteration 1. It can be seen that in the xz plane, the dimensional change between sintered and pre-sintered implants along the x-axis is non-linear, and varies between -31.71% and -26.41%. In the yz plane, the dimensional change between sintered and pre-sintered implants along the y-axis is also non-linear, and varies between -20.67% and -18.22%.



a)



b)

Figure 6.8: Calculated shrinkage in the a) xz and b) yz planes for complex shaped medial femoral trochlea implant at 5, 10, and 15% isotropic compensation compared to an ideal benchmark

Table 6.1 shows the estimated compensation factors in the x, y and z directions respectively as calculated based on the direct shrinkage and indirect shrinkage values along each axis. The direct shrinkage measurement is computed by comparing sintered vs. pre-sintered parts respectively. The indirect shrinkage measurement is computed by adding the initial isotropic compensation factor to the shrinkage measured between the sintered part and the benchmark. The estimated compensation factor (CF) is calculated as the average of the direct and indirect shrinkage mea-

surements, with a complement sign.

Table 6.1: The estimated compensation factor (CF) along the x- and y- axis respectively. * The direct shrinkage measurement is computed by comparing sintered vs. pre-sintered parts. **The indirect measurement is computed by cumulating the initial isotropic compensation factor to the shrinkage measured between the sintered part and the benchmark. The estimated compensation factor (CF) is calculated as the average of the direct and indirect shrinkage, with a complement sign

Type of Shrinkage	FT05	FT10	FT15	Shrinkage	CF
Mean direct shrinkage x-axis * (%)	-31.7	-26.4	-28.4	-28.8	+30.3
Mean indirect shrinkage x-axis ** (%)	-33.5	-29.1	-32.8	-31.8	
Mean direct shrinkage y-axis * (%)	-20.7	-18.2	-19.7	-19.5	+20.7
Mean indirect shrinkage y-axis ** (%)	-22.1	-20.7	-23.1	-21.8	
Mean direct shrinkage z-axis * (%)	-9.4	-9.3	-12.1	-10.3	+11.0
Mean indirect shrinkage z-axis ** (%)	-10.2	-10.6	-14.6	-11.8	

Figure 6.9 shows the result of applying the anisotropic compensation of 30%, 20% and 10% in the x, y, and z directions respectively, as approximated by the estimated CF as seen in Table 6.1. This is considered as a second iteration in estimating compensation parameters. The resulting part is much closer in dimension to the ideal benchmark part, as the computed dimensional deviation between the benchmark and the sintered part was $-5.65 \pm 1.21\%$ in the x-direction, $+6.97 \pm 2.19\%$ in the y-direction, and $+7.14 \pm 2.79\%$ in the z-direction. The implant resulting from this iteration, as seen in Figure 6.9, has been processed by slowly filing the small overhanging features in the z-direction after sintering. The resulting implant matched very well with the contour of the natural bone at the implantation site and was used in an *in vivo* test in a sheep model. ³

³The surgery was performed at University of Guelph, August 2013

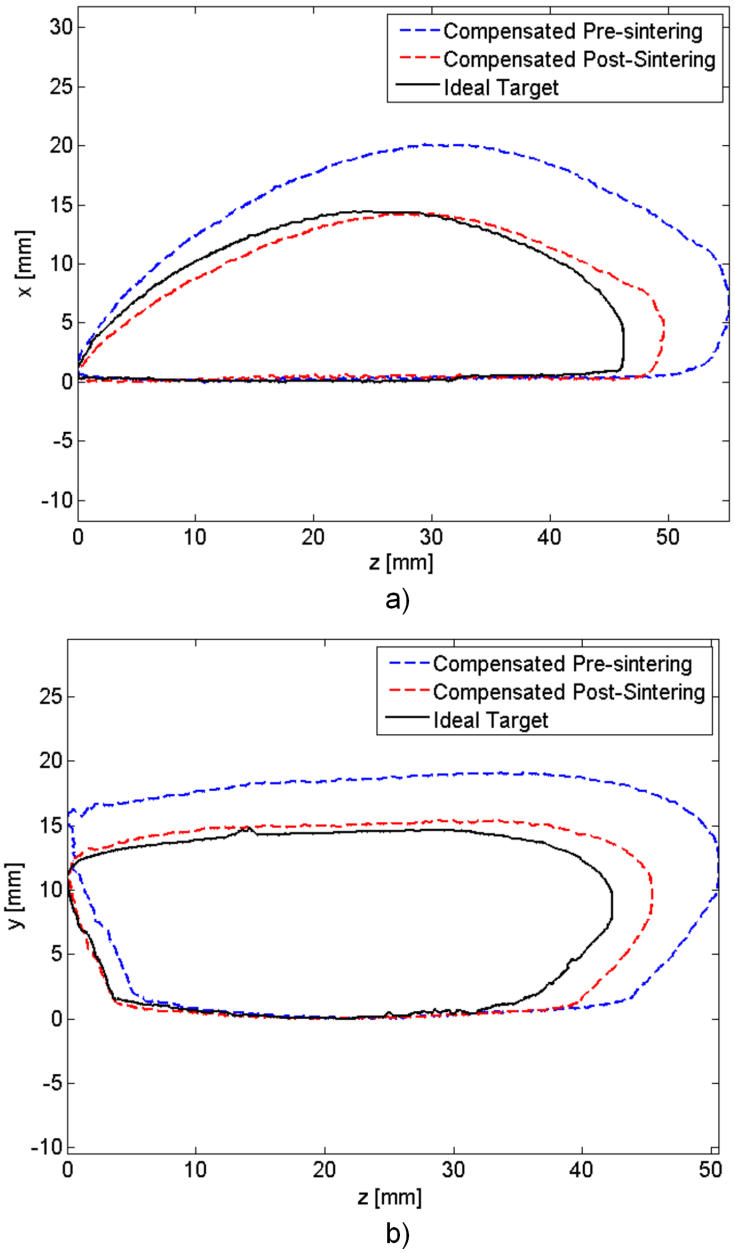


Figure 6.9: Silhouette extraction showing shrinkage in xz and yz planes for complex shaped medial femoral implant at 30, 20, and 10% anisotropic compensation in the x, y, z directions respectively compared to an ideal benchmark

6.3 Discussion

A proposed additive manufacturing design cycle was applied to fabricate a complex-shaped bone substitute for load bearing applications. As a proof of concept, the selected implantation site was the medial femoral condyle in a sheep model, as a precursor for human trials. To this effect, a complex-shaped calcium polyphosphate scaffold substrate was manufactured to mimic the 3D geometrical and mechanical properties of the underlying bone tissue to be replaced. In this study, the optimization step in the additive manufacturing cycle relies on results from Chapter 6, which focused on establishing an orientation that would yield improved mechanical strength characteristics. These results are applied to the complex-shaped implant based on loading conditions at the site of implantation, all the while achieving a good three-dimensional geometrical fidelity to the ideal CAD model.

It was shown in previous work [48, 85] that shrinkage due to thermal annealing of CPP parts manufactured using 3DP is anisotropic in the x, y, and z print directions. Therefore, the AM design cycle includes a step that considers the computation of anisotropic compensation factors for the implant. In this work, a silhouette extraction method was used to compute these manufacturing compensation factors. Based on the results summarized in Table 6.1, the compensation factors in Iteration 1 calculated for the complex-shaped medial femoral condyle bone substitute in the x, y, z directions were approximately 30, 20 and 10% respectively. These values support the idea that shrinkage occurs in an anisotropic fashion. The highest shrinkage occurred in directions parallel to the stacked layers, along x and y axes, since the interparticle contact is at a smaller radius of curvature due to the preferred orientation imposed by the counter-rotating roller mechanism as described previously [48] and explained in Chapter 5. The predominant shrinkage occurred in the x-direction, along the direction of powder spreading. Particles seem more likely to align with the longest axis along the x direction, as the roller spreads and compacts powder particles in its path; therefore, the interparticle contact geometry in this direction promotes a better sinter neck formation during the heat treatment process, resulting in a higher shrinkage of approximately 30%. Conversely, the smallest part shrinkage occurred in the z-direction, 10%, where the sinter necks are weaker due to a higher contact angle between particles.

The applied anisotropic compensation factors resulted in increased overall part fidelity as seen in Figure 6.9. This geometrically compensated part was analysed using silhouette extraction before and after sintering to compute the dimensional deviation from the benchmark and quantify

the performance in the second iteration. The dimensions of the sintered part were found to be $-5.65 \pm 1.21\%$ in the x-direction, $+6.97 \pm 2.19\%$ in the y-direction, and $+7.14 \pm 2.79\%$ in the z-direction. These results further support the idea that shrinkage is non linear and has a complex behaviour, as a closer match was expected. In the additive manufacturing design cycle, the computation of anisotropic compensation factors should be done iteratively, until the complex part dimension matches the benchmark closely, within an acceptable deviation. For this particular part, an acceptable dimensional deviation was considered in the range $\pm 5\%$. In this work, the estimation process can be repeated with the new compensation factors equal to the complement of these newly computed shrinkage values in a third iteration cycle.

6.4 Summary

This chapter focused on applying the additive manufacturing design cycle as described in Figure 6.1 to produce a complex-shaped bone substitute. In this study, the focus of the additive manufacturing design cycle was to enhance the mechanical properties of the implant based on the implantation site and loading conditions, and to ensure the correct anatomical shape of the implant based on silhouette extraction and an image analysis algorithm. The proposed design cycle involves six main iterative steps 1) selecting the implantation site, 2) identifying load kinetics and kinematics at the site, 3) optimizing the 3DP print parameters to yield the desired structural and mechanical properties, 4) establishing appropriate dimensional compensation factors, 5) manufacturing the green part, and 6) annealing the green part. The design cycle was successfully applied for the design and manufacturing of a medial femoral condyle implant in a sheep model and can be expanded for other bone substitute segments. Furthermore, the general design cycle as shown in Chapter 1, Section 1.3.2 can be adapted to produce porous structures with functionally graded properties for other industrial and biomedical applications.

Chapter 7

Conclusions and Future Work

The focus of this thesis was on the development of an additive manufacturing system and associated methodologies for controlling the functionally graded porous structure, composition and 3D shape of constructs. The effects of process parameters on structural and mechanical properties of the manufactured products were investigated. This thesis contributed to the field of additive manufacturing not only by addressing some of the current limitations in powder-based three dimensional printing (3DP), but also by opening the way as a disruptive technology in the advent of the new digital manufacturing trend in rapid layered manufacturing. A newly developed multi-scale 3DP system was designed for this purpose, to control functionally graded internal properties and three dimensional external characteristics of porous constructs manufactured in a layer-by-layer approach. Internal porous properties can be controlled using the multi-scale 3DP system by integrating sacrificial elements with a controlled feature size as described in Chapter 2, by controlling the amount of binder levels dispersed onto the powder substrate as seen in Chapter 3, by controlling the powder type or size as investigated in Chapter 4, or by controlling the layer stacking orientation within the part as seen in Chapter 5. External three-dimensional shape characteristics can be refined by using the proposed algorithm for computing appropriate anisotropic compensation factors using a silhouette extraction approach as described in Chapter 6. This chapter summarizes the main conclusions and some of the future work proposed as a continuation to this thesis.

7.1 Thesis Conclusions

The following conclusions can be drawn from this thesis:

1. The combined 3DP- μ SD approach was used to successfully embed conformal sacrificial photopolymer networks at specific locations within the layers of the manufactured green parts to achieve internal features in the range of 100-500 μm after thermal annealing. It was demonstrated that the sacrificial material does not produce significant pyrolysis residue, which is a criteria of great importance when fabricating implants. Furthermore, a model was proposed and validated experimentally to estimate the geometry of the deposited features, which can be used in designing a real-time deposition control paradigm. The modelling results were on average 14-38% higher than the experimental measurements as a direct consequence of fluid imbibition into porous substrates. The proposed process successfully addressed the minimum feature size limitation in powder-based 3DP.
2. Influence over functionally graded properties was achieved by varying the greyscale binder levels dispersed onto the powder substrate. In this work, by altering the greyscale binder between 70, 80, 90, 100, and 90/70%, within statistical significance, the resulting bulk density varied between 1.46-1.61 g/cm^3 , the porosity ranged between 43-53%, while the compressive strength varied between 4.8-15.5 MPa .
3. The use of two powder sizes, small powder $< 75 \mu m$ and large powder 75-150 μm , influenced structural and mechanical properties of manufactured parts. It was shown, within reasonable statistical significance, that the powder size resulted in a range of bulk density of 1.27-1.46 g/cm^3 , porosity of 49-55%, and compression strength of 2.9-15.5 MPa . Experimental results indicated that the capability of selecting different powder sizes can have an effect over controlling the functionally graded structural and mechanical properties of the manufactured construct.
4. The layer stacking orientations within the part had an effect on the resulting structural and mechanical properties. Experimental data showed that, within reasonable statistical significance, the bulk density varied between 1.8-2.0 g/cm^3 , the bulk porosity ranged between 30-38%, while the compressive strength varied between 13.4-45.1 MPa . In this work, it was shown that control over functionally graded properties can be achieved by selecting the print layer orientation within the part.

5. Thermal annealing produces an anisotropic shrinkage effect on samples manufactured via 3DP. An additive manufacturing design cycle was proposed, which included an algorithm for computing anisotropic shrinkage and appropriate compensation factors along the x, y, z printing directions to ensure that the resulting complex shape retained shape fidelity after thermal annealing when compared to an ideal benchmark. This process was iterative in nature. The algorithm was tested on a medial femoral trochlea bone substitute for a sheep model and can be expanded to other applications. In the first iteration, the compensation factors were determined to be approximately +30, +20, and +10% in the x, y, and z directions respectively. Within the second iteration, the part fidelity was brought to within -6, +6, and + 7% of the final part dimension in the x, y, and z directions respectively. Further iterations were recommended for more stringent shape fidelity requirements.
6. Overall, it was established that the newly developed multi-scale 3DP manufacturing system and process parameters had an influence over the heterogeneous structural and mechanical properties of manufactured parts and could be used to produce constructs with functionally graded porous properties.

7.2 Recommendations and Future Work

The investigations described in this dissertation are intended to establish the framework for further optimization of parameters pertinent to the mechatronic modules integrated in the newly developed multi-scale 3DP system. The intended vision for this system would be to achieve a commercially ready and user-friendly additive manufacturing technology that addresses the emerging need for manufacturing of parts with controlled heterogeneous internal structure and composition, and complex three dimensional shape architecture. To achieve this goal, further research into hardware and software development should be performed.

1. For the micro-syringe deposition system, it is recommended to integrate the model described in Chapter 2, Section 2.2 in a control paradigm that would enable the control of input parameters to obtain the required polymer feature size deposited onto the powder substrate. The model should be refined to include a tuning stage that would account for different sacrificial polymer fluid types by using an estimator approach for this purpose, as described in Appendix E. Furthermore, the control strategy should account for sacrificial polymer fluid

migration through the powder substrate as a result of UV exposure latency, as recommended in Chapter 2, Section 2.2, in order to dynamically compute compensation factors for the estimated height and width of deposited polymer track.

2. In the context of manufacturing bone substitutes using sacrificial elements to produce internal features, to demonstrate that the sacrificial material was fully disintegrated during the thermal annealing process, it is recommended that a cell study be undertaken to establish the effects on cell viability and proliferation. This could be done *in vitro* by culturing the MG-63 cell line (ATCC, CLR-1427, USA) and comparing the cell proliferation and protein expression in samples with and without sacrificial elements, respectively.
3. The unique system capability of printing a wide range of binder droplet sizes onto the powder substrate should be further investigated to determine the range of structural and mechanical properties that can be obtained for different values of powder layer thickness and roller compaction force as dictated by the roller linear and rotational velocity. As well, the effect of gradient greyscale levels should be studied to truly understand the behaviour of the powder-binder interaction.
4. One advantage of the proposed system is the ability to use up to three powder sizes or types during fabrication, which is a new feature in this type of additive manufacturing system. The investigation described in Chapter 4 was preliminary in nature, as the layer thickness and powder spreading parameters were not tuned for each powder type accordingly. It is recommended to determine the effect of different layer spreading parameters such as layer thickness, roller linear and rotational velocity, on the resulting structural and mechanical properties of the resulting part.
5. When working with particles with a small size, an emerging conclusion gained from Chapter 4 was to blend small *wt%* ratios of large particles within the bulk powder of small particle size to improve flowability of the material during the spreading process.
6. Another possible use of the multi-powder capability is to use powders with different *wt%* ratios of a sacrificial porogen components homogeneously blended with the bulk structural powder to further increase the control over porosity in the resulting construct. Feasibility studies have been performed, with promising outcomes.

7. An emerging trend in additive manufacturing software development is to embed the desired structural and mechanical properties (density, porosity etc.) in the data file used in the software for layered manufacturing systems. This is referred to as digital manufacturing. The current state of the art is to simply convey the shape requirements to the additive manufacturing platform. The author is not currently aware of systems with the capability of interpreting digital manufacturing data and relaying the required process parameters to meet the design requirements. The multi-scale 3DP system developed in this work was designed to have the hardware capability to meet such software requirements. For future work, it is necessary to design and integrate a software interpreter that can convey the complex digital design data into layer operational parameters such as selection of powder type/size, binder greyscale distribution across the layer, configuration of sacrificial polymer conformal networks, powder compaction force during spreading, and so on.

APPENDICES

Appendix A

Proposed Additive Manufacturing Process Description

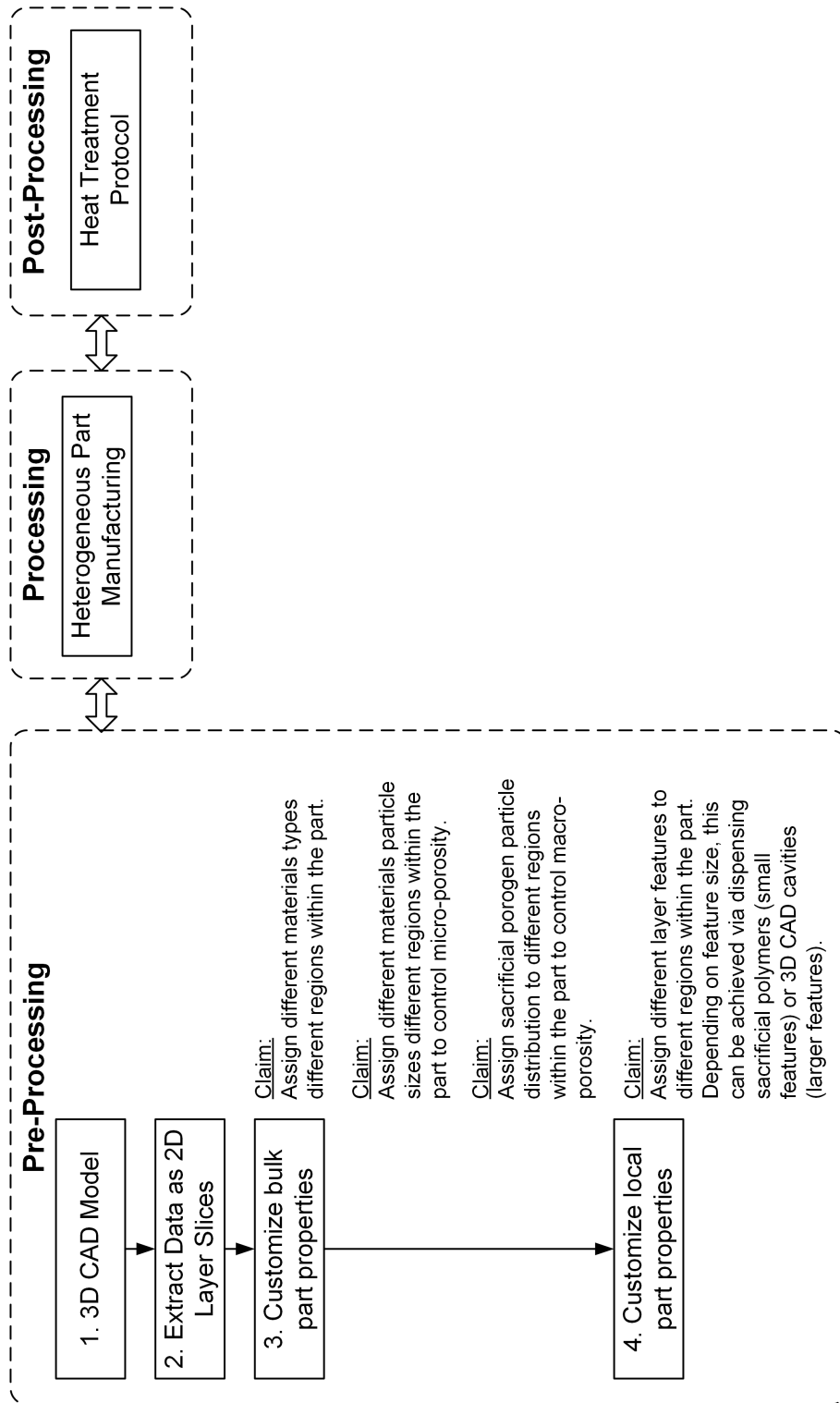


Figure A.1: Pre-processing execution engine high level overview for the novel multi-scale 3DP mechatronic system.

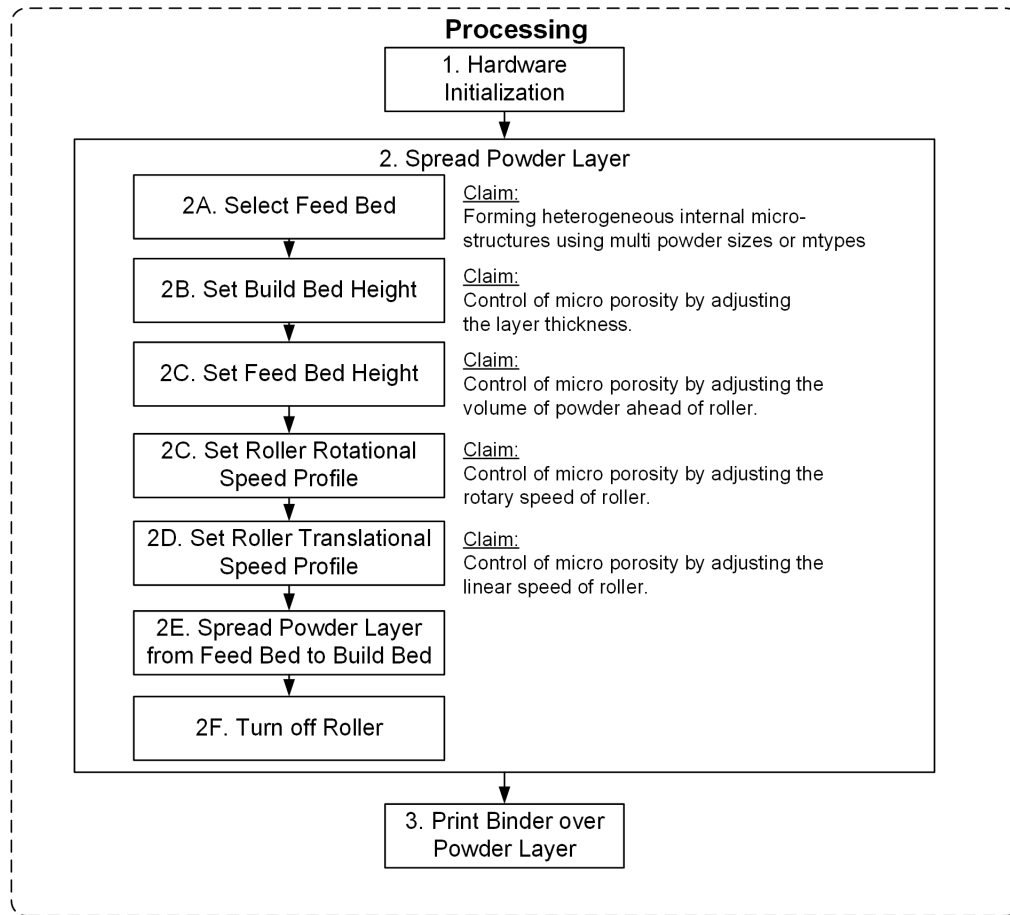


Figure A.2: Processing execution engine high level overview for the novel multi-scale 3DP mechatronic system. Powder spread execution step.

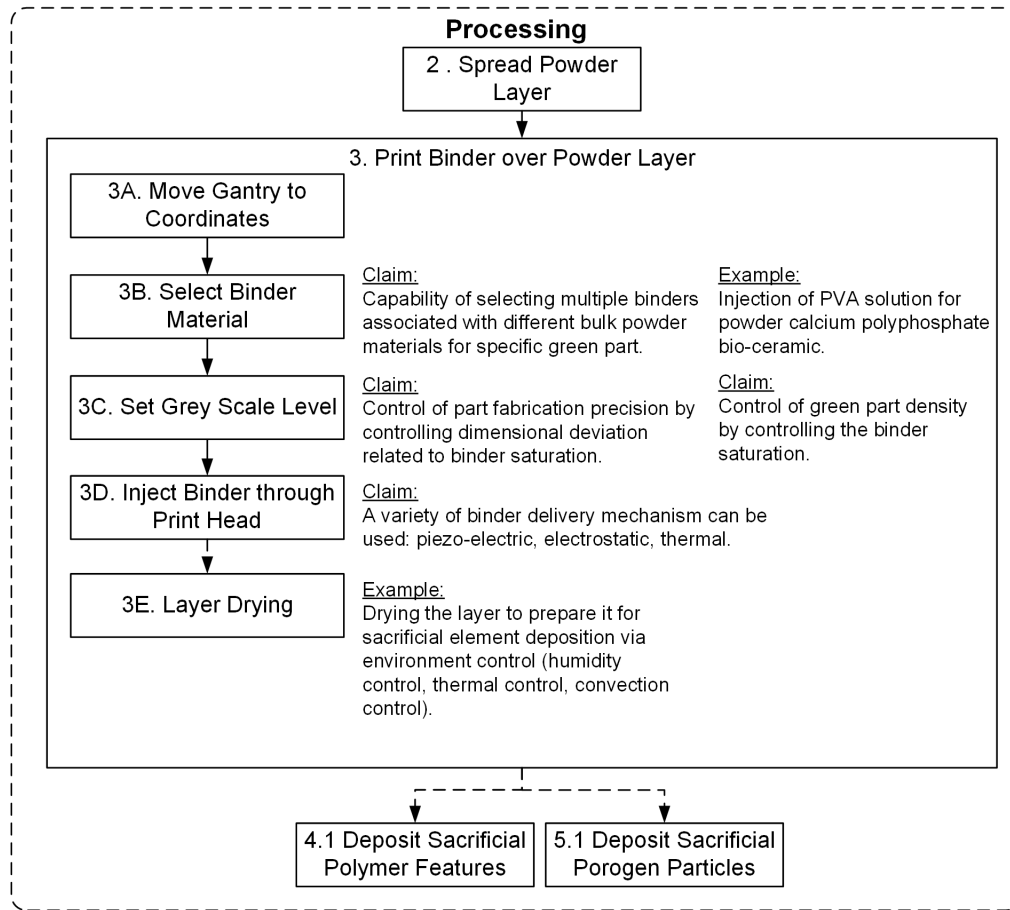


Figure A.3: Processing execution engine high level overview for the novel multi-scale 3DP mechatronic system. Printing of binder execution step.

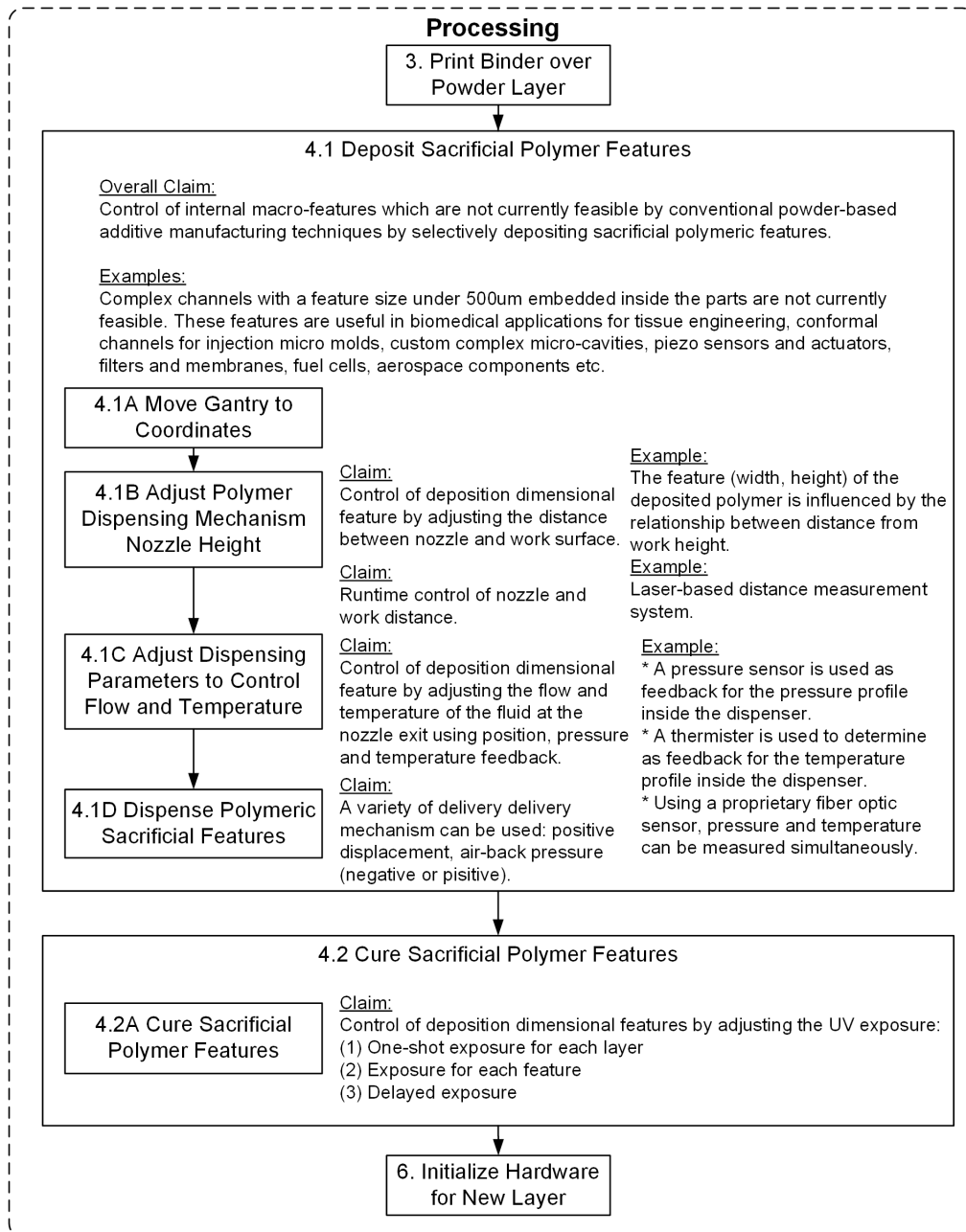


Figure A.4: Processing execution engine high level overview for the novel multi-scale 3DP mechatronic system. Depositing sacrificial polymer features execution step.

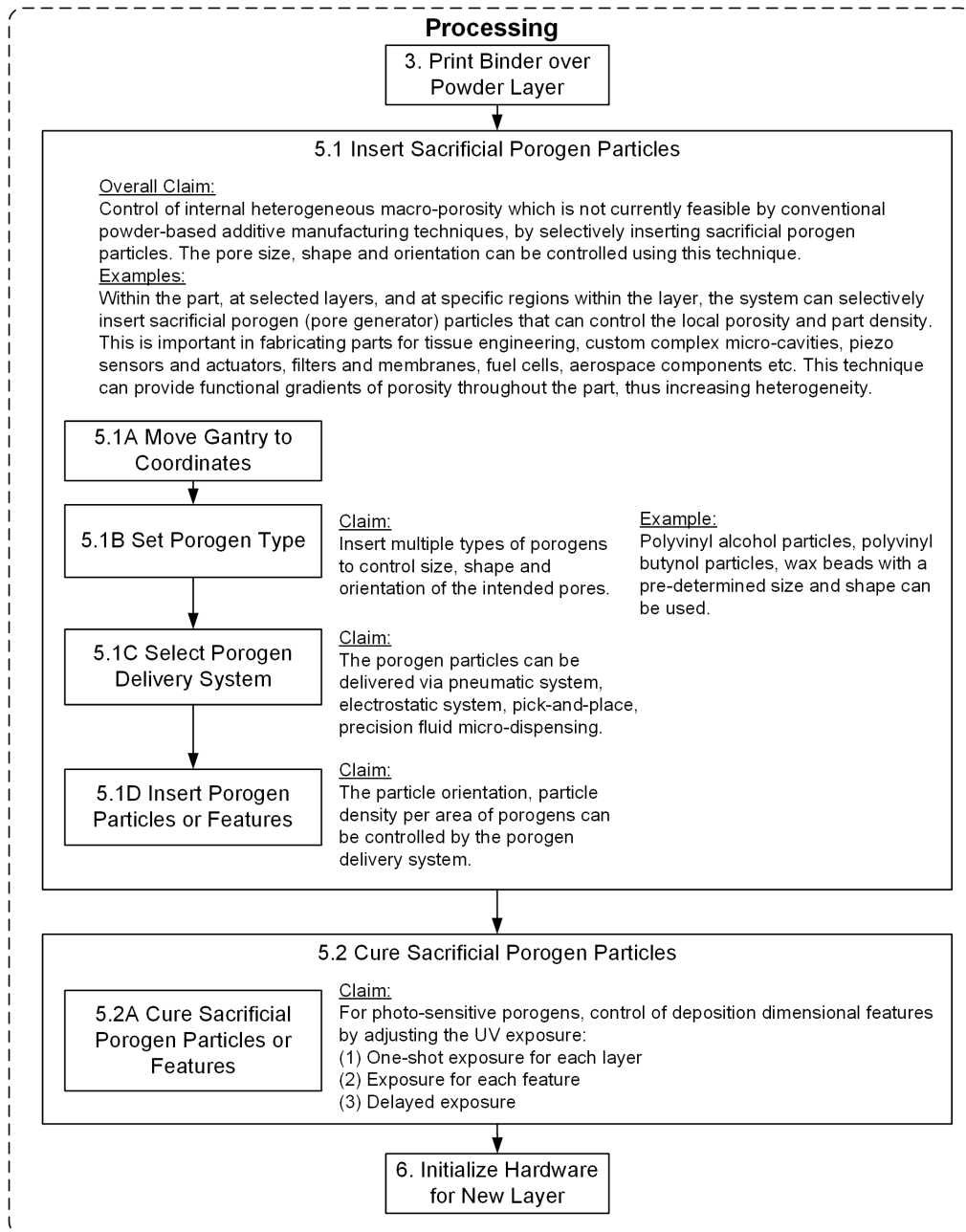


Figure A.5: Processing execution engine high level overview for the novel multi-scale 3DP mechatronic system. Depositing sacrificial porogen particles execution step.

Appendix B

Proposed Additive Manufacturing System Capabilities

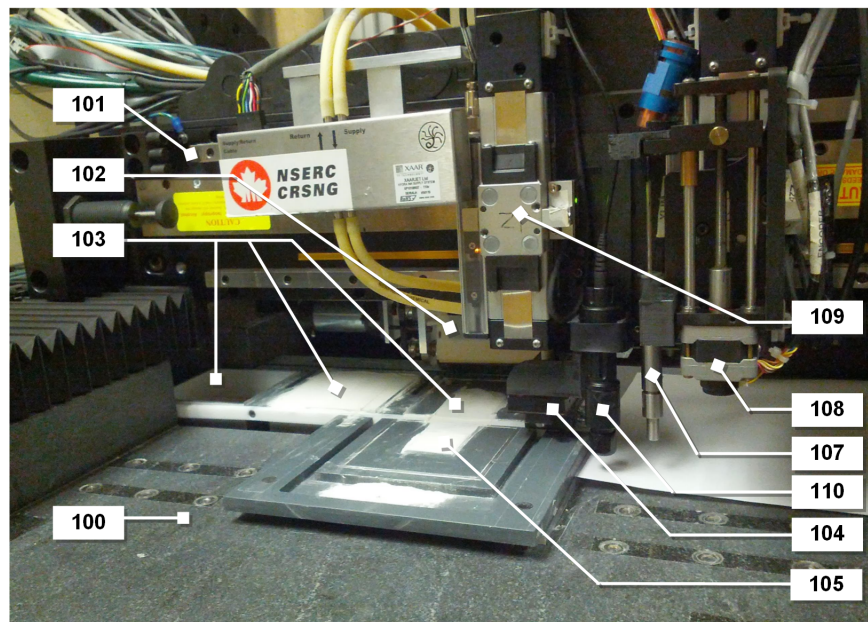
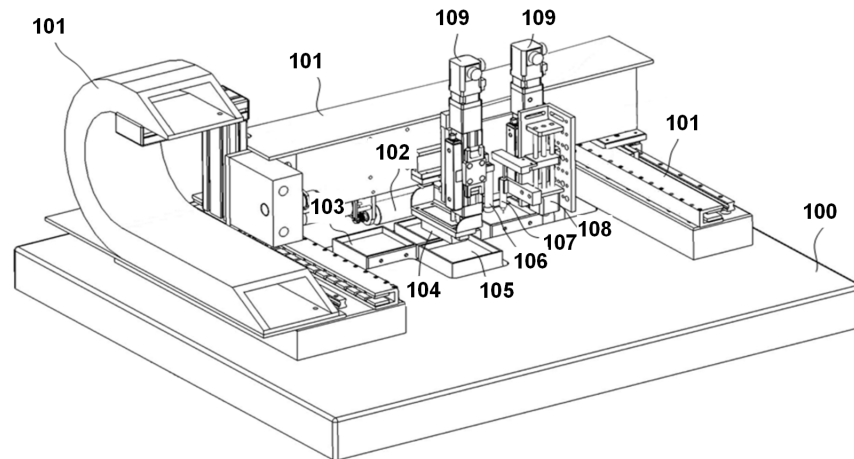


Figure B.1: Novel multi-scale 3DP additive manufacturing system for fabrication of functionally graded porous structures. (100) Granite support, (101) Precision xy gantry assembly, (102) Counter rotating roller module, (103) Multiple supply bed selection and alignment module, (104) Binder dispensing printhead module, (105) Build bed module, (106) Sacrificial porogen particle insertion module, (107) Micro-syringe sacrificial polymer deposition module, (108) Micro-syringe deposition control, (109) Precision control z-axis, (110) UV curing module

Table B.1: Multi-scale 3DP workstation, mechatronics components

Mechatronics Module	Purpose	Actuation or Drive Type	Manufacturer and Part No	Feature	Dynamic Capabilities
XY positioning system	Precision motion in XY plane	Linear positioner, 2 pole servo	PARKER Hannifin T2SA0212NSBBB	◦ Optical linear encoder (RENISHAW RGH24X), 1 μ m resolution	5-10 μ m accuracy and repeatability
Z positioning systems	Precision motion in Z plane(s)	Linear positioner, 8 pole servo	PARKER Hannifin BE161CJ-NPSN	◦ Optical linear encoder (RENISHAW RGH24Z), 0.5 μ m resolution ◦ Rotary optical encoder, 2000ppr resolution	5 μ m accuracy and repeatability
Microsyringe deposition system	Fluid dispensing mechanism	Unipolar stepper	SHINANO KENSHI SST40C1010	◦ Rotary optical encoder (US Digital E4P-100-197-HT), 400ppr resolution	5 μ m accuracy and repeatability
Powder bed carriage	Align one of 3 supply powder beds with the build bed	Single shaft stepper	VELMEX PK296-03AA-A6-3/8	◦ Rotary optical encoder, 500ppr resolution	Good accuracy and repeatability

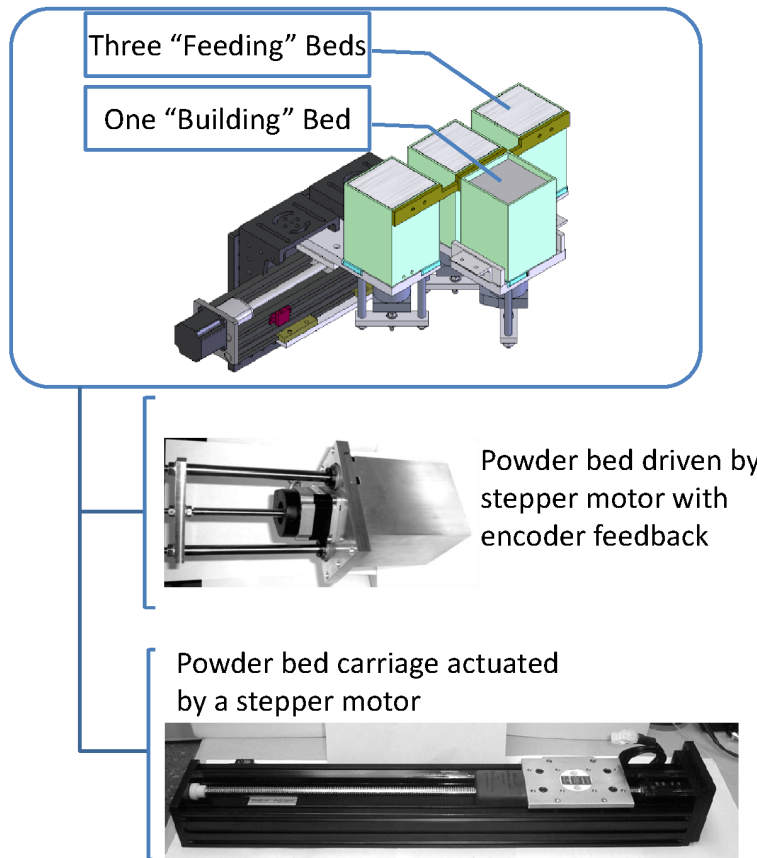


Figure B.2: The relevant hardware components for the feed bed powder systems

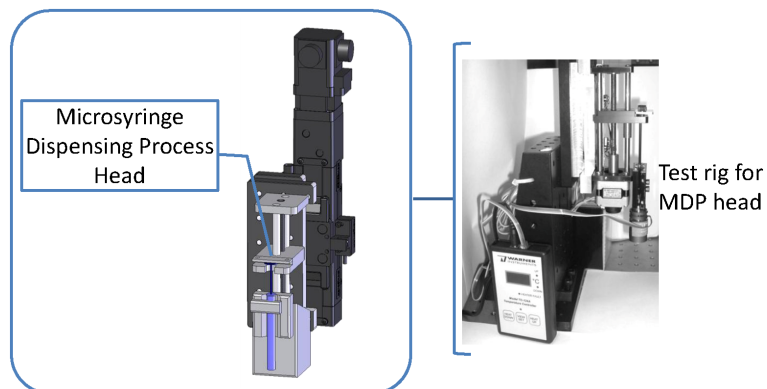


Figure B.3: The relevant hardware components for the micro-syringe deposition module

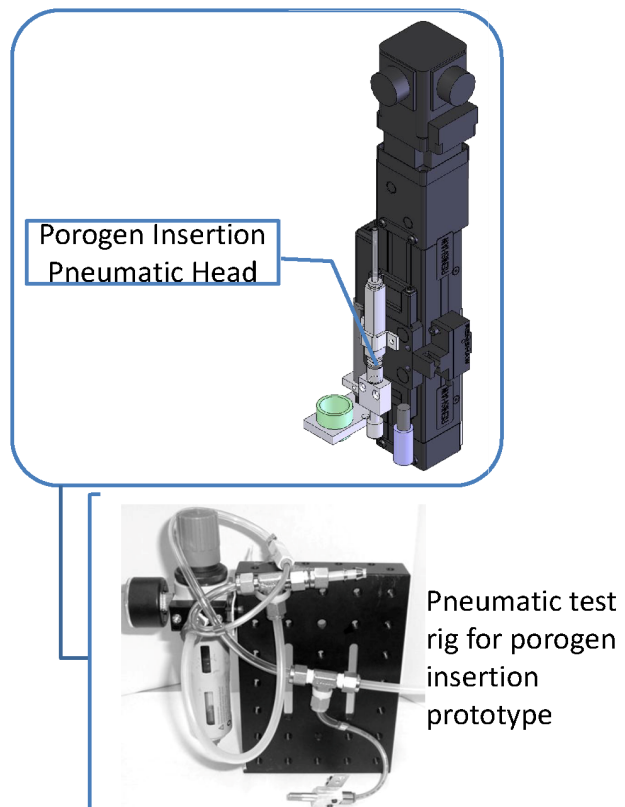


Figure B.4: The relevant hardware components for the porogen insertion module. This system is currently under development

Appendix C

Analytical Modelling of Micro-syringe System

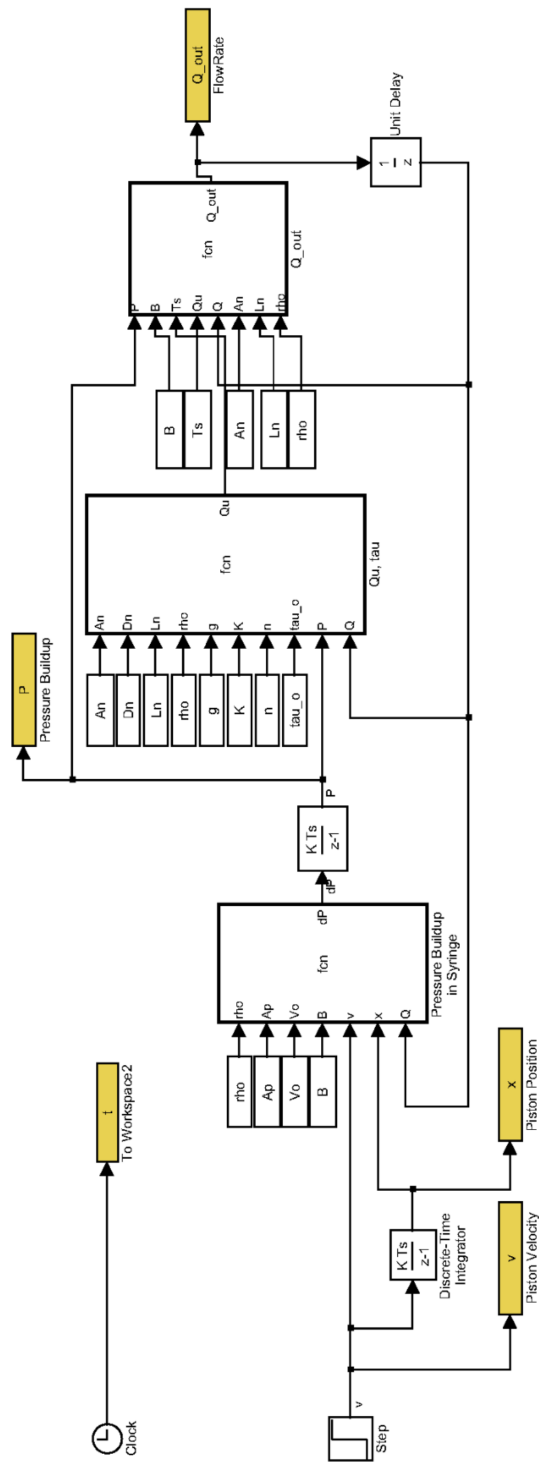


Figure C.1: Analytical pressure-flow model as programmed in Simulink

Model5_Final/Pressure Buildup in Syringe.eML_blk_kernel

```

1: function dP = fcn(rho, Ap, Vo, B,v, x, Q)
2:
3: Q_vol = Q/rho/1000; %Q is in [kg/s], while Q_vol is in [m^3/s]
4: dP = Ap*B*v/(Vo-Ap*x)-Q_vol*B/(Vo-Ap*x); %pressure buildup inside the syringe
5:
6:
7:

```

Model5_Final/Q_out.eML_blk_kernel

```

1: function Q_out= fcn(P, B, Ts, Qu, Q, An, Ln, rho)
2:
3: if (Qu==0)
4:     Qu = 10^-10;
5: end;
6:
7: bb = rho*Ln/An; %this is from chen's model
8: %preliminary calculations of parameters (after model discretizing)
9: Kv = exp(-Ts/(bb*Qu));
10: Pv = 1/bb;
11: %determine flow output
12: Q_out = Kv*Q+Pv*P; %because it is assumed Q[g/s]
13:
14:
15: %%preliminary calculations of parameters
16: %Kv = exp(-Ts/(B*Qu));
17: %Pv = 1/B;
18: %%determine flow output
19: %Q_out = Kv*Q+Pv*P;
20:
21:

```

Model5_Final/Qu, tau.eML_blk_kernel

```

1: function Qu = fcn(An, Dn, Ln, rho, g, K, n, tau_o, P, Q)
2:
3: %determine shear stress
4: u = Q/An;
5: tau = Dn/(4*Ln)*(P+Ln*rho*g-1.12*rho*u^2);
6:
7: %determine steady state flow under a unit of pressure
8: PARAMETER = n/(3*n+1)*tau^2 + 2*n^2/(2*n+1)/(3*n+1)*tau_o*tau+2*n^3/(n+1)/(2*n+1)/(3*n+1)*tau_o^2;
9: Qu = pi*Dn^3/(8*P*K^(1/n)*tau^3)*(tau-tau_o)^((n+1)/n)*PARAMETER;
10:
11: % Qu=35*10^-3/rho;

```

Figure C.2: Formulae descriptions for pressure-flow model as programmed in Simulink

Appendix D

Surface Roughness Experimental Measurements

Surface Roughness Experimental Measurement

The surface roughness was computed by extracting the profile of five ceramic parts manufactured using CPP powder with 75-150 μm particle size before thermal annealing. The images were taken using a calibrated camera (EDMUND Optics Inc., NJ, USA) at 1x magnification with a calibration factor of 2.7397. An example of such an image is shown in Figure D.1.

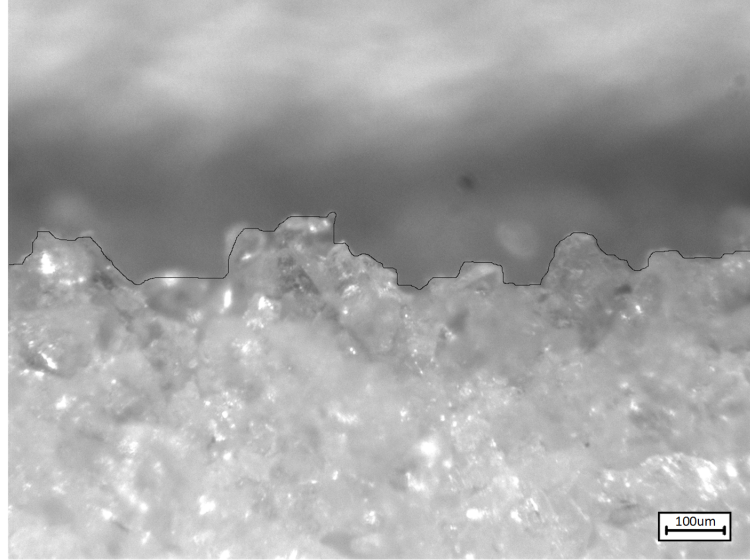


Figure D.1: Profile of CPP ceramic part with particles (75-150) μm in size

Table D.1 illustrates the surface roughness results computed via image processing (MATLAB 7.11, MathWorks, Natick, MA, US).

Table D.1: Surface roughness values for CPP samples with particle size 75-150 μm . R_a is the arithmetic average of absolute values roughness parameter. R_q is the root mean squared roughness parameter.

Profile Image	R_a [μm]	R_q [μm]
1	35.92	41.48
2	37.68	45.17
3	30.53	36.50
4	30.98	36.64
5	27.16	33.16
Mean	32.45	38.59
St Dev	3.83	4.22

Appendix E

Closed Loop Control Strategy for Micro-syringe System

Closed Loop Control Strategy for the Micro-syringe Deposition System

Based on the developed equations for the pressure-flow model, the fluid dispensing mechanism behaves similarly to a second order system. Using this approximation, a simple PI controller may be utilized to enhance the capability of the system. A major difficulty arises in closing the control loop by using flow measurements, as the flow is hard to measure in the μL range. The proposed approach is to use pressure measurements to produce a real time estimate of fluid flow and close the control loop using this estimate.

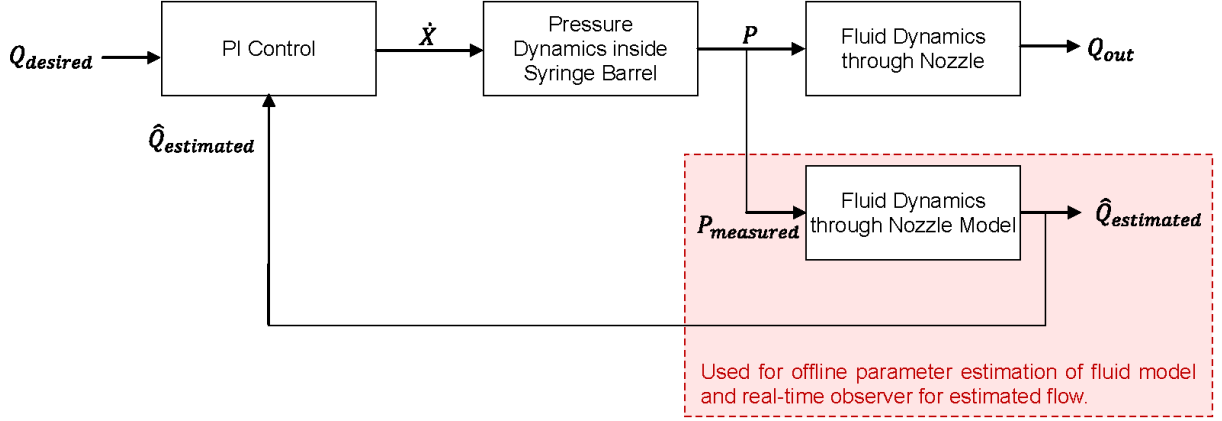


Figure E.1: Control strategy for the pressure flow component of the μSD system

The initial model developed for fluid dynamics through the nozzle has been used to observe the fluid behaviour and infer a controller strategy. In reality, fluid properties are rarely known, and the system must be accurate for various fluid types. To accommodate for this, the proposed control scheme uses a “Fluid Dynamics through Nozzle” model as seen in Figure E.1 for initial off-line identification of fluid parameters using a Modified Least Squares (MLS) algorithm. Once the fluid parameters have been identified, the model is used for on-line estimation of fluid flow based on pressure measurements. This estimation is used as a feedback control signal.

The proposed fluid flow model has been developed using the Power-Law described by Equations (E.1), (E.2) [116]:

$$Q = K_o \Delta P^n \quad (\text{E.1})$$

$$K_o = \frac{n\pi D_n^3}{8(3n+1)} \left(\frac{D_n}{4L_n K} \right)^{\frac{1}{n}} \text{ and } N = \frac{1}{n} \quad (\text{E.2})$$

where $\Delta P = P - P_{atm}$ is the pressure across the nozzle. Parameters are described in Table 2.2. This equation is used for real-time feedback of flow estimations.

The volume of fluid dispensed over a period of time is determined by Equation (E.3)[116]. This equation is used for off-line identification of fluid parameters K_o and N by using data from the pressure sensor as the input to the system and the volume of fluid dispersed based on stepper motor encoder counts as the output from the system.

$$V = \int Q dt \quad (\text{E.3})$$

Since there are only two parameters of interest, a minimum of two independent and sufficiently exciting dataset points are required to perform the parameter identification.

$$V = [V_1 \ V_2]^T \quad (\text{E.4})$$

$$F = [f_1(X) \ f_2(X)]^T \quad (\text{E.5})$$

$$X = [X_1 \ X_2]^T = [K_o \ n]^T \quad (\text{E.6})$$

In Equations (E.4), (E.5) and (E.6) V is the actual dispensed volume measurement matrix, F is the estimated dispensed volume matrix and X is the parameter matrix. F is a nonlinear function. To apply a least squares identification method, F is linearised using the first order Taylor Expansion.

It must be noted that the estimated model will only work for a close range of operating conditions (range of velocities, fluid level inside the dispenser barrel etc.) and the model has to be approximated again if conditions change. This estimation cycle has to be established experimentally.

Appendix F

License Agreements

**SPRINGER LICENSE
TERMS AND CONDITIONS**

Feb 26, 2014

This is a License Agreement between Mihaela L Vlasea ("You") and Springer ("Springer") provided by Copyright Clearance Center ("CCC"). The license consists of your order details, the terms and conditions provided by Springer, and the payment terms and conditions.

All payments must be made in full to CCC. For payment instructions, please see information listed at the bottom of this form.

License Number	3336571346474
License date	Feb 26, 2014
Licensed content publisher	Springer
Licensed content publication	The International Journal of Advanced Manufacturing Technology
Licensed content title	A combined additive manufacturing and micro-syringe deposition technique for realization of bio-ceramic structures with micro-scale channels
Licensed content author	Mihaela Vlasea
Licensed content date	Jan 1, 2013
Volume number	68
Issue number	9
Type of Use	Thesis/Dissertation
Portion	Full text
Number of copies	1
Author of this Springer article	Yes and you are the sole author of the new work
Order reference number	
Title of your thesis / dissertation	Additive Manufacturing Methodology and System for Fabrication of Porous Structures with Functionally Graded Properties
Expected completion date	Feb 2014
Estimated size(pages)	160
Total	0.00 USD

Figure F.1

**ELSEVIER LICENSE
TERMS AND CONDITIONS**

Feb 26, 2014

This is a License Agreement between Mihaela L Vlasea ("You") and Elsevier ("Elsevier") provided by Copyright Clearance Center ("CCC"). The license consists of your order details, the terms and conditions provided by Elsevier, and the payment terms and conditions.

All payments must be made in full to CCC. For payment instructions, please see information listed at the bottom of this form.

Supplier	Elsevier Limited The Boulevard, Langford Lane Kidlington, Oxford, OX5 1GB, UK
Registered Company Number	1982084
Customer name	Mihaela L Vlasea
Customer address	789 Commonwealth Cres. Kitchener, ON N2E4K8
License number	3336570443186
License date	Feb 26, 2014
Licensed content publisher	Elsevier
Licensed content publication	Journal of Materials Processing Technology
Licensed content title	Experimental characterization and numerical modeling of a micro-syringe deposition system for dispensing sacrificial photopolymers on particulate ceramic substrates
Licensed content author	Mihaela Vlasea, Ehsan Toyserkani
Licensed content date	November 2013
Licensed content volume number	213
Licensed content issue number	11
Number of pages	8
Start Page	1970
End Page	1977
Type of Use	reuse in a thesis/dissertation
Portion	full article
Format	both print and electronic
Are you the author of this Elsevier article?	Yes
Will you be translating?	No
Title of your thesis/dissertation	Additive Manufacturing Methodology and System for Fabrication of Porous Structures with Functionally Graded Properties
Expected completion date	Feb 2014
Estimated size (number of pages)	160
Elsevier VAT number	GB 494 6272 12
Permissions price	0.00 USD
VAT/Local Sales Tax	0.00 USD / 0.00 GBP
Total	0.00 USD

Figure F.2

References

- [1] J. J. Sobczak and L. Drenchev. Metallic Functionally Graded Materials: A Specific Class of Advanced Composites. *Journal of Materials Science & Technology*, 29(4):297–316, April 2013. [1](#), [5](#), [6](#)
- [2] E. Mercadelli, A. Sanson, and C. Galassi. *Piezoelectric ceramics, Chapter 6, Porous piezoelectric ceramics*. First edition, 2010. [1](#), [2](#), [6](#)
- [3] M. Mehrali, F. S. Shirazi, H. S. C. Metselaar, N. A. Bin K. Kadri, and N. A. A. Osman. Dental implants from functionally graded materials. *Journal of biomedical materials research. Part A*, 101(10):3046–57, October 2013. [1](#), [2](#), [3](#), [6](#), [19](#)
- [4] C. Zhou, P. Wang, and W. Li. Fabrication of functionally graded porous polymer via supercritical CO₂ foaming. *Composites Part B: Engineering*, 42(2):318–325, March 2011. [1](#)
- [5] A. Butscher, M. Bohner, S. Hofmann, L. Gauckler, and R. Müller. Structural and material approaches to bone tissue engineering in powder-based three-dimensional printing. *Acta Biomaterialia*, 7(3):907–20, March 2011. [1](#), [3](#), [10](#), [12](#), [13](#), [18](#), [19](#), [52](#), [61](#), [62](#), [74](#), [84](#)
- [6] D. W. Hutmacher. Scaffolds in tissue engineering bone and cartilage. *Biomaterials*, 21(24):2529–43, December 2000. [2](#), [5](#), [6](#), [10](#), [12](#), [18](#), [19](#), [90](#)
- [7] J. R. Porter, T. T. Ruckh, and K. C. Popat. Bone tissue engineering: a review in bone biomimetics and drug delivery strategies. *Biotechnology progress*, 25(6):1539–60, 2009. [2](#), [18](#), [19](#), [86](#)
- [8] B. Stevens, Y. Yang, A. Mohandas, B. Stucker, and K. T. Nguyen. A review of materials, fabrication methods, and strategies used to enhance bone regeneration in engineered bone

- tissues. *Journal of biomedical materials research. Part B, Applied biomaterials*, 85(2):573–82, May 2008. [2](#), [5](#), [8](#), [12](#), [86](#)
- [9] E. Mercadelli, A. Sanson, P. Pinasco, E. Roncari, and C. Galassi. Influence of carbon black on slurry compositions for tape cast porous piezoelectric ceramics. *Ceramics International*, 37(7):2143–2149, September 2011. [2](#), [5](#)
- [10] B. P. Kumar, H. H. Kumar, and D. K. Kharat. Study on pore-forming agents in processing of porous piezoceramics. *Journal of Materials Science: Materials in Electronics*, 16(10):681–686, October 2005. [2](#)
- [11] I. Yadroitsev, I. Shishkovsky, P. Bertrand, and I. Smurov. Manufacturing of fine-structured 3D porous filter elements by selective laser melting. *Applied Surface Science*, 255(10):5523–5527, March 2009. [2](#)
- [12] C. Hong, J. Du, J. Liang, X. Zhang, and J. Han. Functionally graded porous ceramics with dense surface layer produced by freeze-casting. *Ceramics International*, 37(8):3717–3722, December 2011. [2](#), [4](#), [5](#)
- [13] N . P. Brandon and D. J. Brett. Engineering porous materials for fuel cell applications. *Philosophical transactions. Series A, Mathematical, physical, and engineering sciences*, 364(1838):147–59, January 2006. [2](#)
- [14] Y. Liu, C. Compson, and M. Liu. Nanostructured and functionally graded cathodes for intermediate temperature solid oxide fuel cells. *Journal of Power Sources*, 138(1-2):194–198, November 2004. [2](#)
- [15] S. W. Sofie. Fabrication of functionally graded and aligned porosity in thin ceramic Substrates with the novel freeze tape-casting process. *Journal of the American Ceramic Society*, 90(7):2024–2031, July 2007. [2](#)
- [16] A. Bandyopadhyay, B. V. Krishna, W. Xue, and S. Bose. Application of laser engineered net shaping (LENS) to manufacture porous and functionally graded structures for load bearing implants. *Journal of materials science. Materials in medicine*, 20 Suppl 1:S29–34, December 2009. [3](#)

- [17] C. Szpalski, M. Wetterau, J. Barr, and S. M. Warren. Bone tissue engineering: current strategies and techniques Part I : Scaffolds. *Tissue Engineering Part B-Reviews*, 18(4):246–257, 2012. [3](#)
- [18] D. L. Bartel, D. T. Davy, and T. M. Keaveny. *Orthopaedic biomechanics: mechanics and design in musculoskeletal systems*. Pearson Prentice Hall, Upper Saddle River, first edition, 2006. [3](#), [17](#)
- [19] H. M. Frost. Bone’s mechanostat: a 2003 update. *The anatomical record. Part A, Discoveries in molecular, cellular, and evolutionary biology*, 275(2):1081–101, December 2003. [3](#)
- [20] J. L. Koh. The effect of graft height mismatch on contact pressure following osteochondral grafting: a biomechanical study. *American Journal of Sports Medicine*, 32(2):317–320, March 2004. [3](#), [18](#), [90](#)
- [21] S. J. Hollister. Porous scaffold design for tissue engineering. *Nature materials*, 4(7):518–24, July 2005. [4](#), [7](#), [12](#)
- [22] S. Deville. Freeze-casting of porous biomaterials: structure, properties and opportunities. *Materials*, 3(3):1913–1927, March 2010. [4](#)
- [23] N. Annabi, J. W. Nichol, X. Zhong, C. Ji, S. Koshy, A. Khademhosseini, and F. Dehghani. Controlling the porosity and microarchitecture of hydrogels for tissue engineering. *Tissue engineering. Part B, Reviews*, 16(4):371–83, August 2010. [5](#), [6](#)
- [24] S. G. Kazarian. Polymer processing with supercritical fluids. *Polymer Science*, 42(1):78–101, 2000. [5](#)
- [25] Y. Liu and Z. Jin. Electric current assisted sintering of continuous functionally graded Ti₂AlN/TiN material. *Ceramics International*, 38(1):217–222, January 2012. [6](#)
- [26] M. Thieme, K. P. Wieters, F. Bergner, D. Scharnweber, H. Worch, J. Ndop, T. J. Kim, and W. Grill. Titanium powder sintering for preparation of a porous functionally graded material destined for orthopaedic implants. *Journal of materials science. Materials in medicine*, 12(3):225–31, March 2001. [6](#)

- [27] X. P. Fan, B. Feng, Y. L. Di, J. X. Wang, X. Lu, and J. Weng. Graded porous titanium scaffolds fabricated using powder metallurgy technique. *Powder Metallurgy and Metal Ceramics*, 51(5-6):372–377, October 2012. [6](#)
- [28] T. Matsuno, K. Watanabe, K. Ono, and M. Koishi. Preparation of laminated hydroxyapatite a zirconia sintered composite with the gradient composition. *Journal of Materials Science Letters*, 7(16):1349–1351, 1998. [6](#)
- [29] M. G. Kutty, S. Bhaduri, and S. B. Bhaduri. Gradient surface porosity in titanium dental implants: relation between processing parameters and microstructure. *Journal of Materials Science. Materials in Medicine*, 15(2):145–50, February 2004. [6](#)
- [30] D. W. Hutmacher, M. Sittinger, and M. V. Risbud. Scaffold-based tissue engineering: rationale for computer-aided design and solid free-form fabrication systems. *Trends in Biotechnology*, 22(7):354–62, July 2004. [7](#), [9](#), [12](#), [13](#), [93](#)
- [31] K. Leong, C. M. Cheah, and C. K. Chua. Solid freeform fabrication of three-dimensional scaffolds for engineering replacement tissues and organs. *Biomaterials*, 24(13):2363–78, June 2003. [7](#), [9](#), [12](#), [13](#), [18](#), [34](#)
- [32] W. K. Chiu and K. M. Yu. Direct digital manufacturing of three-dimensional functionally graded material objects. *Computer-Aided Design*, 40(12):1080–1093, December 2008. [7](#)
- [33] M. Vlasea, Y. Shanjani, A. Basalah, and E. Toyserkani. Additive manufacturing of scaffolds for tissue engineering of bone and cartilage. *International Journal of Advanced Manufacturing Systems*, 13(1):129–147, 2010. [8](#)
- [34] ASTM International. ASTM F2792 - 12a Standard Terminology for Additive Manufacturing Technologies. Technical report, 2012. [8](#)
- [35] S. Yang, Z. Du, and C. K. Chua. Review The Design of Scaffolds for Use in Tissue Engineering. Part II. Rapid Prototyping Techniques. *Tissue Engineering*, 8(1):1–11, 2002. [8](#), [9](#), [10](#), [12](#), [13](#)
- [36] R. Liska, M. Schuster, R. Inführ, C. Turecek, C. Fritscher, B. Seidl, V. Schmidt, L. Kuna, a. Haase, F. Varga, H. Lichtenegger, and J. Stampfl. Photopolymers for rapid prototyping. *Journal of Coatings Technology and Research*, 4(4):505–510, November 2007. [8](#)

- [37] A. Woesz, M. Rumpler, J. Stampf, F. Varga, N. Fratzl-zelman, and P. Roschger. Towards bone replacement materials from calcium phosphates via rapid prototyping and ceramic gelcasting. *Materials Science and Engineering C*, 25:181–186, 2005. [8](#)
- [38] J. W. Lee, P. X. Lan, B. Kim, G. Lim, and D. W. Cho. Fabrication and characteristic analysis of a poly(propylene fumarate) scaffold using micro-stereolithography technology. *Journal of Biomedical Materials Research. Part B, Applied Biomaterials*, 87(1):1–9, October 2008. [8](#)
- [39] Z. Xiong, Y. Yongnian, W. Shenguo, Z. Renji, and Z. Chao. Fabrication of porous scaffolds for bone tissue engineering via low-temperature deposition. *Scripta Materialia*, 46(11):771–776, June 2002. [9](#)
- [40] M. J. Cima, J. S. Haggerty, E. M. Sachs, and P. A. Williams. Three-dimensional printing techniques, Patent Number 5,204,055, 1993. [10](#)
- [41] M. J. Cima, J. S. Haggerty, E. M. Sachs, and P. A. Williams. Three Dimensional Printing Techniques, Patent Number 5,340,656, 1994. [10](#)
- [42] M. Cima, E. Sachs, T. L. Fan, J. F. Bredt, S. P. Michaels, S. Khanuja, A. Lauder, S. J. Lee, D. Brancazio, A. Curodeau, and H. Tuerck. Three Dimensional Printing, Patent Number 5,387,380, 1995. [10](#)
- [43] E. Carreno-Morelli, S. Martinerie, and J. E. Bidaux. Three-dimensional printing of shape memory alloys. *Progress in Powder Metallurgy, Pts 1 and 2 - Materials Science Forum*, 536:477–480, 2007. [11](#)
- [44] K. Lu and W. T. Reynolds. 3DP process for fine mesh structure printing. *Powder Technology*, 187(1):11–18, October 2008. [11](#), [52](#)
- [45] J. Moon, A. C. Caballero, L. Hozer, Y. M. Chiang, and M. J. Cima. Fabrication of functionally graded reaction infiltrated SiC-Si composite by three-dimensional printing (3DP) process. *Materials Science and Engineering: A*, 298(1-2):110–119, January 2001. [11](#)
- [46] S. M. Allen and E. M. Sachs. Three-dimensional printing of metal parts for tooling and other applications. *Metals and Materials*, 6(6):589–594, 2000. [11](#)

- [47] S. B. Hong, N. Eliaz, G. G. Leisk, E. M. Sach, R. M. Latanision, and S. M. Allen. A new Ti-5Ag alloy for customized prostheses by three-dimensional printing (3DP). *Journal of Dental Research*, 80(3):860–863, March 2001. [11](#)
- [48] Y. Shanjani, Y. Hu, R. M. Pilliar, and E. Toyserkani. Mechanical characteristics of solid-freeform-fabricated porous calcium polyphosphate structures with oriented stacked layers. *Acta Biomaterialia*, 7(4):1788–96, April 2011. [11](#), [12](#), [35](#), [53](#), [54](#), [55](#), [62](#), [63](#), [74](#), [76](#), [78](#), [79](#), [85](#), [86](#), [90](#), [92](#), [94](#), [101](#)
- [49] P. Habibovic, U. Gbureck, C. J. Doillon, D. C. Bassett, C. A. Blitterswijk, and J. E. Barralet. Osteoconduction and osteoinduction of low-temperature 3D printed bioceramic implants. *Biomaterials*, 29(7):944–53, March 2008. [11](#), [12](#)
- [50] U. Gbureck, T. Hölzel, C. J. Doillon, F. A. Müller, and J. E. Barralet. Direct printing of bioceramic implants with spatially localized angiogenic factors. *Advanced Materials*, 19(6):795–800, March 2007. [11](#), [12](#)
- [51] A. Khalyfa, S. Vogt, J. Weisser, G. Grimm, A. Rechtenbach, W. Meyer, and M. Schnabelrauch. Development of a new calcium phosphate powder-binder system for the 3D printing of patient specific implants. *Journal of Materials Science: Materials in Medicine*, 18(5):909–916, May 2007. [11](#), [12](#), [52](#)
- [52] E. Vorndran, M. Klarner, U. Klammert, L. M. Grover, S. Patel, J. E. Barralet, and U. Gbureck. 3D Powder Printing of β -Tricalcium Phosphate Ceramics Using Different Strategies. *Advanced Engineering Materials*, 10(12):B67–B71, December 2008. [11](#), [52](#)
- [53] U. Gbureck, T. Hölzel, I. Biermann, J. E. Barralet, and L. M. Grover. Preparation of tricalcium phosphate/calcium pyrophosphate structures via rapid prototyping. *Journal of Materials Science: Materials in Medicine*, 19(4):1559–63, April 2008. [11](#), [52](#)
- [54] J. Suwanprateeb. Influence of printing parameters on the transformation efficiency of 3D-printed plaster of paris to hydroxyapatite and its properties. *Rapid Prototyping Journal*, 18(6):490–499, 2012. [11](#), [52](#)
- [55] T.J. Hsu and W. H. Lai. Manufacturing parts optimization in the three-dimensional printing process by the taguchi method. *Journal of the Chinese Institute of Engineers*, 33(1):121–130, 2010. [11](#), [52](#)

- [56] P. H. Warnke, H. Seitz, F. Warnke, S. T. Becker, S. Sivananthan, E. Sherry, Q. Liu, J. Wiltfang, and T. Douglas. Ceramic scaffolds produced by computer-assisted 3D printing and sintering: characterization and biocompatibility investigations. *Journal of Biomedical Materials Research. Part B, Applied Biomaterials*, 93(1):212–7, April 2010. [11](#), [12](#)
- [57] U. Klammert, T. Reuther, C. Jahn, B. Kraski, C. Kübler, and U. Gbureck. Cytocompatibility of brushite and monetite cell culture scaffolds made by three-dimensional powder printing. *Acta Biomaterialia*, 5(2):727–34, February 2009. [11](#)
- [58] S. N. Rath, L. A. Strobel, A. Arkudas, J. P. Beier, A. K. Maier, P. Greil, R. E. Horch, and U. Kneser. Osteoinduction and survival of osteoblasts and bone-marrow stromal cells in 3D biphasic calcium phosphate scaffolds under static and dynamic culture conditions. *Journal of Cellular and Molecular Medicine*, 16(10):2350–61, October 2012. [11](#)
- [59] R. Chumnanklang, T. Panyathanmaporn, K. Sitthiseripratip, and J. Suwanprateeb. 3D printing of hydroxyapatite: Effect of binder concentration in pre-coated particle on part strength. *Materials Science and Engineering: C*, 27(4):914–921, May 2007. [11](#)
- [60] J. Suwanprateeb and R. Chumnanklang. Three-dimensional printing of porous polyethylene structure using water-based binders. *Journal of Biomedical Materials Research Part B-Applied Biomaterials*, 78B(1):138–145, 2006. [11](#)
- [61] G. Gibbons. 3D Printing of cement composites. *Advances in Applied Ceramics*, 109(5):287–290, 2010. [11](#)
- [62] J. Will, R. Melcher, C. Treul, N. Travitzky, U. Kneser, E. Polykandriotis, R. Horch, and P. Greil. Porous ceramic bone scaffolds for vascularized bone tissue regeneration. *Journal of Materials Science: Materials in Medicine*, 19(8):2781–90, August 2008. [11](#), [12](#), [65](#), [74](#), [75](#)
- [63] W. Zhang, R. Melcher, N. Travitzky, R. K. Bordia, and P. Greil. Three-dimensional printing of complex-shaped alumina/glass composites. *Advanced Engineering Materials*, 11(12):1039–1043, November 2009. [11](#), [78](#)
- [64] M. Vaezi and C. K. Chua. Effects of layer thickness and binder saturation level parameters on 3D printing process. *The International Journal of Advanced Manufacturing Technology*, 53(1-4):275–284, July 2010. [11](#), [62](#)

- [65] M. Castilho, M. Dias, U. Gbureck, J. Groll, P. Fernandes, Inês Pires, B. Gouveia, J. Rodrigues, and E. Vorndran. Fabrication of computationally designed scaffolds by low temperature 3D printing. *Biofabrication*, 5(3):035012, September 2013. [11](#), [12](#)
- [66] K. Igawa, M. Mochizuki, O. Sugimori, K. Shimizu, K. Yamazawa, H. Kawaguchi, K. Nakamura, T. Takato, R. Nishimura, S. Suzuki, M. Anzai, U. Chung, and N. Sasaki. Tailor-made tricalcium phosphate bone implant directly fabricated by a three-dimensional ink-jet printer. *Journal of Artificial Organs : the Official Journal of the Japanese Society for Artificial Organs*, 9(4):234–40, January 2006. [12](#)
- [67] S. Choi, J. Lee, K. Igawa, O. Sugimori, S. Suzuki, M. Mochizuki, R. Nishimura, U. Chung, and N. Sasaki. Bone regeneration within a tailor-made tricalcium phosphate bone implant with both horizontal and vertical cylindrical holes transplanted into the skull of dogs. *Journal of Artificial Organs : the Official Journal of the Japanese Society for Artificial Organs*, 12(4):274–7, January 2009. [12](#)
- [68] M. Castilho, I. Pires, B. Gouveia, and J. Rodrigues. Structural evaluation of scaffolds prototypes produced by three-dimensional printing. *The International Journal of Advanced Manufacturing Technology*, 56(5-8):561–569, February 2011. [12](#), [13](#)
- [69] S. Yang, K. F. Leong, Z. Du, and C. K. Chua. The design of scaffolds for use in tissue engineering. Part I. Traditional factors. *Tissue Engineering*, 7(6):679–89, December 2001. [12](#), [18](#), [19](#), [34](#), [63](#), [76](#), [86](#)
- [70] Y. Shanjani. Solid freeform fabrication of porous calcium polyphosphate structures for use in orthopaedics. Technical report, 2011. [13](#), [16](#)
- [71] M. Hutchinson. The burden of musculoskeletal diseases in the united states: prevalence, societal and economic cost. *Journal of the American College of Surgeons*, 208(1):e5–e6, January 2009. [17](#)
- [72] S. Cheng, V. Poon, E. DeSa, A. Dragan, S. Chen, and N. DeGuia. Hip and knee replacements in Canada: Canadian joint replacement registry 2013 annual report. Technical report, Canadian Institute for Health Information, Canadian Joint Replacement Registry (CJRR) Advisory Committee, Ottawa, 2013. [17](#)

- [73] P. D. Gikas, L. Bayliss, G. Bentley, and T. W. R. Briggs. An overview of autologous chondrocyte implantation. *Bone and Joint Surgery - British Volume*, 91(8):997–1006, August 2009. [17](#), [18](#), [90](#)
- [74] H. S. Vasiliadis, J. Wasiak, and G. Salanti. Autologous chondrocyte implantation for the treatment of cartilage lesions of the knee: a systematic review of randomized studies. *Knee Surgery, Sports Traumatology, Arthroscopy*, 18(12):1645–1655, March 2010. [18](#)
- [75] M Vert, S M Li, P Guerin, and Substances Macromoleculaires. Bioresorbability and biocompatibility of aliphatic polyesters. *Journal of Materials Science: Materials In Medicine*, 3(6):432–446, 1992. [18](#)
- [76] R. M. Pilliar, M. J. Filiaggi, J. D. Wells, M. D. Grynepas, and R. A. Kandel. Porous calcium polyphosphate scaffolds for bone substitute applications - in vitro characterization. *Biomaterials*, 22(9):963–72, May 2001. [18](#), [56](#), [62](#), [79](#), [85](#), [92](#)
- [77] R. M. Pilliar, R. A. Kandel, M. D. Grynepas, P. Zalzal, and M. Hurtig. Osteochondral defect repair using a novel tissue engineering approach: sheep model study. *Technology and Health Care: Official Journal of the European Society for Engineering and Medicine*, 15(1):47–56, January 2007. [18](#), [79](#), [91](#), [92](#)
- [78] B. S. Chang, C. K. Lee, K. S. Hong, H. J. Youn, H. S. Ryu, S. S. Chung, and K. W. Park. Osteoconduction at porous hydroxyapatite with various pore configurations. *Biomaterials*, 21(12):1291–8, June 2000. [19](#), [34](#)
- [79] S. Kujala, J. Ryhanen, A. Danilov, and J. Tuukkanen. Effect of porosity on the osteointegration and bone ingrowth of a weight-bearing nickel-titanium bone graft substitute. *Biomaterials*, 24(25):4691–4697, November 2003. [19](#), [34](#)
- [80] R. Langer and J. P. Vacanti. Tissue Engineering. *Science*, 260(5110):920–926, 1993. [19](#)
- [81] V. Karageorgiou and D. Kaplan. Porosity of 3D biomaterial scaffolds and osteogenesis. *Biomaterials*, 26(27):5474–91, September 2005. [19](#), [34](#), [57](#), [63](#), [76](#), [86](#)
- [82] M. Vlasea, Y. Shanjani, A. Bothe, R. Kandel, and E. Toyserkani. A combined additive manufacturing and micro-syringe deposition technique for realization of bio-ceramic structures with micro-scale channels. *The International Journal of Advanced Manufacturing Technology*, 68(9-12):2261–2269, February 2013. [23](#)

- [83] M. Vlasea and E. Toyserkani. Experimental characterization and numerical modeling of a micro-syringe deposition system for dispensing sacrificial photopolymers on particulate ceramic substrates. *Journal of Materials Processing Technology*, 213(11):1970–1977, 2013. [23](#), [36](#)
- [84] G. Vozzi, A. Previti, D. Rossi, and A. Ahluwalia. Microsyringe-based deposition of two-dimensional and three-dimensional polymer scaffolds with a well-defined geometries for application to tissue engineering. *Tissue Engineering*, 8(6):1089–1098, 2002. [26](#), [40](#), [43](#)
- [85] Y. Shanjani, J. N. A. De Croos, R. M. Pilliar, R. A. Kandel, and E. Toyserkani. Solid freeform fabrication and characterization of porous calcium polyphosphate structures for tissue engineering purposes. *Journal of Biomedical Materials Research. Part B, Applied Biomaterials*, 93(2):510–9, May 2010. [33](#), [34](#), [35](#), [53](#), [54](#), [55](#), [63](#), [79](#), [92](#), [94](#), [101](#)
- [86] R. M. German. *Sintering theory and practice*. John Wiley and Sons, New York, first edition, 1996. [34](#)
- [87] J. W. Gilman, D. L. Vanderhart, and T. Kashiwagi. Thermal-decomposition chemistry of poly(vinyl alcohol) - char characterization and reactions with bismaleimides. *Fire and Polymers II: Materials and Tests for Hazard Prevention*, 599:161–85, 1995. [35](#)
- [88] X.B. Chen and J. Kai. Modeling of positive-displacement fluid dispensing processes. *IEEE Transactions on Electronics Packaging Manufacturing*, 27(3):157–163, July 2004. [37](#), [38](#), [39](#)
- [89] X. B. Chen, G. Schoenau, and W. J. Zhang. Modelling of time-pressure fluid dispensing processes. *IEEE Transactions on Electronics Packaging Manufacturing*, 23(4):236–236, October 2000. [38](#), [39](#)
- [90] M. Lee, J. C. Y. Dunn, and B. M. Wu. Scaffold fabrication by indirect three-dimensional printing. *Biomaterials*, 26(20):4281–9, July 2005. [48](#), [49](#), [62](#)
- [91] G. L. Batten. Liquid imbibition in capillaries and packed beds. *Journal of Colloid and Interface Science*, 102(2), 1984. [49](#)
- [92] B. Markicevic, H. Li, A. R. Zand, and H. K. Navaz. Influence of the boundary conditions on capillary flow dynamics and liquid distribution in a porous medium. *American Institute of Chemical Engineers Journal*, 58(9), 2012. [49](#)

- [93] R. M. Pilliar, J. Hong, and P. J. Santerre. Method of manufacture of porous inorganic structures, Patent Number 7494614, 2009. [55](#), [67](#), [79](#), [95](#)
- [94] J. Absi and P. Fournier. Influence of experimental parameters on the estimated value of Weibull’s modulus. *Journal of Materials Science*, 34:1219–1227, 1999. [56](#)
- [95] R. K. Holman, S. A. Uhland, M. J. Cima, and E. Sachs. Surface adsorption effects in the inkjet printing of an aqueous polymer solution on a porous oxide ceramic substrate. *Journal of Colloid and Interface Science*, 247(2):266–74, March 2002. [62](#)
- [96] K. Lu, M. Hiser, and W. Wu. Effect of particle size on three dimensional printed mesh structures. *Powder Technology*, 192(2):178–183, June 2009. [62](#), [65](#), [74](#)
- [97] P. Miranda, A. Pajares, E. Saiz, A. P. Tomsia, and F. Guiberteau. Mechanical properties of calcium phosphate scaffolds fabricated by robocasting. *Journal of Biomedical Materials Research. Part A*, 85(1):218–27, April 2008. [63](#), [76](#), [86](#)
- [98] L. Montanaro, O. Y. Jorand, G. Fantozzib, and A. Negroa. Ceramic foams by powder processing. *Journal of the European Ceramic Society*, 18(9):1339–1350, 1998. [63](#), [86](#)
- [99] M. Lanzetta and E. Sachs. Improved surface finish in 3D printing using bimodal powder distribution. *Rapid Prototyping Journal*, 9(3):157–166, 2003. [65](#), [75](#)
- [100] M. D. Grynypas, R. M. Pilliar, R. A. Kandel, R. Renlund, M. Filiaggi, and M. Dumitriu. Porous calcium polyphosphate scaffolds for bone substitute applications in vivo studies. *Biomaterials*, 23(9):2063–70, May 2002. [79](#)
- [101] M.J Bannister. Shape sensitivity of initial sintering equations. *Journal of the American Ceramic Society*, 51(10):548–553, 1968. [85](#)
- [102] D. Drucker. *Introduction to Mechanics of Deformable Solids*. McGraw-Hill, New York, 1967. [85](#)
- [103] H. J. Lundberg, K. C. Foucher, T. P. Andriacchi, and M. A. Wimmer. Direct comparison of measured and calculated total knee replacement force envelopes during walking in the presence of normal and abnormal gait patterns. *Journal of Biomechanics*, 45(6):990–6, April 2012. [90](#), [91](#), [92](#)

- [104] H. J. Lundberg, K. C. Foucher, and M. A. Wimmer. A parametric approach to numerical modeling of TKR contact forces. *Journal of Biomechanics*, 42(4):541–5, March 2009. [90](#), [91](#), [92](#)
- [105] W. R. Taylor, R. M. Ehrig, M. O. Heller, H. Schell, P. Seebeck, and G. N. Duda. Tibio-femoral joint contact forces in sheep. *Journal of Biomechanics*, 39(5):791–8, January 2006. [90](#), [92](#)
- [106] R. A. Gallo and B. T. Feeley. Cartilage defects of the femoral trochlea. *Knee Surgery, Sports Traumatology, Arthroscopy*, 17(11):1316–25, November 2009. [90](#)
- [107] L. D. Kaplan, M. R. Schurhoff, H. Selesnick, M. Thorpe, and J. W. Uribe. Magnetic resonance imaging of the knee in asymptomatic professional basketball players. *Arthroscopy : the Journal of Arthroscopic & Related Surgery* :, 21(5):557–61, May 2005. [90](#)
- [108] W. Widuchowski, J. Widuchowski, and T. Trzaska. Articular cartilage defects: study of 25,124 knee arthroscopies. *The Knee*, 14(3):177–82, June 2007. [90](#)
- [109] J. R. Perera, P. D. Gikas, and G. Bentley. The present state of treatments for articular cartilage defects in the knee. *Annals of the Royal College of Surgeons of England*, 94(6):381–7, September 2012. [90](#)
- [110] G. Bentley, J. S. Bhamra, P. D. Gikas, J. A. Skinner, R. Carrington, and T. W. Briggs. Repair of osteochondral defects in joints - how to achieve success. *Injury*, 44(S1):S3–S10, January 2013. [90](#)
- [111] J. H. Caton and D. Dejour. Tibial tubercle osteotomy in patello-femoral instability and in patellar height abnormality. *International Orthopaedics*, 34(2):305–309, February 2010. [90](#)
- [112] Eva-Maria Brick, Heike Rudolph, Jens Arnold, and Ralph G Luthardt. Analysis of three-dimensional sinter shrinkage of copings made from alumina in an innovative direct shaping process. *Computerized medical imaging and graphics : the official journal of the Computerized Medical Imaging Society*, 28(3):159–65, April 2004. [93](#)
- [113] Ven-Gen Lee and Ting-Hao Yeh. Sintering effects on the development of mechanical properties of fired clay ceramics. *Materials Science and Engineering: A*, 485(1-2):5–13, June 2008. [93](#)

- [114] Sylvain Marinel and Etienne Savary. In situ measurement of the shrinkage during microwave sintering. *Journal of Materials Processing Technology*, 209(10):4784–4788, June 2009. [93](#)
- [115] Y. Sahilliolu and Y. Yemez. Coarse-to-fine surface reconstruction from silhouettes and range data using mesh deformation. *Computer Vision and Image Understanding*, 114(3):334–348, March 2010. [93](#)
- [116] H. X. Li, J. Liu, C. P. Chen, and H. Deng. A simple model-based approach for fluid dispensing analysis and control. *IEEE/ASME Transactions on Mechatronics*, 12(4):491–503, August 2007. [126](#), [127](#)